Reconciling Surface Deflections From Simulations of Global Mantle Convection

Conor Patrick O'Malley[1], Gareth G Roberts[1], James Panton[2], Fred D Richards[1], J. Huw Davies[3], Victoria M Fernandes[4], and Sia Ghelichkhan[5]

[1]Imperial College London
[2]Cardiff University
[3]School of Earth and Ocean Sciences, Cardiff University
[4]GFZ Potsdam
[5]Australian National University

April 12, 2024

Abstract

The modern state of the mantle and its evolution on geological timescales is of widespread importance for the Earth sciences. For instance, it is generally agreed that mantle flow is manifest in topographic and drainage network evolution, glacio-eustasy and in the distribution of sediments. There now exists a variety of theoretical approaches to predict histories of mantle convection and its impact on surface deflections. A general goal is to make use of observed deflections to identify Earth-like simulations and constrain the history of mantle convection. Several important insights into roles of radial and non-radial viscosity variations, gravitation, and the importance of shallow structure already exist. Here we seek to bring those insights into a single framework to elucidate the relative importance of popular modelling choices on predicted instantaneous vertical surface deflections. We start by comparing results from numeric and analytic approaches to solving the equations of motion that are ostensibly parameterised to be as-similar-as-possible. Resultant deflections can vary by $\sim$10\%, increasing to $\sim$25$\% when viscosity is temperature-dependent. Including self-gravitation and gravitational potential of the deflected surface are relatively small sources of discrepancy. However, spherical harmonic correlations between model predictions decrease dramatically with the excision of shallow structure to increasing depths, and when radial viscosity structure is modified. The results emphasise sensitivity of instantaneous surface deflections to density and viscosity anomalies in the upper mantle. They reinforce the view that a detailed understanding of lithospheric structure is crucial for relating mantle convective history to observations of vertical motions at Earth's surface.

Reconciling Surface Deflections From Simulations of Global Mantle Convection

Conor P. B. O'Malley[1,2], Gareth G. Roberts[1], James Panton[3], Fred D. Richards[1], J. Huw Davies[3], Victoria M. Fernandes[1,4], Sia Ghelichkhan[5]

[1]Department of Earth Science & Engineering, Imperial College London, London SW7 2BP, UK
[2]now at Cathie Group, 2-4 Hanover Square, Newcastle upon Tyne, NE1 3NP, UK
[3]School of Earth & Environmental Sciences, University of Cardiff, Park Place, Cardiff CF10 3AT, UK
[4]now at Section 4.6 Geomorphology, GFZ Potsdam, Telegrafenberg, 14473 Potsdam, Germany
[5]Research School of Earth Sciences, Australian National University, 142 Mills Road, Acton, ACT 0200, Australia

Key Points:

- Numeric and analytic predictions of surface deflections from mantle convection simulations are compared.
- Impact of gravitation, excising shallow structure, boundary conditions, and different viscosity and density distributions are quantified.
- Calculated effective contributions to surface deflection emphasize dominance of upper mantle structure.

Corresponding author: Conor O'Malley; Gareth Roberts, c_omalley1@msn.com; gareth.roberts@imperial.ac.uk

Abstract

The modern state of the mantle and its evolution on geological timescales is of widespread importance for the Earth sciences. For instance, it is generally agreed that mantle flow is manifest in topographic and drainage network evolution, glacio-eustasy and in the distribution of sediments. There now exists a variety of theoretical approaches to predict histories of mantle convection and its impact on surface deflections. A general goal is to make use of observed deflections to identify Earth-like simulations and constrain the history of mantle convection. Several important insights into the role of radial and non-radial viscosity variations, gravitation, and the importance of shallow structure already exist. Here we seek to bring those insights into a single framework to elucidate the relative importance of popular modelling choices on predicted instantaneous vertical surface deflections. We start by comparing results from numeric and analytic approaches to solving the equations of motion that are ostensibly parameterised to be as-similar-as-possible. Resultant deflections can vary by $\sim$10%, increasing to $\sim$ 25% when viscosity is temperature-dependent. Including self-gravitation and gravitational potential of the deflected surface are relatively small sources of discrepancy. However, spherical harmonic correlations between model predictions decrease dramatically with the excision of shallow structure to increasing depths, and when radial viscosity structure is modified. The results emphasise sensitivity of instantaneous surface deflections to density and viscosity anomalies in the upper mantle. They reinforce the view that a detailed understanding of lithospheric structure is crucial for relating mantle convective history to observations of vertical motions at Earth's surface.

Plain Language Summary

Flow of rock within Earth's interior plays a crucial role in evolving the planet. It moves heat and chemicals from deep depths to the surface, for instance. It also moves the lithosphere—the Earth's outer rocky shell—which in turn impacts processes including mountain building, sea-level change, formation of volcanoes, river network evolution, and natural resource distribution. Consequently, we wish to understand the present state, and history, of flowing rock within Earth's interior. Observations exist to address this problem, and mathematics and computing tools can also be used to predict histories of flow and their impact on Earth's surface. We explore how assumptions incorporated into such numeric models can affect calculations of the vertical deflection of Earth's surface. Predictions from different models are compared, with a view to identifying crucial modelling components. Surface sensitivity to deep flow is assessed, demonstrating how surface observations can enlighten flow histories.

1 Introduction

Mantle convection plays a crucial role in Earth's evolution (e.g., Hager & Clayton, 1989; Parsons & Daly, 1983; Pekeris, 1935). It is well understood, for instance, that flow in the mantle is fundamental in the transfer of heat and chemicals from the deep Earth to the surface, in driving horizontal and vertical lithospheric motions (thus tectonic processes), and in magnetism via interactions with the core (e.g., Biggin et al., 2012; Davies et al., 2023; Foley & Fischer, 2017; Hoggard et al., 2016; Holdt et al., 2022; Pekeris, 1935). In turn, many processes operating at or close to Earth's surface are impacted, including glacio-eustasy, magmatism, climate, sediment routing, natural resource distribution, drainage network evolution, and development of biodiversity (e.g., Bahadori et al., 2022; Ball et al., 2021; Braun, 2010; Chang & Liu, 2021; Hazzard et al., 2022; O'Malley et al., 2021; Salles et al., 2017; Stanley et al., 2021). Clearly, understanding the physical and chemical evolution of the mantle has broad implications. An important goal is to determine contributions to surface processes from the modern mantle and its history during, say, the last 100 million years.

Residual oceanic age-depth measurements, potential field data, seismic tomographic models and melting histories of young mafic rocks are providing increasingly coherent observational insights into the modern and recent state of the mantle (e.g., Ball et al., 2022; Davies et al., 2023; Fichtner et al., 2009, 2013; Fichtner & Villaseñor, 2015; French & Romanowicz, 2015; Hoggard et al., 2016; Holdt et al., 2022; Kaula, 1963; Lekić & Fischer, 2014; Priestley & McKenzie, 2013; F. D. Richards et al., 2021). Stratigraphic and geomorphic observations as well as magmatic histories provide clues about the history of mantle convection on geologic timescales (e.g., Al-Hajri et al., 2009; Czarnota et al., 2013; Flament et al., 2015; Fernandes et al., 2019; Fernandes & Roberts, 2021; Galloway et al., 2011; Gunnell & Burke, 2008; Gurnis et al., 2000; Hoggard et al., 2021; Lambeck et al., 1998; Morris et al., 2020; O'Malley et al., 2021; Stanley et al., 2021). Despite these advances, observations providing information about the history of mantle convection are sparse in places, especially within continental interiors and back in time (see e.g., Hoggard et al., 2021). Moreover, disentangling contributions from crustal, lithospheric and sub-lithospheric processes to surface deflections remains challenging and controversial (see e.g. Hoggard et al., 2021; Wang et al., 2022).

Theoretical approaches that retrodict histories of mantle convection can, in principle, be used to fill in spatio-temporal gaps in the observational record and disentangle contributions to surface observables from different geologic processes (e.g., Baumgardner, 1985; Bunge & Baumgardner, 1995; Davies et al., 2013; Flament et al., 2015; Ghelichkhan et al., 2021; Hager et al., 1985; Moucha & Forte, 2011; Steinberger & Antretter, 2006). Increasingly realistic geodynamic simulations incorporating, for instance, plate motions, gravitation and deflection of gravitational potential fields, complex rheologies, viscosity laws that can include temperature, pressure, composition, grain size and strain rate dependence, and assimilation of seismic tomographic information into flow solutions, result in a diverse array of retrodicted flow histories. Mineralogical phase changes, compressibility, different surface and core-mantle boundary slip conditions (e.g., no-slip, free-slip), chemical and thermal buoyancy, and plate motion constraints on mantle structure can also generate diverse predictions of mantle convection and resultant surface deflections (e.g., Baumgardner, 1985; Bunge et al., 2002, 2003; Corrieu et al., 1995; Crameri et al., 2012; Dannberg et al., 2017; "Topographic asymmetry of the South Atlantic from global models of mantle flow and lithospheric stretching", 2014; Forte, 2007; Ghosh & Holt, 2012; Glišović & Forte, 2016; Hager & Clayton, 1989; Heister et al., 2017; Liu & Gurnis, 2008; Panasyuk et al., 1996; Ribe, 2007; Ricard, 2007; Tackley et al., 1993; Zhong et al., 2008; Zhou et al., 2018). Aside from the fundamental choice of governing equations and parameterizations underpinning simulations, mathematical and computational approaches to solve the equations of motion generate different predictions of surface deflections. These approaches sit within two broad families: numeric simulations (e.g., ASPECT, CitcomS, TERRA; Bangerth et al., 2023; Baumgardner, 1985; Zhong et al., 2000), and propagator-matrix-based, quasi-analytic techniques, that can be solved in two or three dimensions, and importantly for our purposes, spherically and spectrally (e.g., Colli et al., 2016; Hager & O'Connell, 1979; Parsons & Daly, 1983).

A challenge then is to establish whether observed surface deflections can be used to discriminate between theoretical predictions of mantle convection, and, in turn, identify models that generate realistic and testable retrodictions. In this study we are principally concerned with establishing similarities and sensitivities of predicted instantaneous vertical surface deflections. We focus on vertical motions for two reasons. First, inventories of measurements of uplift and subsidence—on timescales of mantle convection—now exist for most continents and could be compared to predictions from global simulations in future work (e.g. Fernandes & Roberts, 2021, and references therein). Secondly, many geodynamic simulations incorporate horizontal motions of the lithosphere, which limits their use as a comparator.

From an observational perspective, it would be useful to establish rules-of-thumb that quantify sensitivity of surface deflections to choices made when predicting them. Many such rules are already well known from analytic and numeric solutions of the equations of motion (e.g., Colli et al., 2016; Hager & O'Connell, 1979; Holdt et al., 2022; Lees et al., 2020; Parsons & Daly, 1983). For instance, a suite of benchmark studies exist that compare predictions from numeric mantle convection simulations with analytic solutions (see e.g., Bauer et al., 2019; Kramer et al., 2021; Zhong et al., 2008, and references therein). Those papers tend to focus on establishing the fidelity of numeric models. In contrast, our goals are to, first, understand how calculated deflections are impacted by the choice of methodology used to solve the equations of motion and, secondly, to establish sensitivities to popular assumptions incorporated into simulations. We want to know the extent to which an improved fit between predictions and observations reflects a more Earth-like density and viscosity structure versus modelling choices. Our thesis is that performing all tests in a self-consistent framework, as we do in this study, provides a straightforward way to collate insights into the sensitivities of predicted surface deflections and to simplify the comparison of predictions from different suites of models.

1.1 Our Approach and Paper Structure

We start by exploring the consequences of solving the equations of motion numerically, using the TERRA software, and analytically, using Ghelichkhan et al. (2021)'s propagator matrix algorithms (see Figure 1 & Supporting Information). We make use of the flexibility of numeric approaches by incorporating a variety of assumptions and parameterizations that are not amenable to analytic attack (e.g., temperature-dependent viscosity). All numeric simulations presented in this paper were driven by the plate motion history of Merdith et al. (2021, see Figures 1g–h and S1). The models have a resolution of 60 km at their surface (see Supporting Information for details of model setup and execution). We note that they do not directly assimilate information about the mantle from tomographic models. Ensuring that numeric simulations are accurate and stable means that computational burden is often considerable and hence systematic exploration of parameter space remains challenging. In contrast, analytic approaches can yield calculated surface deflections that are (mathematically) accurate, whilst including features such as radial gravitation, with much less computational cost. Consequently, we make use of propagator matrix techniques to explore parameter space, examine benchmarks, and reproduce results. We establish the sensitivity of solutions to different parameterizations and approaches to solving the equations of motion.

There are at least two important considerations when solving the equations of motion analytically. First, solutions are only known to exist in the spherical harmonic domain for fluid bodies with radial viscosity (i.e., no lateral variability in viscosity). Second, generating solutions in the spherical harmonic domain places practical limits on spatial resolution of solutions. Consider that the number of spherical harmonic coefficients per degree $= 2l+1$, where l is degree, so for a given maximum degree L, there are $(L+1)^2$ coefficients in total. For instance, when $L = 50$ there are $2,601$ coefficients for each model. Consider also that spatial resolution increases approximately with the reciprocal of l (see Section 2.2). Incorporating full resolution output from the numeric models (60 km at the surface) would require $L \approx 880$, with $776,161$ coefficients, which is computationally cumbersome. Furthermore, observational constraints on mantle-related surface deflection are unlikely to be finer than the flexural wavelength of the overlying lithosphere, $l \approx 50$ (e.g., Holdt et al., 2022). With these limitations in mind, we compared surface deflections predicted using different approaches at the same resolution up to $l = 50$ (see Supporting Information and Section 2.3).

Most of the tests in this paper compare surface deflections calculated using the entirety of the model domains (i.e., from CMB to the surface). This approach simplifies like-for-like comparisons of model predictions and comparisons to increasingly complex

scenarios. However, amplitudes of calculated deflections will of course not reflect estimated amplitudes of dynamic topography. This approach purposefully avoids isolating passive or plate-driven surface deflections and sub-plate support from numeric simulations or analytic solutions. Since the central focus of this work is merely on quantifying contrasts that arise from choices made when simulating mantle convection, we wish to avoid incorporating additional modifications where possible. In subsequent tests we examine the consequences of simply removing shallow structure, a widely used approach for estimating dynamic support from simulations (see e.g., Flament et al., 2013; Flament, 2018; Wang et al., 2022).

With this framework in place we generate, compare and contrast predicted surface deflections. The first suite of tests are purposefully simple, e.g., incompressible, constant gravitational acceleration (no self-gravitation or radial variation in gravitation) and have radial viscosity independent of temperature. Results are compared to estimates of sub-plate support from oceanic age-depth residuals with a view to quantifying corrections necessary to convert predicted instantaneous surface deflections into estimates of sub-plate support. We then systematically examine the impact of incorporating radial variations in gravitational acceleration, contribution to flow from deflection of the gravitational potential field, removal of shallow density structure, choice of surface and CMB slip conditions, inclusion of temperature-dependent viscosity, and amplification or reduction of viscosity and density anomalies in the upper and lower mantle (Section 4; Tables 1–2). A closed-loop modelling strategy is explored in which predicted surface deflections from these relatively complex models are compared to results from simpler reference models. Finally, a methodology for assessing effective contributions to surface topography from mantle anomalies is presented.

2 Numeric and Analytic Calculations of Surface Deflection

The Supporting Information document summarises the formulations of Stokes' equations that are solved, model parameter values used and the numeric approach to calculating mantle convection using the TERRA finite-element software. Here, we move straight to explaining how those simulations are used to calculate radial stresses, σ_{rr}, thence vertical deflections, h, at Earth's surface (Figure 1). A methodology for representing model predictions in the spherical harmonic domain is then described. We then examine analytic solutions obtained using propagator matrix techniques.

2.1 Deflections calculated using radial stresses from numeric simulation

Following Parsons and Daly (1983), surface deformation is estimated from numeric simulations of mantle convection by making use of the requirement that normal stress is continuous across the upper boundary of the solid Earth (see also McKenzie, 1977; Ricard, 2015). In other words, radial stresses generated by the solid Earth are required to be balanced by stresses generated by the overlying (oceanic or atmospheric) fluid. There are three contributions to normal stress at this boundary from the mantle: hydrostatic stress that would exist even in the absence of convection, dynamic stress arising from convection, and viscous stress which opposes fluid motion (see Equations 2–6 in Supporting Information). To satisfy the continuity condition, these stresses must be balanced by those generated by the water (or air) column atop this boundary. If the pressure from the overlying column is hydrostatic, the resultant condition is

$$\rho_w g_s h = \rho_m g_s h + \sigma_{rr}, \tag{1}$$

where σ_{rr} incorporates deviatoric viscous stresses generated by mantle convection and dynamic pressure ($\sigma_{rr} = \tau_{rr} - p$), obtained by solving Equation 2 in Supporting Information. In practice, since values for this term are obtained by subtracting radial litho-

static stress from the total stress, values of σ_{rr} integrate to zero globally. g_s is gravitational acceleration at Earth's surface, ρ_m is the mean density for the surficial layer, and ρ_w is the density of the overlying fluid (see Table S1). Note that we do not impose additional oceanic plate cooling, e.g., due to hydrothermal circulation at ridges. Cooling and subsequent subsidence, as well as passive return flow at ridges, arise naturally from solution of the governing equations laid out in Section 2 of Supporting Information.

Surface deflection arising in response to predicted convective flow, h, is approximated by rearranging Equation 1,

$$h \approx -\frac{\sigma_{rr}}{(\rho_m - \rho_w)g_s}. \tag{2}$$

Deflections are estimated from radial stresses at times of interest (e.g., the present-day) by re-running one time-step of the TERRA model. During that time-step, a free-slip boundary condition, for which analytic approximations for surface deflection exist, is imposed instead of the plate-slip condition prescribed during the main model run routine (see Section 2.3; Ricard, 2015). The numeric models themselves apply a quasi-rigid condition at the surface, whereby flow is driven by estimates of real plate velocities (from Merdith et al., 2021), and so the surface layers behave as a series of rigid, laterally mobile plates rather than a single rigid shell. We assess the accuracy of modifying boundary conditions in this way by converting calculated deflections into the spherical harmonic domain and comparing them to predictions generated using the analytic propagator matrix approach. The consistent boundary flux (CBF) method provides an alternative means to accurately calculate normal stresses (Zhong et al., 1993). Previous benchmarking with TERRA has shown mean errors of a few percent or less for surface deflection predictions at low harmonic degrees, $l \leq 16$ (Davies et al., 2013).

2.2 Surface Deflections Calculated in the Spherical Harmonic Domain

Transforming stress, or surface deflections, calculated using numeric approaches into the frequency domain provides straightforward means of comparing results to analytic solutions and of quantifying spectral power, i.e., the magnitude of contribution to the total signal from different wavelengths. Since the models that we investigate are global in scope, we do so using spherical harmonics. The methodology for calculating spherical harmonics and the definition of power adopted in this study are included as Supporting Information. Figure 2 shows an example of surface stresses calculated using the TERRA code, their spherical harmonic representation, calculated surface deflections in the spherical harmonic domain, and associated statistics and power spectra.

Using the total power per degree convention, Hoggard et al. (2016) derived a rule-of-thumb for estimating the power spectrum of dynamic topography (see their Supporting Information), P_l^{DT}, using Kaula (1963)'s approximation for the long-wavelength gravity field of Earth as a function of l:

$$P_l^{DT} \approx \left(\frac{GM}{ZR^2}\right)^2 \left(\frac{2}{l} - \frac{3}{l^2} + \frac{1}{l^4}\right), \tag{3}$$

where G is the gravitational constant, $M = 5.97 \times 10^{24}$ kg is the mass of the Earth, $R \approx 6370$ km is Earth's radius. The value of low-degree admittance, Z, between gravity and topography varies as a function of viscosity, as well as the depth and wavelength of internal density anomalies (Colli et al., 2016). Hoggard et al. (2016) found that assuming an average value of $Z = 12$ mGal km^{-1} provides a reasonable approximation of observed residual topographic trends, thus we make use of that value in the remainder of the paper. Finally, it is useful to note that Jeans (1923) related spherical harmonic degree to wavelength λ, which at Earth's surface can be approximated via $\lambda \approx 2\pi R/\sqrt{l(l+1)}$.

2.3 Surface Deflections Calculated Analytically

The second methodology used to calculate surface deflection in response to mantle convection is the analytic propagator matrix technique (e.g., Craig & McKenzie, 1987; Gantmacher, 1959; Ghelichkhan et al., 2021; Parsons & Daly, 1983; M. A. Richards & Hager, 1984). The approach we take stems from the work of Hager and O'Connell (1981) who used Green's functions to solve the equations of motion in the spherical harmonic domain. Those solutions are used to generate sensitivity kernels that straightforwardly relate, for example, density or temperature anomalies in the mantle to surface deflections. The kernels are generated in the frequency domain, and constructed such that surface deflection sensitivity to mantle (e.g., density) anomalies is calculated as a function of depth (or radius) and wavenumber. A global spherical harmonic implementation introduced by Hager et al. (1985) has been extended to include compressibility, the effect of warping of the gravitational potential by subsurface density distributions, and radial gravity variations calculated using radial mean density values (Corrieu et al., 1995; Forte & Peltier, 1991; Hager & O'Connell, 1981; M. A. Richards & Hager, 1984; Thoraval et al., 1994).

In this study, following Ghelichkhan et al. (2021), surface deflection for each spherical harmonic coefficient, h_{lm}, is calculated in the spectral domain such that

$$h_{lm} = \frac{1}{(\rho_m - \rho_w)} \int_{R_{\mathrm{CMB}}}^{R} A_l \delta\rho_{lm}(r) \cdot \mathrm{d}r. \tag{4}$$

Products of the sensitivity kernel, A_l, and density anomalies, $\delta\rho_{lm}$, of spherical harmonic degree, l, and order, m, are integrated with respect to radius, r, between the core-mantle boundary and Earth's surface radii, R_{CMB} and R, respectively. The sensitivity kernel is given by

$$A_l = -\left(\frac{\eta_0}{R g_R}\right)\left(u_1 + \frac{\rho_w}{\rho_0} u_3\right), \tag{5}$$

where $u_n(r)$ represents a set of poloidal variables, which are posed for solution of the set of simultaneous equations by matrix manipulation, such that

$$u(r) = \begin{bmatrix} y_1\eta_0 & y_2\eta_0\Lambda & (y_3 + \bar{\rho}(r)y_5)r & y_4 r\Lambda & y_5 r\rho_0\Lambda & y_6 r^2\rho_0 \end{bmatrix}^T, \tag{6}$$

where $\Lambda = \sqrt{l(l+1)}$, and y_1 to y_6 represent the spherical harmonic coefficients of radial velocity v_r, lateral velocity $v_{\theta,\phi}$, radial stress σ_{rr}, lateral stress $\sigma_{r\theta,\phi}$, gravitational potential V, and gravitational potential gradient $\partial V/\partial r$, respectively (Hager & Clayton, 1989; Panasyuk et al., 1996). $\bar{\rho}$ is the layer mean ($l = 0$) density. The kernel A_l includes both u_1 and u_3, two terms in the matrix solution to the governing equations that affect surface topography by directly exerting stress on the surface boundary (u_1), and by changing the gravitational potential at the surface (u_3). The functional forms of calculated sensitivity kernels depend on chosen radial viscosity profiles and boundary conditions (e.g., free-slip or no-slip; Parsons & Daly, 1983).

3 Spatial and Spectral Comparison of Model Predictions

To quantify impacts of modelling assumptions and approaches used to solve the equations of motion we compare calculated surface deflections using the following metrics.

3.1 Euclidean Comparisons of Amplitudes

First, we calculate root-mean-squared difference, χ, between predicted surface deflections in the spatial domain,

$$\chi = \sqrt{\frac{1}{N}\sum_{n=1}^{N} w_\phi \left(h_n^a - h_n^b\right)^2}, \tag{7}$$

where h_n^a and h_n^b are predicted surface deflections from the two models being compared. N = number of points in the 1×1° gridded maps being compared (e.g., Figure 3b; N = 65341). The prefactor w_ϕ is proportional to $\cos\phi$, where ϕ is latitude, and is included to correct biases in cell size with latitude; mean $w_\phi = 1$. This metric is closely associated with the mean vertical distance (L^2-norm distance) between predicted and reference surfaces, i.e., $\Delta\bar{h} = 1/N \sum_{n=1}^{N} w_\phi |h_n^a - h_n^b|$. These metrics are sensitive to differences in amplitudes and locations of surface deflections.

3.2 Spectral Correlation Coefficients

Second, we use pyshtools v4.10 to compute correlation coefficients, r_l, between predicted surface deflections in the spectral domain (Wieczorek & Meschede, 2018). Correlation coefficients as a function of degree l, adapted from Forte (2007), are calculated such that

$$r_l = \frac{\sum f_1^* f_2}{\sqrt{\sum f_1^* f_1}\sqrt{\sum f_2^* f_2}}, \quad \text{where} \quad \sum = \sum_{m=-l}^{+l}, \tag{8}$$

f_1 and f_2 are the spherical harmonic coefficients of the two fields (i.e., surface deflections) being compared, which vary as a function of order, m, and l; $f = f_l^m$. * indicates complex conjugation (see also Becker & Boschi, 2002; O'Connell, 1971). This metric is sensitive to the difference between predicted and reference surface deflection signals in the frequency domain, but not to their amplitudes. To summarize spectral similarity between models concisely, we later refer to the mean value of r_l over every degree (0–50) as $\bar{r_l}$. We refer to the standard deviation of r_l across degrees as s_r.

3.3 Comparing Calculated Power Spectra

Lastly, to estimate closeness of fit between power spectra of surface deflections predicted in this study and independent estimates, we calculate

$$\chi_p = \sqrt{\frac{1}{L}\sum_{l=1}^{L}\left(\log_{10}P_l - \log_{10}P_l^K\right)^2} + \sqrt{\frac{1}{L}\sum_{l=1}^{L}\left(\log_{10}P_l - \log_{10}P_l^H\right)^2}, \tag{9}$$

where L = number of spherical harmonic degrees being compared ($L = 50$). P_l = power of predicted surface deflections generated in this study at degrees $1 \leq l \leq L$ (Equation 11 in Supporting Information). P_l^K = power of surface deflections estimated using Kaula's law (Equation 3). P_l^H = power of residual oceanic age-depth measurements from Holdt et al. (2022).

4 Model Parameterizations

The models examined in this paper are summarised in Table 1. In terms of assumptions tested there are two families of models, those with viscosity independent of tem-

Table 1. Summary of mantle convection simulations. Column labeled 'Method' indicates surface deflections calculated using either '*Numeric*' (i.e., from surface normal stresses calculated using TERRA) or '*Analytic*' (i.e., propagator matrix) approaches; '*Mixed*' indicates spherical harmonic fitting of surface stresses calculated using numeric code, enabling comparison with solutions to propagator matrix code. $\eta(r)$ indicates models with radial viscosity (e.g. independent of temperature; Models 1–10). $\eta(r,T)$ indicates models with temperature-dependent (therefore laterally varying) viscosity (Models 11–20); note that analytic Models 12–20 incorporate radial viscosity calculated using mean radial viscosity from Model 11a. †indicates with respect to Model 12. See Table 1, Section 4 and figures referred to in column 5 for details.

Model	Method	Viscosity	Parameterizations	Figures
1a	Numeric	$\eta(r)$	Full resolution numeric model	1g-h, 2a-c, S1-2
1b	Mixed	$\eta(r)$	Spherical harmonic fit to 1a	2d–i
2	Analytic	$\eta(r)$	Propagator matrix solutions	3, S3
3	Analytic	$\eta(r)$	Radial gravitation, $g(r)$	4a-c, S4
4	Analytic	$\eta(r)$	Gravitational potential terms	4d-e, S5
5	Analytic	$\eta(r)$	Removing upper 50 km of mantle	5a-b, S7a-d
6	Analytic	$\eta(r)$	Removing upper 100 km of mantle	5c-d, S7e-h
7	Analytic	$\eta(r)$	Removing upper 200 km of mantle	5e-f, S7i-l
8	Analytic	$\eta(r)$	No-slip surface, free CMB	6a-d
9	Analytic	$\eta(r)$	Free surface, no-slip CMB	6e-h
10	Analytic	$\eta(r)$	No-slip surface, no-slip CMB	6i-l
11a	Numeric	$\eta(r,T)$	Full resolution numeric model	S8-S10, S12a-c
11b	Mixed	$\eta(r,T)$	Spherical harmonic fit to 11a	7, S8-10, S12d-g
12	Analytic	$\eta(r)$	Mean radial $\eta(r,T)$ from Model 11a	7, S11, S12h-k
13	Analytic	$\eta(r)$	Decrease† radial upper mantle η	8a-b, S13a-d
14	Analytic	$\eta(r)$	Increase† radial upper mantle η	8c-d, S13e-h
15	Analytic	$\eta(r)$	Increase† radial upper mantle η	8e-f, S13i-l
16	Analytic	$\eta(r)$	Constant radial η	8g-h, S13m-p
17	Analytic	$\eta(r)$	Upper mantle densities $\times 2^{\dagger}$	8i, S14a-c
18	Analytic	$\eta(r)$	Upper mantle densities $\times 1/2^{\dagger}$	8j, S14d-f
19	Analytic	$\eta(r)$	Lower mantle densities $\times 2^{\dagger}$	8k, S14g-i
20	Analytic	$\eta(r)$	Lower mantle densities $\times 1/2^{\dagger}$	8l, S14j-l

perature (Models 1–10), and those with temperature-dependent viscosity (Models 11–20). We note that Models 12-20 incorporate mean radial viscosity from the numeric Model 11a in which viscosity depends on temperature. The two approaches used to solve the equations of motion are annotated 'Numeric' and 'Analytic' in Table 1, which refers to solutions from the TERRA and propagator matrix code, respectively. Viscosities and densities calculated using TERRA were used as input for the propagator matrix code and thus used to generate analytic estimates of surface deflection. Since analytic solutions are obtained by spherical harmonic expansion, surface deflections from TERRA were fit using spherical harmonics before predicted deflections were compared (annotated 'Mixed' in Table 1; Section 2.2). We compare predicted deflections that arise from flow across entire model domains, i.e., from the CMB to the surface. Parameterizations of these models and resultant surface deflections are discussed in the following sections, with summary statistics given in Table 2.

346

347 ## 4.1 Models with Viscosity Independent of Temperature

348 ### *4.1.1 Reference models*

349 Models 1 and 2 are the simplest explored in this paper. They were designed to be
350 as similar as possible, with a view to quantifying differences and similarities arising solely
351 from the choice of numeric or analytic methodology used to solve equations of motion
352 and to calculate surface deflections. Model 1 was parameterized with the radial viscos-
353 ity structure shown in Figure 2c. Radial viscosity used in other geodynamic studies are
354 shown alongside for comparison (Ghelichkhan et al., 2021; Mitrovica & Forte, 2004; Stein-
355 berger & Calderwood, 2006). Figure 2d shows spherical harmonic expansion of the sur-
356 face stress field predicted by Model 1 at 0 Ma (cf. Figure 2a). We call this result Model
357 1b. The original, full-resolution, numerical result is referred to as Model 1a.

358 Model 2 is the analytic model parameterized to be as similar as possible to Model
359 1. Its sensitivity kernel, generated assuming water loading ($\rho_w = 1030$ kg /m^3), free-
360 slip surface and CMB boundary conditions, and the radial viscosity profile shown in Fig-
361 ure 2c, is shown in Figure 3a. Values of the other parameters used to generate these ker-
362 nels are stated in Table S1. Similar to many previous studies, the kernel indicates that
363 surface deflections will be especially sensitive (across all degrees incorporated, $l \leq 50$)
364 to density anomalies in the upper mantle (Parsons & Daly, 1983; Hager & Clayton, 1989;
365 Ghelichkhan et al., 2021). Models 1 and 2 are used as points of reference for other more
366 complex models explored in the remainder of this paper.

367 ### *4.1.2 Gravitation*

368 We start by incorporating more complex parameterizations of gravitation. The an-
369 alytic Model 3 was parameterized in the same way as Model 2 with the addition of ra-
370 dial gravitation (following Hager & Clayton, 1989; Panasyuk et al., 1996, see Equation
371 5). The solid curve in Figure 4b shows the radial gravity function used to calculate sur-
372 face deflections. It was generated using the density distribution produced by (the nu-
373 merical) Model 1a (see Figure S1) by calculating

$$g(r) = \frac{4\pi G}{r^2}\left[\int_{R_{\mathrm{CMB}}}^{r} \bar{\rho}(r')\, r'^2\, \mathrm{d}r'\right] + F_{core}, \tag{10}$$

374 where $\bar{\rho}(r)$ is layer mean density and F is a factor chosen to account for core mass, and
375 such that $g = 9.8$ m s^{-2} at the surface. This formulation is derived from Gauss's law
376 assuming spherically symmetric density, combined with Newton's law of universal grav-
377 itation (Turcotte & Schubert, 2002).

378 The analytic Model 4 incorporates stress perturbations induced by deflections of
379 the gravitational potential field. This model assumes $g = 10$ m s^{-2} everywhere, even
380 within the deflected surface layer, as was the case for Models 1–2. Following Hager and
381 Clayton (1989) and Panasyuk et al. (1996), when solving for surface deflection using prop-
382 agator matrices, the effect on flow of perturbation of gravitational potential is included
383 via the u_3 term in Equation 6 (see also Ribe, 2007; Ricard, 2015). Sensitivity kernels for
384 Models 3 and 4 are shown in Figure S6. TERRA simulations do not include this com-
385 ponent in flow calculations (see Supporting Information).

386 ### *4.1.3 Discarding Shallow Structure*

387 The uppermost few hundred kilometers of geodynamic simulations are often not
388 included in predictions of surface deflections (see e.g. Flament et al., 2013; Flament, 2018;

Davies et al., 2019, and references therein). To quantify the impact of discarding shallow structure on our calculations, we examine differences in calculated deflections in the spatial and spherical harmonic domains. We present three tests, resulting in Models 5, 6 and 7, where structure shallower than 50, 100 and 200 km is removed from Model 2.

4.1.4 Changing Boundary Conditions

Up to now, we have only considered instantaneous analytic and numeric solutions for surface deflection where both the surface and CMB have free-slip conditions imposed (i.e., vertical component of flow velocity $\mathbf{u_r} = 0$, horizontal components are allowed to freely vary). No gradient/Neumann constraint (e.g., on $\partial\mathbf{u}/\partial z$) is imposed. This condition is generally deemed appropriate for the surface of the convecting mantle, and CMB, since at both boundaries, cohesion within convecting mantle is thought to be much stronger than adhesion to the boundary. Analytic solutions for sensitivity kernels for propagator matrices also exist for no-slip Dirichlet boundary conditions, where horizontal components of $\mathbf{u} = 0$, which may be more appropriate when the Earth's lithosphere is implicitly included in mantle convection models, as is the case here (Parsons & Daly, 1983; Thoraval & Richards, 1997). Therefore, we test the effect of changing the surface boundary condition to no-slip on predicted surface deflections (Model 8). Although there is little reason to believe the adhesion of the CMB would be strong, for completeness, we test scenarios in which no- and free-slip conditions are assumed for the CMB and the surface, respectively (Model 9), and both have no-slip conditions (Model 10).

4.2 Models with Temperature-Dependent Viscosity

We investigate the impact of including the temperature dependence of viscosity, $\eta(r, T)$, on predicted global mantle flow in numeric models, and on subsequent estimates of surface deflection. We do so by first generating the numeric Model 11, which is identical to Model 1 in terms of all boundary conditions, initialization, and physical parameters, except for the fact that viscosity depends on temperature in the manner described by Equation 7 in Supporting Information.

The radial distribution of viscosity, but not its absolute value, plays a crucial role in determining sensitivity of instantaneous solutions for surface deflections to density (and thermal) anomalies in the mantle (e.g., Parsons & Daly, 1983; Hager, 1984). Consequently, to assess sensitivity of surface deflections to arbitrary changes to radial viscosity, $\eta(r)$, we performed a suite of analytic tests. Since the analytic approaches require viscosity to only vary as a function of radius, we first test the impact of inserting layer-mean viscosity from the present-day 3D temperature-dependent viscosity structure predicted by numeric Model 11 (Figure S8). This parameterization is used to generate (the analytic) Model 12. The sensitivity kernel for Model 12 is shown in Figure S11a.

We stress that in Models 3–10 analytic instantaneous solutions for surface deflection, with adjusted parameters and boundary conditions, were simply compared with Model 2; no new numeric models were generated using TERRA. In contrast, the additional tests examined here correspond to a new TERRA model (Model 11) in which temperature dependence of viscosity affects mantle flow across the entire run time.

The sensitivity of surface deflections to arbitrary modification of upper and lower mantle viscosity and densities were then examined. Mean upper and lower mantle (radial) temperature-dependent viscosity was decreased or increased by an order of magnitude from that used to generate Model 12 (see solid black curve in Figure 8). The resultant impact on calculated surface deflections (Models 13–16) was quantified by comparison with results generated using reference Model 12 (Figure S11). Figures 8i–l and S14 show the amplitudes of density anomalies in the upper and lower mantle that were systematically increased or decreased to generate Models 17–20. Similar to the tests shown

in Figures 8a–h and S13, densities are amplified relative to Model 12. Radial viscosity is constant for each of these tests (black curve in Figure 8a; i.e., same as that used to generate Model 12).

5 Results

5.1 Models with Viscosity Independent of Temperature

5.1.1 Reference Models: Comparing Numeric and Analytic Solutions

We first compare solutions generated from numeric Model 1a, with its spherical harmonic representation (Model 1b), and analytic Model 2, which were designed to be as similar as possible. Figure 1g–h shows calculated densities that arise in Model 1a at 0 and 100 Ma (see Figure S1 for extended results). The history of plate motions used to drive these models is also indicated on these figures. The resultant normal stresses, σ_{rr}, calculated at the surface of Model 1, and associated statistics are shown in Figure 2a–b. By convention, positive stresses imply compression and hence downward surface deflection, which could be manifest as lithospheric drawdown, i.e., subsidence. Prominent regions of positive stress anomalies in this model include locations atop imposed collision zones, where subduction naturally results, e.g., along the Pacific margin of South America. Negative stresses imply dilation and hence positive lithospheric support (i.e., surface uplift). Figure 2a shows dilatational stresses beneath Southern Africa, for example, and along mid-oceanic ridges in the Indian and Atlantic Oceans.

Surface stresses calculated by fitting radial stresses from Model 1a with a global spherical harmonic interpolation up to maximum degree $l = 50$, i.e., minimum wavelength of ≈ 800 km, is shown in Figure 2d–e. The resultant power spectrum in terms of total power at each degree is shown in Figure 2f. Aside from the lack of structure at degree 0, amplitudes decrease steadily with increasing degree (i.e., decreasing wavelength) and can be approximated by red noise. The spherical harmonic representation of deflections calculated by converting stress using Equation 2, assuming water loading, are shown in Figures 2g and S2. A comparison of calculated power spectra, expected surface deflection from Kaula's rule (Equation 3), and spectra generated from observed residual ocean age-depth measurements is also included in Figures 2 and S2 (Kaula, 1963; Hoggard et al., 2016; Holdt et al., 2022). For completeness, surface deflections calculated assuming air loading are shown in Figure S2f-j.

Surface deflections predicted by Model 2 and its associated sensitivity kernel are shown in Figure 3a-b. An expanded set of results including sensitivity kernels for water and air loading, and histograms of deflection and associate power spectra are included in Figure S3.

Deflections predicted from these numeric and analytic models are visually similar (cf. Figures 2g & 3b). Absolute differences in amplitudes are greatest close to subduction zones (e.g., in South America and Asia; Figure 3c). The differences are broadly normally distributed and centred on 0 (Figure 3d). The spherical harmonic correlation between these models is high (close to 1 for all degrees; cf. Forte, 2007, Figure 3e). The ratios between surface deflection values in these predictions indicate that analytic solutions tend to be damped compared to numeric solutions. This result is emphasized by the histogram shown in Figure 3g. Multiplying amplitudes of deflections from the propagator matrix solutions by a factor of 1.1 brings them in-line with the numeric solutions. These results indicate that the propagator matrix approach dampens solutions by $\approx 10\%$. We note that power spectral slopes between Model 1b and 2 are similar (cf. Figures 2i and S3d). These and all other results are discussed in Section 6.

5.1.2 Incorporating Self-Gravitation and Gravitational Potential of the Deflected Surface

Differences in deflections predicted by Model 2, which assumes constant $g = 10$ m s^{-2} across all radii, and Model 3, which incorporates self-consistently calculated radial gravitation, are shown in Figure 4a and 4c. Deviations in predicted instantaneous deflections are $\sim 10\%$ of maximum amplitudes predicted by Model 2 (see Table 2). Note that, for the viscosity structure used in these models, changing g in this way impacts sensitivity kernels most at low degrees $l \lesssim 10$ in the mid-mantle (see Figures 2c, 3a and S6).

We suggest that the broadly hemispherical differences in calculated deflections arise from three contributing factors. First, deviations in g between the two models are greatest in the mid-mantle, which, secondly, results in subtly different sensitivity kernels (see Figure S6). In general, surface deflection sensitivity to mid-mantle structure is highest at low degrees (l =1–3), and is almost negligible at higher degrees compared to contributions from the near-surface. Thus it seems likely that differences between these kernels would be manifest in low-degree (e.g. hemispherical) differences in surface deflections. Third, in the final timestep, which is used to calculate deflections, there occurs a greater proportion of negative and positive deflections in the northern and southern hemispheres, respectively.

We note that incorporating radially varying gravitation into numeric simulations, which is not trivial, might materially impact calculated mantle flow fields and hence predictions of surface deflections. Our results are consistent with the rule of thumb outlined in Section 7.02.2.5.2 of Ricard (2015), whereby magnitudes of differences incurred by inclusion of full self-gravitation, i.e., $g(\theta, \phi, r)$, decay as a function of spherical harmonic degree, proportionately to $3/(2l + 1)$.

As expected, induced differences in surface displacement predictions are much lower in magnitude when gravitational potential of the deflected surface is included compared to when radial gravitation is incorporated (cf. Figure 4a and 4d). We note that they are of the same order of magnitude as the geoid height anomalies predicted by these models. The mean Euclidean distance between the two predicted surfaces in Models 2 and 4 is only $\sim$110 m (compared to maximum amplitudes > 8 km), and the spherical harmonic correlation is very high across all degrees (see Table 2). Similar to the results for Model 3, the differences are concentrated at low spherical harmonic degree l. We stress that this test investigates the effect of the u_3 term on instantaneous solution for surface deflection (Equation 5). It cannot be ruled out from this test that inclusion of the effect of gravitational potential field perturbation would result in greater differences across the entire model run time of a numeric model, although it is unlikely (Zhong et al., 2008).

5.1.3 Excising Shallow Structure

As expected from examination of surface deflection sensitivity kernels (e.g., Figure 3a), removal of shallow structure (Models 4–6) results in significantly reduced amplitudes of surface deflections (Figure 5). Doing so results in amplitudes of power spectra that more closely align with independent estimates (Figure 5b, f, j). The reduction in differences is largely due to the fact that the reference Model 2 has surface deflections that are much larger than independent estimates of dynamic topographic power across all degrees. We note that power spectral slopes for predicted surface deflection from Model 2 are close to those generated from Kaula's rule, and observed oceanic residual depths (Figures 2i, S2 and S3). Removing shallow structure steepens spectral slopes (i.e., reduces power at high degrees) beyond those expected from theoretical considerations (Kaula's rule) or observed from oceanic residual depths, akin to results from other work that excised shallow structure (e.g., Flament et al., 2013; Moucha et al., 2008; Steinberger, 2007). This result is emphasized by calculated spectral coherence, r_l, between deflections with

and without shallow structure removed (cf. Figure 5b, d, f). While degree 1 and 2 structure remains coherent, coherence across degrees $\gtrsim$ 20 decreases from $\sim$ 0.9 to as low as 0.5, which are the largest discrepancies between any models examined in this study (Figure S7).

5.1.4 Adjusting Boundary Conditions

Figure 6a, e and i show predicted sensitivity kernels as a function of depth and degree, for no-slip/free-slip, free-slip/no-slip and no-slip/no-slip boundaries respectively, where the first condition is the surface slip condition, and the second the CMB slip condition. Differences to the sensitivity kernel for Model 2 (free-slip/free-slip; Figure 3a) are shown in panels b, f and j. Those panels, and panels c, g and k, demonstrate that when the surface boundary condition is 'no-slip', there is decreased sensitivity to short wavelength shallow structure, and increased sensitivity to long-wavelength (low degree) structure across all depths. Figure 6d, h and l reveal that induced misfit in the spatial domain is impacted to a greater degree than in tests of gravitation (Models 3 & 4), but not necessarily more severely than for removal of, say the upper 200 km of density structure from surface deflection calculations. Spectral correlation with Model 2 is most severely impacted when both surface and CMB boundaries are no-slip, which is probably physically unrealistic (Model 7; see Table 2; Section 4.1.4).

5.2 Adjusting Viscosity and Density Anomaly Amplitudes

5.2.1 Temperature-Dependent Viscosity

Slices through the three-dimensional viscosity and density structure of Model 11, which incorporated temperature-dependent viscosity, are shown in Figure 1a, c and e. Density anomalies in the models parameterized with temperature-dependent viscosity are more localised ('sharper') than in the models with viscosity independent of temperature (e.g., Model 1; see Figures 7 & S8–S10). This result is unsurprising since temperature-dependent viscosity provides stronger mechanical contrasts between cooler subducting regions and surrounding asthenosphere (cf. Figure 1g–h & S9; Zhong et al., 2000). Nonetheless, power spectra of calculated surface deflections are very similar (cf. Figure S10j & 2i). This result emphasises the relatively small impact incorporating temperature-dependent viscosity has on surface deflections compared to, say, excising shallow structure.

Calculated power spectra from the analytic Model 12, which was generated using layer-mean (radial) viscosity from Model 11a, reinforces this view (cf. Figure S3a-d & Figure S11a-d). Similar to the results obtained for models without temperature-dependent viscosity (Figure 3), deflections calculated analytically are damped relative to numeric solutions (see Figure 7f). The best fit amplification factor to align propagator matrix and numeric solutions is 1.24 (24%). The effect is greater than that seen when comparing Models 1b and 2 because of increased short wavelength structure in Model 11 (see also Zhong et al., 2000). Nonetheless, spherical harmonic correlations, r_l, are > 0.75 for all degrees examined ($l \leq 50$), and > 0.85 for most degrees. Cell-to-cell differences in surface deflections are broadly normally distributed and centred on zero (Figure 7d).

A summary of comparisons between models with and without temperature-dependent viscosity is shown in Figure S12. Discrepancies in cell-to-cell deflections are broadly normally distributed and centred on zero, clustering along the 1:1 relationship with maximum $\chi = 1.51$ for full resolution (numeric) models (Figure S12b-c; see Table 2). Unsurprisingly, spherical harmonic fits and analytic results have tighter normal distributions and lower χ values. Correlation coefficients are > 0.75 for nearly all degrees in all comparisons.

5.2.2 Sensitivity to Upper/Lower Mantle Viscosity and Density Anomalies

In order to explore the consequences of modified viscosity and density on calculated deflections we also systematically increased and decreased contrasts in the upper and lower mantle (Models 13–20) with respect to Model 12. Figure 8 summarises the results, which include decreasing upper mantle viscosity by an order of magnitude and show the impact of using increasingly simple radial viscosity in analytic calculations. Calculated sensitivity kernels for the adjusted viscosity profiles demonstrate that decreasing upper mantle viscosity reduces sensitivity of surface deflections to long-wavelength density structure, especially in the lower mantle (Figures S13 & 8d, f, h). Models 13–16 have broad similarities with the reference Model 12 even when $\eta(r)$ is drastically varied: average χ misfit = 0.17–0.38 km, and $r_l > 0.97$ across all degrees. These results emphasize that the viscosity adjustments we examined exert a relatively minor control on the amplitudes of instantaneous surface deflection (Table 2, see, e.g., Ghosh et al., 2010; Moucha et al., 2007; Lu et al., 2020).

In contrast, increasing (Model 17) or decreasing (Model 18) upper mantle densities is much more impactful on amplitudes of calculated surface deflections (see Figure 8i–l, and S14). For instance, increasing or decreasing upper mantle densities by a factor of two (relative to Model 12) results in χ values of 0.97 and 0.48, respectively. Modifying lower mantle densities has a much smaller impact on amplitudes of deflection (Models 18 & 19). Spherical harmonic correlation between models is approximately as good as for the radial viscosity tests (Models 13–16), which is to be expected since we do not vary locations of density anomalies here, only their amplitudes, and r_l is insensitive to amplitudes of the two results being compared. Significant is the fact that mean vertical differences between Models 17–20 and 12 (i.e., χ and $\Delta\bar{h}$) are higher than those calculated for Models 13–16 (in which viscosity is varied; see Table 2).

These results emphasize the relative sensitivity of instantaneous surface deflections to upper mantle density anomalies compared to, say, radial viscosity or lower mantle densities. Even quite large uncertainties in lower mantle density anomalies have relatively little impact on instantaneous surface deflections. These results reinforce the view that accounting for shallow (e.g., lithospheric and asthenospheric) densities is crucial when estimating surface deflection, and dynamic topography, from mantle convection simulations (e.g., Colli et al., 2016; Flament et al., 2013; Holdt et al., 2022; Wang et al., 2022).

6 Discussion

6.1 Similarities of Analytic and Numeric Solutions

In this paper we compare numeric and analytic predictions of instantaneous surface deflections generated by mantle convection simulations. First, we simply compared predictions from numeric and analytic approaches parameterised to be as similar as possible. In this test, the models were purposefully simple: viscosity is radial, models are incompressible, and they do not include self-gravitation, or radial variation in g. Numeric solutions were transformed into the frequency (spherical harmonic) domain so that they could be compared with analytic solutions, and so that power spectra could be directly compared at appropriate scales. The results show that, for as-similar-as-possible parameterizations, amplitudes of analytic solutions are $\approx 10\%$ lower than numeric solutions (Figure 3). If the numeric model incorporates temperature-dependent viscosity, this discrepancy increases to 25% (Figure 7). We interpret these results in two ways. First, once armed with viscosity and density fields, numeric and analytic approaches broadly yield

Table 2. Inter-model comparison of predicted surface deflections. Models being compared are summarised in Table 1. Metrics: root-mean-squared difference (χ, km), mean Euclidean (L^2-norm) difference in predicted deflection ($\Delta\bar{h}$, km), and mean spherical harmonic correlation between models ($\bar{r}_l$). Standard deviation of r_l distribution across degrees (s_r) is also stated: note that $r_l \leq 1$. All spherical harmonic representations of output from numeric code and generated by the propagator matrix code are expanded up to maximum degree, $l = 50$. See body text, figures referred to in column 6, and Table 1 for details.

Models	χ	$\Delta\bar{h}$	$\bar{r}_l$	s_r	Figures
1b & 2	0.95	0.69	0.97	0.02	3
2 & 3	0.57	0.47	0.99	4×10^{-4}	4
2 & 4	0.13	0.11	0.99	2×10^{-5}	4
2 & 5	0.67	0.48	0.93	0.04	5a-b
2 & 6	1.03	0.74	0.87	0.06	5c-d
2 & 7	1.57	1.12	0.63	0.15	5e-f
2 & 8	1.26	1.04	0.99	1×10^{-3}	6a-d
2 & 9	1.09	0.97	0.99	0.04	6e-h
2 & 10	1.00	0.74	0.96	0.28	6i-l
1a & 11a	1.51	1.04	—	—	S12a-c
1b & 11b	1.44	0.98	0.79	0.26	S12d-g
11b & 12	1.20	0.80	0.95	0.02	7
2 & 12	0.92	0.64	0.85	0.27	S12h-k
12 & 13	0.31	0.20	0.99	9×10^{-3}	8a-b, S13a-d
12 & 14	0.17	0.10	0.99	3×10^{-3}	8c-d, S13e-h
12 & 15	0.32	0.20	0.98	0.01	8e-f, S13i-l
12 & 16	0.38	0.23	0.98	0.01	8g-h, S13m-p
12 & 17	0.97	0.64	0.98	7×10^{-3}	8i, S14a-c
12 & 18	0.48	0.32	0.98	6×10^{-3}	8j, S14d-f
12 & 19	0.43	0.29	0.99	3×10^{-3}	8k, S14g-i
12 & 20	0.22	0.14	0.99	1×10^{-3}	8l, S14j-l

similar estimates of surface deflections. Second, the relatively damped analytic solutions are a consequence of smoothing steps in the propagator matrix approach.

The smoothness of analytic solutions, and subsequent damping of topographic amplitudes, is perhaps surprising, given the fact that they are being compared with numeric models expanded into the spherical harmonic domain to the same maximum degree, $l = 50$. However, the surface stresses used to generate Model 1a have full horizontal resolution (≈ 45 km) across depths, and *only* the surface layer is smoothed by spherical harmonic fitting, to generate Model 1b. Therefore, Model 1b inherently contains some contribution from degrees ≥ 50, in the sense that finer-resolution density structure at depth could affect longer-wavelength flow nearer the surface. In contrast, to generate the analytic solution (Model 2), the density structure of each layer of the model is smoothed, by expansion to maximum $l = 50$, *before* integration of their contributions to surface deflection. The analytic solution would provide a better match to stress estimates from numeric models if such estimates were calculated using density structure smoothed to the same maximum l across all depths, which is currently challenging (see Section 1.1).

Nonetheless, the similarity of results indicates that the relatively low-cost propagator matrix approach can be used to explore consequences of including additional model complexity. A systematic sweep of parameters, including radial gravitation (Figure 4a-c) and gravitational potential field effects (Figure 4d-e) indicates that their effects on surface deflection are relatively modest. A useful rule of thumb is that self-gravitation perturbs instantaneous surface deflections by $O(1\text{–}10)\%$ when compared to models with constant gravitational acceleration, and even less difference is observed at high degree (e.g., Ricard, 2015, their Section 7.02.2.5.2). Incorporating the effect of deflections of gravitational potential field on flow has a modest impact on amplitudes of surface deflections at degrees 1–2, but overall it contributes even less than radial variation in g to surface deflections across the scales of interest. We note that incorporating full 3-D self-gravitation into numeric simulations is currently challenging. Nonetheless, establishing its impact on the flow field over time, and resultant impact on surface deflections, may be important future work.

6.2 Importance of Viscosity and Shallow Density Anomalies for Isolating Dynamic Support

Figure 8 demonstrates that even quite large (order of magnitude) variations in viscosity do not have much impact on instantaneous surface deflections when compared to, say, modified upper mantle density anomalies, which appears to agree with the results of Davies et al. (2019) (see also Flament, 2019; Steinberger et al., 2019). Assuming no-slip boundary conditions at Earth's surface may be appropriate for driving near-surface (lithospheric) flow throughout the main model run time, but it less clear whether no- or free-slip boundary conditions are most appropriate for calculating instantaneous dynamic topography (see, e.g., Forte & Peltier, 1994; Thoraval & Richards, 1997). Nonetheless, all calculated sensitivity kernels in this study indicate that shallow density anomalies make significant contributions to surface topography regardless of viscosity profile or boundary conditions chosen (e.g., Figure 3a; see also Colli et al., 2016; Parsons & Daly, 1983).

It is well known that disentangling contributions to Earth's surface topography from mantle convection, lithospheric isostasy and flexure is important but not trivial (see, e.g., Davies et al., 2019; Cao & Liu, 2021; Fernandes & Roberts, 2021; Hoggard et al., 2021; Steinberger, 2016; Stephenson et al., 2021; Zhou & Liu, 2019; Wang et al., 2022). Previous studies simulating mantle convection have addressed this issue by discarding density anomalies in radial shells shallower than specified depths before calculating surface stresses (e.g., Spasojevic & Gurnis, 2012; Flament et al., 2013; Molnar et al., 2015). Similarly, analytic approaches have isolated contributions from the convecting mantle by only

incorporating information from deep shells (e.g., Colli et al., 2018). This method has the advantage of effectively removing the effect of lithospheric cooling through time from surface deflection estimates. It also avoids the need to incorporate, say, realistic crustal or depleted lithospheric layers within the viscous flow parameterization. However, uncertain oceanic and continental lithospheric thicknesses mean that choosing appropriate cut-off depths is not simple.

Out of all the tests performed in this study, removing shallow structure resulted in the largest impact on predicted surface deflections. It modifies amplitudes of deflections, locations of uplift and subsidence, and degrees over which they are resolved, and hence modifies power spectral scalings (Table 2, Figure 5). Making quantitative predictions of dynamic topography from such an approach is fraught for at least two reasons. First, if the chosen depth is shallower than the lithosphere-asthenosphere boundary in places, plate and sub-plate contributions to topography will be entangled. Second, discarding deeper layers to ensure that all plate contribution is definitely avoided means that some contributions from asthenospheric flow will be missed. Thus, such a step is unlikely to be desirable if mantle flow models are to be used to understand, say, lithospheric vertical motions, or vice versa (see e.g., Figure 3a; Davies et al., 2019; Hoggard et al., 2016). Given the calculated sensitivity kernels, excising layers in the upper few 100 km is likely to result in predictions of surface deflections that are especially inaccurate at short wavelengths, i.e., high spherical harmonic degree. An alternative approach, which may be fruitful future work, is removal of structure based on appropriately calibrated plate models, or globally averaged age-dependent density trends (e.g., F. D. Richards et al., 2020, 2023).

6.3 Assessing 'Effective' Contributions to Instantaneous Deflections

The results emphasise the importance of considering sensitivities of instantaneous vertical surface deflections to the location and scale of flow in the mantle. Taking inspiration from Hager and O'Connell (1981) and Parsons and Daly (1983), we calculate the net contributions from density anomaly structure to deflections, as a function of radius, latitude and longitude across all spherical harmonic degrees considered (i.e., $l = 1$ to 50). Contributions to deflections from densities at particular radii r, across all spherical harmonic degrees and orders, for each latitude and longitude, (θ, ϕ), are calculated such that

$$h_e(\theta, \phi, r) = \sum_{l=1}^{L} \sum_{m=-l}^{m=l} \left[Y_{lm}(\theta, \phi) \cdot \delta\rho_{lm}(r) \cdot A_l(r) \cdot \Delta r \right], \tag{11}$$

where Δr is the radial width of the spherical shell included in the calculation (≈ 45 km for all shells from the surface to the CMB; see Supporting Information) and Y_{lm} are spherical harmonic coefficients. Mean density anomalies, $\delta\rho_{lm}$, within each shell at each latitude and longitude, and sensitivities A_l at the top of each shell are used to calculate h_e (see Section 2.3). Contributions at specific locations to surface deflections as a function of latitude and longitude, and spherical shell depth are shown in Figure 9 for Model 12, for $1 \leq l \leq 50$. Results for lower maximum degrees are shown in Supporting Information. Panels a-d show slices through effective density in the upper (at 45, 135, 360 km) and lower mantle (1445 km). A 180° cross-section showing effective densities from the core-mantle-boundary to the surface beneath the Pacific to the Indian Ocean encompassing South America and southern Africa (the same transect as shown in Figure 1) is shown in panel e. This figure again emphasizes the contribution of density anomalies in the upper mantle to surface deflections, and the risks associated with discarding shallow structure when predicting dynamic topography.

6.4 Summary and Future Work

Encouragingly, although predicted instantaneous surface deflections are sensitive to different parameterizations, broadly coherent patterns emerge in all models tested. Moreover, calculated deflections are relatively insensitive to the methodologies used to solve the equations of motion. For instance, incorporation of gravitational potential of deflected surfaces, self-gravitation and viscosity anomalies each generate subtly different surface deflections. Choosing to solve the equations of motion analytically or numerically changes calculated deflections by $< 25\%$, even when temperature-dependent viscosity is included throughout the duration of a simulation.

In contrast, removal of shallow structure produces much larger discrepancies between predicted deflections. For instance, surface deflections calculated using the entire modelling domain (core-mantle boundary to surface) have spectral slopes consistent with those of oceanic age-depth residuals, however amplitudes are over-predicted by 1–2 orders of magnitude. In contrast, by not including the shallowest 200 km, calculated power spectra more closely match observed amplitudes, especially at spherical harmonic degrees > 10 (Figure 5). However, the spectral slopes of predicted deflections are redder than for the oceanic residuals, which implies that a different approach to removing the contribution of lithospheric structure is required.

An obvious necessary next step for accurately predicting modern dynamic support from mantle convection simulations is to incorporate accurate information about lithospheric structure from, for instance, tomographic models (e.g., Priestley & McKenzie, 2013; F. D. Richards et al., 2020). Another useful next step is to establish sensitivity of surface deflections to time-dependent parameters that impact predicted flow histories, including plate motions. The results in this paper indicate that comparing predicted and observed surface deflections, combined with knowledge of lithospheric structure, could be used to identify optimal models.

Finally, the body of geologic and geomorphologic observations that could be used to test predicted histories of surface deflections from mantle convection simulations has grown substantially in the last decade (e.g., uplift and subsidence histories; Section 1; see, e.g., Hoggard et al., 2021, and references therein). A suite of other geologic and geophysical observables are also predicted by, or can be derived from, such simulations (e.g., mantle temperatures, heat flux, geoid, seismic velocities, true polar wander). Using them alongside histories of surface deflections to identify optimal simulations is an obvious avenue for future work (e.g., Ball et al., 2021; Lau et al., 2017; Panton et al., 2023; F. D. Richards et al., 2023). Using such data and the methodologies explored in this paper may be a fruitful way of identifying optimal simulations from the considerable inventory that already exists.

7 Conclusions

This study is concerned with quantifying sensitivities and uncertainties of Earth's surface deflections that arise in simulations of mantle convection. Calculated sensitivities of instantaneous deflection of Earth's surface to mantle density structure emphasise the importance of accurate mapping of the upper mantle. Surface deflections are somewhat sensitive to the distribution of viscosity throughout the mantle, but especially to the locations and scales of density anomalies in the upper mantle. The largest discrepancies between predicted deflections seen in this study are generated when upper mantle structure is excised or altered. Doing so changes both the amplitude and distribution of calculated deflections, modifying their power spectral slopes. These results emphasise the importance of incorporating accurate models of lithospheric structure into calculation of sub-plate support of topography, and also the need to accurately determine plate contributions to topography. In contrast, the choice of methodology to es-

timate surface deflections—analytic or numeric—or boundary conditions are relatively small sources of uncertainty. Similarly, assumed gravitational profiles and temperature dependence of viscosity are relatively minor contributors to uncertainty given reasonable, Earth-like, parameterizations. Nonetheless, these parameterizations may impact surface deflections through their role in determining how upper mantle flow evolves through geologic time. A fruitful next step could be to use the approaches developed in this paper, in combination with careful isolation of plate cooling signatures from surface deflection predictions, to test mantle convection simulations using the existing and growing body of geologic, geomorphologic and geophysical observations.

Open Research Section

TERRA models are archived [here]. The propagator matrix code is archived [here]. Parameterization files are archived [here]. [TO ED: this section will be completed upon final submission, when confirmation of the precise models published is obtained after review.]

Acknowledgments

We thank A. Biggin, H. Brown, C. Davies, A. Ferreira, M. Holdt, P. Japsen, P. Koelemeijer, F. M^{c}Nab, R. Myhill and J. Ward for helpful discussion. We also thank N. Flament and an anonymous reviewer for helping us to clarify our thesis. C.O., J.P. and V.M.F. were supported by NERC Grant NE/T01684/1.

References

Al-Hajri, Y., White, N., & Fishwick, S. (2009). Scales of transient convective support beneath Africa. *Geology*, *37*(10), 883–886. doi: 10.1130/G25703A.1

Bahadori, A., Holt, W., & Feng, R. e. a. (2022). Coupled influence of tectonics, climate, and surface processes on landscape evolution in southwestern North America. *Nat Commun*, *13*(4437). doi: 10.1038/s41467-022-31903-2

Ball, P. W., Duvernay, T., & Davies, D. R. (2022). A coupled geochemical-geodynamic approach for predicting mantle melting in space and time. *Geochemistry, Geophysics, Geosystems*, *23*, 1–31. doi: 10.1029/2022gc010421

Ball, P. W., White, N. J., Maclennan, J., & Stephenson, S. N. (2021). Global Influence of Mantle Temperature and Plate Thickness on Intraplate Volcanism. *Nature Communications*, *12*(2045), 1–13. doi: 10.1038/s41467-021-22323-9

Bangerth, W., Dannberg, J., Fraters, M., Gassmoeller, R., Glerum, A., Heister, T., ... Naliboff, J. (2023). ASPECT v2.5.0 [Computer software manual]. Retrieved 2023-08-04, from `https://zenodo.org/record/3924604` doi: 10.5281/zenodo.8200213

Bauer, S., Huber, M., Ghelichkhan, S., Mohr, M., Rüde, U., & Wohlmuth, B. (2019). Large-scale simulation of mantle convection based on a new matrix-free approach. *Journal of Computational Science*, *31*, 60–76. Retrieved from `https://doi.org/10.1016/j.jocs.2018.12.006` doi: 10.1016/j.jocs.2018.12.006

Baumgardner, J. R. (1985). Three-dimensional treatment of convective flow in the Earth's mantle. *Journal of Statistical Physics*, *39*(5-6), 501–511. doi: 10.1007/BF01008348

Becker, T. W., & Boschi, L. (2002). A comparison of tomographic and geodynamic mantle models. *Geochemistry, Geophysics, Geosystems*, *3*(1), 1–48. doi: 10.1029/2001GC000168

Biggin, A. J., Steinberger, B., Aubert, J., Suttie, N., Holme, R., Torsvik, T. H., ... Van Hinsbergen, D. J. (2012). Possible links between long-term geomagnetic variations and whole-mantle convection processes. *Nature Geoscience*, *5*(8),

526–533. doi: 10.1038/ngeo1521

Braun, J. (2010). The many surface expressions of mantle dynamics. *Nature Geoscience*, *3*(12), 825–833. doi: 10.1038/ngeo1020

Bunge, H.-P., & Baumgardner, J. R. (1995). Mantle convection modeling on parallel virtual machines. *Computers in Physics*, *9*(2), 207–215. doi: 10.1063/1.168525

Bunge, H.-P., Hagelberg, C. R., & Travis, B. J. (2003). Mantle circulation models with variational data assimilation: inferring past mantle flow and structure from plate motion histories and seismic tomography. *Geophysical Journal International*, *152*, 280–301. doi: 10.1046/j.1365-246X.2003.01823

Bunge, H.-P., Richards, M. A., & Baumgardner, J. R. (2002). Mantle-circulation models with sequential data assimilation: Inferring present-day mantle structure from plate-motion histories. *Philosophical Transactions of the Royal Society A: Mathematical, Physical and Engineering Sciences*, *360*(1800), 2545–2567. doi: 10.1098/rsta.2002.1080

Cao, Z., & Liu, L. (2021). Origin of Three-Dimensional Crustal Stress Over the Conterminous United States. *Journal of Geophysical Research: Solid Earth*, *126*(11), e2021JB022137. (e2021JB022137 2021JB022137) doi: https://doi.org/10.1029/2021JB022137

Chang, C., & Liu, L. (2021). Investigating the formation of the Cretaceous Western Interior Seaway using landscape evolution simulations. *GSA Bulletin*, *133*(1-2), 347–361. doi: 10.1130/B35653.1

Colli, L., Ghelichkhan, S., & Bunge, H.-P. (2016). On the ratio of dynamic topography and gravity anomalies in a dynamic Earth. *Geophysical Research Letters*, *43*, 2510–2516. doi: 10.1002/2016GL067929

Colli, L., Ghelichkhan, S., Bunge, H.-P., & Oeser, J. (2018). Retrodictions of Mid Paleogene mantle flow and dynamic topography in the Atlantic region from compressible high resolution adjoint mantle convection models: Sensitivity to deep mantle viscosity and tomographic input model. *Gondwana Research*, *53*, 252–272. doi: 10.1016/j.gr.2017.04.027

Corrieu, V., Thoraval, C., & Ricard, Y. (1995). Mantle dynamics and geoid Green functions. *Geophysical Journal International*, *120*(2), 516–523. doi: 10.1111/j.1365-246X.1995.tb01835.x

Craig, C. H., & McKenzie, D. (1987). Surface deformation, gravity and the geoid from a three-dimensional convection model at low Rayleigh numbers. *Earth and Planetary Science Letters*, *83*, 123–136. doi: 10.1016/0012-821X(87)90056-2

Crameri, F., Schmeling, H., Golabek, G. J., Duretz, T., Orendt, R., Buiter, S. J., ... Tackley, P. J. (2012). A comparison of numerical surface topography calculations in geodynamic modelling: An evaluation of the 'sticky air' method. *Geophysical Journal International*, *189*(1), 38–54. doi: 10.1111/j.1365-246X.2012.05388.x

Czarnota, K., Hoggard, M. J., White, N., & Winterbourne, J. (2013). Spatial and temporal patterns of Cenozoic dynamic topography around Australia. *Geochemistry, Geophysics, Geosystems*, *14*(3), 634–658. doi: 10.1029/2012GC004392

Dannberg, J., Eilon, Z., Faul, U., Gassmöller, R., Moulik, P., & Myhill, R. (2017). The importance of grain size to mantle dynamics and seismological observations. *Geochemistry, Geophysics, Geosystems*, *18*(8), 3034-3061. doi: 10.1002/2017GC006944

Davies, D. R., Davies, J. H., Bollada, P. C., Hassan, O., Morgan, K., & Nithiarasu, P. (2013). A hierarchical mesh refinement technique for global 3-D spherical mantle convection modelling. *Geoscientific Model Development*, *6*(4), 1095–1107. doi: 10.5194/gmd-6-1095-2013

Davies, D. R., Ghelichkhan, S., Hoggard, M. J., Valentine, A. P., & Richards, F. D.

(2023). Observations and Models of Dynamic Topography: Current Status and Future Directions. In J. Duarte (Ed.), *Dynamics of plate tectonics and mantle convection* (pp. 223–269). Elsevier. doi: 10.1016/B978-0-323-85733-8.00017-2

Davies, D. R., Valentine, A. P., Kramer, S. C., Rawlinson, N., Hoggard, M. J., Eakin, C. M., & Wilson, C. R. (2019). Earth's multi-scale topographic response to global mantle flow. *Nature Geoscience*, *12*, 845–850. doi: 10.1038/s41561-019-0441-4

Fernandes, V. M., & Roberts, G. G. (2021). Cretaceous to Recent net continental uplift from paleobiological data: Insights into sub-plate support. *GSA Bulletin*, *133*, 1–20. doi: 10.1130/b35739.1

Fernandes, V. M., Roberts, G. G., White, N., & Whittaker, A. C. (2019). Continental-Scale Landscape Evolution: A History of North American Topography. *Journal of Geophysical Research: Earth Surface*, *124*, 1–34. doi: 10.1029/2018jf004979

Fichtner, A., Kennett, B. L. N., Igel, H., & Bunge, H.-P. (2009). Full seismic waveform tomography for upper-mantle structure in the Australasian region using adjoint methods. *Geophysical Journal International*, *179*(3), 1703–1725. doi: 10.1111/j.1365-246X.2009.04368.x

Fichtner, A., Trampert, J., Cupillard, P., Saygin, E., Taymaz, T., Capdeville, Y., & Villaseñor, A. (2013). Multiscale full waveform inversion. *Geophysical Journal International*, *194*, 534–556. doi: 10.1093/gji/ggt118

Fichtner, A., & Villaseñor, A. (2015). Crust and upper mantle of the western Mediterranean - Constraints from full-waveform inversion. *Earth and Planetary Science Letters*, *428*, 52–62. doi: 10.1016/j.epsl.2015.07.038

Flament, N. (2018). Present-day dynamic topography and lower-mantle structure from palaeogeographically constrained mantle flow models. *Geophysical Journal International*, *216*(3), 2158–2182. doi: 10.1093/gji/ggy526

Flament, N. (2019). Present-day dynamic topography and lower-mantle structure from palaeogeographically constrained mantle flow models. *Geophysical Journal International*, *216*(3), 2158–2182. doi: 10.1093/gji/ggy526

Flament, N., Gurnis, M., & Muller, R. D. (2013). A review of observations and models of dynamic topography. *Lithosphere*, *5*(2), 189–210. doi: 10.1130/L245.1

Flament, N., Gurnis, M., Müller, R. D., Bower, D. J., & Husson, L. (2015). Influence of subduction history on South American topography. *Earth and Planetary Science Letters*, *430*, 9–18. doi: 10.1016/j.epsl.2015.08.006

Foley, S. F., & Fischer, T. P. (2017). An essential role for continental rifts and lithosphere in the deep carbon cycle. *Nature Geoscience*, *10*(12), 897–902. doi: 10.1038/s41561-017-0002-7

Forte, A. M. (2007). Constraints on Seismic Models from Other Disciplines - Implications for Mantle Dynamics and Composition. In B. Romanowicz & A. Dziewonski (Eds.), *Seismology and the structure of the earth* (pp. 805–858). Elsevier B.V. doi: 10.1016/B978-044452748-6.00027-4

Forte, A. M., & Peltier, R. (1991). Viscous Flow Models of Global Geophysical Observables 1. Forward Problems. *Journal of Geophysical Research*, *96*(B12), 20131–20159. doi: 10.1029/91JB01709

Forte, A. M., & Peltier, W. R. (1994). The Kinematics and Dynamics of Poloidal-Toroidal Coupling in Mantle Flow: The Importance of Surface Plates and Lateral Viscosity Variations. *Advances in Geophysics*, *36*, 1–119. doi: 10.1016/S0065-2687(08)60537-3

French, S. W., & Romanowicz, B. (2015). Broad plumes rooted at the base of the Earth's mantle beneath major hotspots. *Nature*, *525*(7567), 95–99. doi: 10.1038/nature14876

Galloway, W. E., Whiteaker, T. L., & Ganey-Curry, P. (2011). History of Cenozoic North American drainage basin evolution, sediment yield, and accumulation in the Gulf of Mexico basin. *Geosphere*, *7*(4), 938–973. doi:

10.1130/GES00647.1

Gantmacher, F. R. (1959). *The Theory of Matrices*. New York: Chelsea Publishing Company.

Ghelichkhan, S., Bunge, H.-P., & Oeser, J. (2021). Global mantle flow retrodictions for the early Cenozoic using an adjoint method: Evolving dynamic topographies, deep mantle structures, flow trajectories and sublithospheric stresses. *Geophysical Journal International*, *226*(2), 1432–1460. doi: 10.1093/gji/ggab108

Ghosh, A., Becker, T. W., & Zhong, S. J. (2010). Effects of lateral viscosity variations on the geoid. *Geophysical Research Letters*, *37*(1), 2–7. doi: 10.1029/2009GL040426

Ghosh, A., & Holt, W. E. (2012). Plate Motions and Stresses from Global Dynamic Models. *Science*, *335*(6070), 838–843. doi: 10.1126/science.1214209

Glišović, P., & Forte, A. M. (2016). A new back-and-forth iterative method for time-reversed convection modeling: Implications for the Cenozoic evolution of 3-D structure and dynamics of the mantle. *Journal of Geophysical Research: Solid Earth*, *121*(6), 4067–4084. doi: 10.1002/2016JB012841

Gunnell, Y., & Burke, K. (2008). The African Erosion Surface: A Continental-Scale Synthesis of Geomorphology, Tectonics, and Environmental Change over the Past 180 Million Years. *Memoir of the Geological Society of America*, *201*, 1–66. doi: 10.1130/2008.1201

Gurnis, M., Mitrovica, J. X., Ritsema, J., & Van Heijst, H.-J. (2000). Constraining mantle density structure using geological evidence of surface uplift rates: The case of the African Superplume. *Geochemistry, Geophysics, Geosystems*, *1*(7), 1–35. doi: 10.1029/1999GC000035

Hager, B. H. (1984). Subducted Slabs and the Geoid: Constraints on Mantle Rheology and Flow. *Journal of Geophysical Research*, *89*(B7), 6003–6015.

Hager, B. H., & Clayton, R. W. (1989). Constraints on the Structure of Mantle Convection Using Seismic Observations, Flow Models, and the Geoid. In W. R. Peltier (Ed.), *Mantle convection: Plate tectonics and global dynamics* (pp. 657–763). New York: Gordon and Breach Science Publishers.

Hager, B. H., Clayton, R. W., Richards, M. A., Comer, R. P., & Dziewonski, A. M. (1985). Lower mantle heterogeneity, dynamic topography and the geoid. *Nature*, *313*, 541–545. doi: 10.1038/314752a0

Hager, B. H., & O'Connell, R. J. (1979). Kinematic Models of Large-Scale Flow in the Earth's Mantle. *Journal of Geophysical Research*, *84*(B3), 1031–1048.

Hager, B. H., & O'Connell, R. J. (1981). A Simple Global Model of Plate Dynamics and Mantle Convection. *Journal of Geophysical Research*, *86*(B6), 4843–4867. doi: 10.1029/JB086iB06p04843

Hazzard, J. A. N., Richards, F. D., Goes, S. D. B., & Roberts, G. G. (2022). Probabilistic Assessment of Antarctic Thermomechanical Structure: Impacts on Ice Sheet Stability. *EarthArXiv*. doi: 10.31223/X5C35R

Heister, T., Dannberg, J., Gassmöller, R., & Bangerth, W. (2017). High accuracy mantle convection simulation through modern numerical methods – II: realistic models and problems. *Geophysical Journal International*, *210*(2), 833–851. doi: 10.1093/gji/ggx195

Hoggard, M. J., Austermann, J., Randel, C., & Stephenson, S. (2021). Observational Estimates of Dynamic Topography Through Space and Time. In *Mantle convection and surface expressions* (pp. 371–411). AGU. doi: 10.1002/9781119528609.ch15

Hoggard, M. J., White, N., & Al-Attar, D. (2016). Global dynamic topography observations reveal limited influence of large-scale mantle flow. *Nature Geoscience*, *9*(May), 1–8. doi: 10.1038/ngeo2709

Holdt, M. C., White, N. J., Stephenson, S. N., & Conway-Jones, B. W. (2022). Densely Sampled Global Dynamic Topographic Observations and Their Signifi-

cance. *Journal of Geophysical Research: Solid Earth*, *127*, 1–32.

Jeans, J. H. (1923). The Propagation of Earthquake Waves. *Proceedings of the Royal Society of London A*, *102*(718), 554–574.

Kaula, W. M. (1963). Determination of the Earth's Gravitational Field. *Reviews of Geophysics*, *1*(4), 507–551.

Kramer, S. C., Davies, D. R., & Wilson, C. R. (2021). Analytical solutions for mantle flow in cylindrical and spherical shells. *Geoscientific Model Development*, *14*(4), 1899–1919. doi: 10.5194/gmd-14-1899-2021

Lambeck, K., Smither, C., & Johnston, P. (1998). Sea-level change, glacial rebound and mantle viscosity for northern Europe. *Geophysical Journal International*, *134*, 102–144. doi: 10.1046/j.1365-246X.1998.00541.x

Lau, H. C. P., Mitrovica, J. X., Davis, J. L., Tromp, J., Yang, H.-Y., & Al-Attar, D. (2017). Tidal tomography constrains Earth's deep-mantle buoyancy. *Nature*, *551*(7680), 321–326. doi: 10.1038/nature24452

Lees, M. E., Rudge, J. F., & McKenzie, D. (2020). Gravity, topography, and melt generation rates from simple 3D models of mantle convection. *Geochemistry, Geophysics, Geosystems*, *21*, 1–29. doi: 10.1029/2019gc008809

Lekić, V., & Fischer, K. M. (2014). Contrasting lithospheric signatures across the western United States revealed by Sp receiver functions. *Earth and Planetary Science Letters*, *402*, 90–98. doi: 10.1016/j.epsl.2013.11.026

Liu, L., & Gurnis, M. (2008). Simultaneous inversion of mantle properties and initial conditions using an adjoint of mantle convection. *Journal of Geophysical Research: Solid Earth*, *113*(B8), 1–17. doi: 10.1029/2008jb005594

Lu, C., Forte, A. M., Simmons, N. A., Grand, S. P., Kajan, M. N., Lai, H., & Garnero, E. J. (2020). The Sensitivity of Joint Inversions of Seismic and Geodynamic Data to Mantle Viscosity. *Geochemistry, Geophysics, Geosystems*, *21*(4), 1–29. doi: 10.1029/2019gc008648

McKenzie, D. (1977). Surface deformation, gravity anomalies and convection. *Geophysical Journal of the Royal Astronomical Society*, *48*, 211–238. doi: 10.1111/j.1365-246X.1977.tb01297.x

Merdith, A. S., Williams, S. E., Collins, A. S., Tetley, M. G., Mulder, J. A., Blades, M. L., ... Müller, R. D. (2021). Extending full-plate tectonic models into deep time: Linking the Neoproterozoic and the Phanerozoic. *Earth-Science Reviews*, *214*(103477), 1–44. doi: 10.1016/j.earscirev.2020.103477

Mitrovica, J. X., & Forte, A. M. (2004). A new inference of mantle viscosity based upon joint inversion of convection and glacial isostatic adjustment data. *Earth and Planetary Science Letters*, *225*(1-2), 177–189. doi: 10.1016/j.epsl.2004.06.005

Molnar, P., England, P. C., & Jones, C. H. (2015). Mantle dynamics, isostasy, and the support of high terrain. *Journal of Geophysical Research: Solid Earth*, *120*(3), 1932–1957. doi: 10.1002/2014JB011724

Morris, M., Fernandes, V. M., & Roberts, G. G. (2020). Extricating dynamic topography from subsidence patterns: Examples from Eastern North America's passive margin. *Earth and Planetary Science Letters*, *530*(115840), 1–13. doi: 10.1016/j.epsl.2019.115840

Moucha, R., & Forte, A. M. (2011). Changes in African topography driven by mantle convection: supplementary information. *Nature Geoscience*, *4*(10), 707–712. doi: 10.1038/ngeo1235

Moucha, R., Forte, A. M., Mitrovica, J. X., & Daradich, A. (2007). Lateral variations in mantle rheology: Implications for convection related surface observables and inferred viscosity models. *Geophysical Journal International*, *169*(1), 113–135. doi: 10.1111/j.1365-246X.2006.03225.x

Moucha, R., Forte, A. M., Mitrovica, J. X., Rowley, D. B., Quéré, S., Simmons, N. A., & Grand, S. P. (2008). Dynamic topography and long-term sea-level variations: There is no such thing as a stable continental platform. *Earth and*

Planetary Science Letters, *271*(1-4), 101–108. doi: 10.1016/j.epsl.2008.03.056

O'Connell, R. J. (1971). Pleistocene Glaciation and the Viscosity of the Lower Mantle. *Geophysical Journal of the Royal Astronomical Society*, *23*(3), 299–327. doi: 10.1111/j.1365-246X.1971.tb01823.x

O'Malley, C. P. B., White, N. J., Stephenson, S. N., & Roberts, G. G. (2021). Large-Scale Tectonic Forcing of the African Landscape. *Journal of Geophysical Research: Earth Surface*, *126*, 1–37. doi: 10.1029/2021jf006345

Panasyuk, S. V., Hager, B. H., & Forte, A. M. (1996). Understanding the effects of mantle compressibility on geoid kernels. *Geophysical Journal International*, *124*(1), 121–133. doi: 10.1111/j.1365-246X.1996.tb06357.x

Panton, J., Davies, J. H., & Myhill, R. (2023). The Stability of Dense Oceanic Crust Near the Core-Mantle Boundary. *Journal of Geophysical Research: Solid Earth*, *128*, 1–21. doi: 10.1029/2022JB025610

Parsons, B., & Daly, S. (1983). The relationship between surface topography, gravity anomalies and temperature structure of convection. *Journal of Geophysical Research*, *88*(B2), 1129–1144. doi: 10.1029/JB088iB02p01129

Pekeris, C. L. (1935). Thermal Convection in the Interior of the Earth. *Geophysical Supplements to the Monthly Notices of the Royal Astronomical Society*, *3*(8), 343–367.

Priestley, K., & McKenzie, D. (2013). The relationship between shear wave velocity, temperature, attenuation and viscosity in the shallow part of the mantle. *Earth and Planetary Science Letters*, *381*, 78–91. doi: 10.1016/j.epsl.2013.08.022

Ribe, N. M. (2007). Analytical Approaches to Mantle Dynamics. *Treatise on Geophysics*, *7*, 167–226. doi: 10.1016/B978-044452748-6.00117-6

Ricard, Y. (2007). Physics of Mantle Convection. *Treatise on Geophysics*, *7*, 31–88.

Ricard, Y. (2015). Physics of Mantle Convection. In G. Schubert (Ed.), *Treatise on geophysics* (pp. 23–71). doi: 10.1016/B978-044452748-6.00115-2

Richards, F. D., Hoggard, M. J., Ghelichkhan, S., Koelemeijer, P., & Lau, H. C. P. (2021). Geodynamic, geodetic, and seismic constraints favour deflated and dense-cored LLVPs. *EarthArXiv*, 1–20. doi: 10.31223/X55601

Richards, F. D., Hoggard, M. J., Ghelichkhan, S., Koelemeijer, P., & Lau, H. C. P. (2023). Geodynamic, geodetic, and seismic constraints favour deflated and dense-cored LLVPs. *Earth and Planetary Science Letters*, *602*(117964), 1–13. doi: 10.1016/j.epsl.2022.117964

Richards, F. D., Hoggard, M. J., White, N., & Ghelichkhan, S. (2020). Quantifying the relationship between short-wavelength dynamic topography and thermomechanical structure of the upper mantle using calibrated parameterization of anelasticity. *Journal of Geophysical Research: Solid Earth*, *125*, 1–36. doi: 10.1029/2019JB019062

Richards, M. A., & Hager, B. H. (1984). Geoid Anomalies in a Dynamic Earth. *Journal of Geophysical Research*, *89*(B7), 5987–6002. doi: 10.1029/JB089iB07p05987

Salles, T., Flament, N., & Müller, D. (2017, jan). Influence of mantle flow on the drainage of eastern Australia since the Jurassic Period. *Geochemistry, Geophysics, Geosystems*, *18*(1), 280–305. doi: 10.1002/2016GC006617

Spasojevic, S., & Gurnis, M. (2012). Sea level and vertical motion of continents from dynamic earth models since the Late Cretaceous. *AAPG Bulletin*, *96*(11), 2037–2064. doi: 10.1306/03261211121

Stanley, J. R., Braun, J., Baby, G., Guillocheau, F., Robin, C., Flowers, R. M., ... Beucher, R. (2021). Constraining Plateau Uplift in Southern Africa by Combining Thermochronology, Sediment Flux, Topography, and Landscape Evolution Modeling. *Journal of Geophysical Research: Solid Earth*, *126*, 1–34. doi: 10.1029/2020JB021243

Steinberger, B. (2007). Effects of latent heat release at phase boundaries on flow in

the Earth's mantle, phase boundary topography and dynamic topography at the Earth's surface. *Physics of the Earth and Planetary Interiors*, *164*(1-2), 2–20. doi: 10.1016/j.pepi.2007.04.021

Steinberger, B. (2016). Topography caused by mantle density variations: Observation-based estimates and models derived from tomography and lithosphere thickness. *Geophysical Journal International*, *205*(1), 604–621. doi: 10.1093/gji/ggw040

Steinberger, B., & Antretter, M. (2006). Conduit diameter and buoyant rising speed of mantle plumes: Implications for the motion of hot spots and shape of plume conduits. *Geochemistry, Geophysics, Geosystems*, *7*(11), 1–25. doi: 10.1029/2006GC001409

Steinberger, B., & Calderwood, A. R. (2006). Models of large-scale viscous flow in the Earth's mantle with constraints from mineral physics and surface observations. *Geophysical Journal International*, *167*(3), 1461–1481. doi: 10.1111/j.1365-246X.2006.03131.x

Steinberger, B., Nelson, P. L., Grand, S. P., & Wang, W. (2019). Yellowstone plume conduit tilt caused by large-scale mantle flow. *Geochemistry, Geophysics, Geosystems*, *20*, 5896–5912. doi: 10.1029/2019gc008490

Stephenson, S. N., White, N. J., Carter, A., Seward, D., Ball, P. W., & Klöcking, M. (2021). Cenozoic Dynamic Topography of Madagascar. *Geochemistry, Geophysics, Geosystems*, *22*, 1–38. doi: 10.1029/2020gc009624

Tackley, P. J., Stevenson, D. J., Glatzmaier, G. A., & Schubert, G. (1993). Effects of an endothermic phase transition at 670 km depth on spherical mantle convection. *Nature*, *361*, 699–704. doi: 10.1038/361699a0

Thoraval, C., Machete, P., & Cazenave, A. (1994). Influence of mantle compressibility and ocean warping on dynamical models of the geoid. *Geophysical Journal International*, *117*, 566–573. doi: 10.1111/j.1365-246X.1994.tb03954.x

Thoraval, C., & Richards, M. A. (1997). The geoid constraint in global geodynamics: Viscosity structure, mantle heterogeneity models and boundary conditions. *Geophysical Journal International*, *131*, 1–8. doi: 10.1111/j.1365-246X.1997.tb00591.x

Topographic asymmetry of the south atlantic from global models of mantle flow and lithospheric stretching. (2014). *Earth and Planetary Science Letters*, *387*, 107-119. doi: 10.1016/j.epsl.2013.11.017

Turcotte, D. L., & Schubert, G. (2002). *Geodynamics* (Second Edi ed.). Cambridge University Press.

Wang, Y., Liu, L., & Zhou, Q. (2022). Topography and gravity reveal denser cratonic lithospheric mantle than previously thought. *Geophysical Research Letters*, *49*(1). doi: https://doi.org/10.1029/2021GL096844

Wieczorek, M. A., & Meschede, M. (2018). SHTools: Tools for Working with Spherical Harmonics. *Geochemistry, Geophysics, Geosystems*, *19*, 1–19. doi: 10.1029/2018GC007529

Zhong, S., Gurnis, M., & Hulbert, G. (1993). Accurate determination of surface normal stress in viscous flow from a consistent boundary flux method. *Physics of the Earth and Planetary Interiors*, *78*, 1–8. doi: 10.1016/0031-9201(93)90078-N

Zhong, S., McNamara, A., Tan, E., Moresi, L., & Gurnis, M. (2008). A benchmark study on mantle convection in a 3-D spherical shell using CitcomS. *Geochemistry, Geophysics, Geosystems*, *9*(10), 1–32. doi: 10.1029/2008GC002048

Zhong, S., Zuber, M. T., Moresi, L., & Gurnis, M. (2000). Role of temperature-dependent viscosity and surface plates in spherical shell models of mantle convection. *Journal of Geophysical Research*, *105*(B5), 11063–11082.

Zhou, Q., & Liu, L. (2019). Topographic evolution of the western United States since the early Miocene. *Earth and Planetary Science Letters*, *514*, 1–12. doi: 10.1016/j.epsl.2019.02.029

1157 Zhou, Q., Liu, L., & Hu, J. (2018). Western US volcanism due to intruding oceanic
1158 mantle driven by ancient Farallon slabs. *Nature Geoscience*, *11*, 70–76. doi: 10
1159 .1038/s41561-017-0035-y

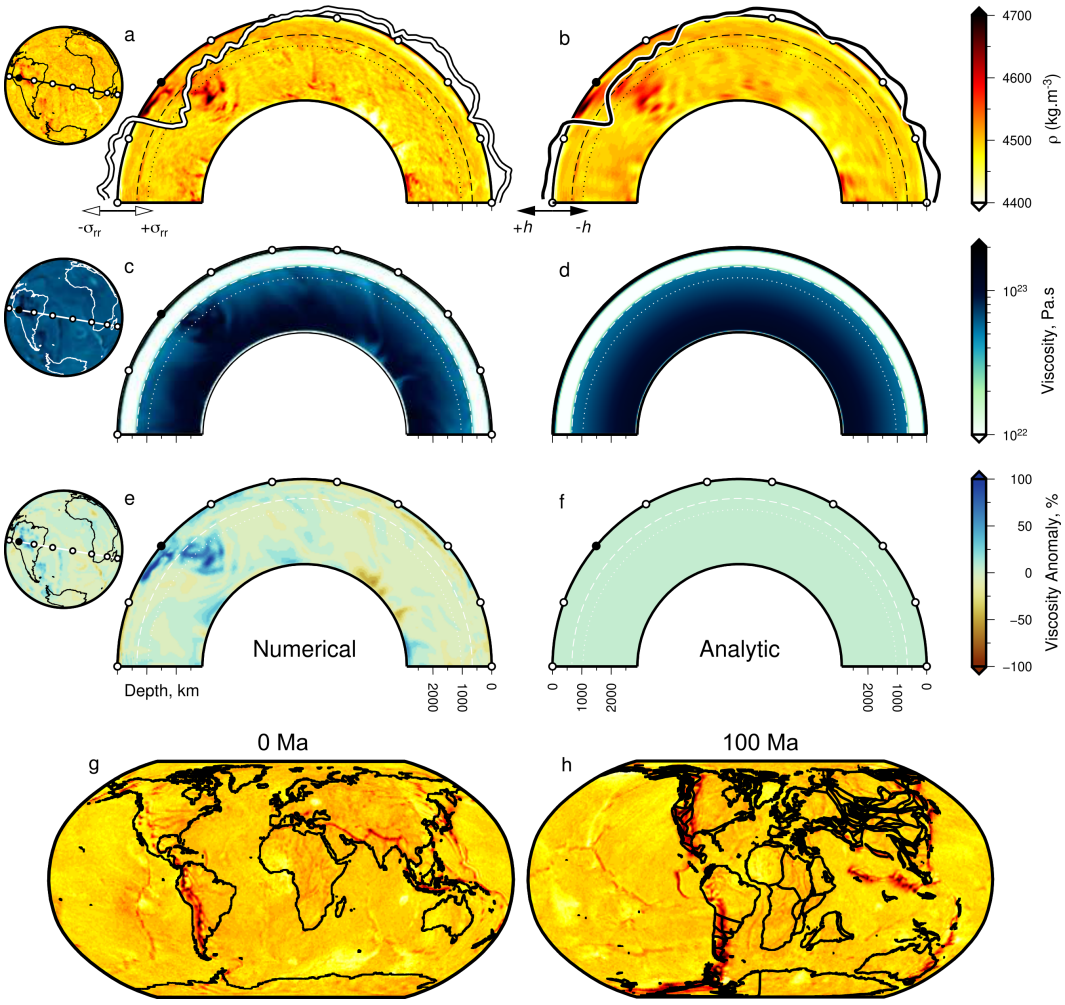

Figure 1. Examples of mantle densities and viscosity used to calculate stresses and surface deflections numerically and analytically. (a) Great-circle slice (180°) through full-resolution, present-day, density ρ, predicted by numeric model TERRA with temperature dependent viscosity (Model 11a; see Table 1 and body text); see globe to left for location. White circles = 20° intervals; filled black circle indicates orientation of cross section; dashed line = 660 km depth contour; dotted line = 1038 km depth contour, at which depth ρ is plotted on globe; white-black curve = numeric prediction of surface normal stress σ_{rr} from Model 11a. (b) As (a) but slice is through spherical harmonic expansion of density structure, to maximum degree $l = 50$ ($\lambda \approx 792$ km; Model 11b); black-white curve = surface deflection h, calculated using (analytic) propagator matrix approach (Model 12). (c) As (a) but for slice through full-resolution viscosity structure of numeric model. (d) As (c) but for mean (radial) viscosity structure, used along with the density structure shown in (b) to generate analytic solution for surface deflection shown by black-white curve atop (b). (e–f) As (c–d) but viscosity is expressed as a percentage anomaly with respect to the layer (radial) mean. (g–h) Predicted densities at 270 km depth at 0 and 100 Ma from numeric model with viscosity independent of temperature (Model 1a). Extended results are shown in Figure S1. Plate motions and paleo-coastlines are from Merdith et al. (2021).

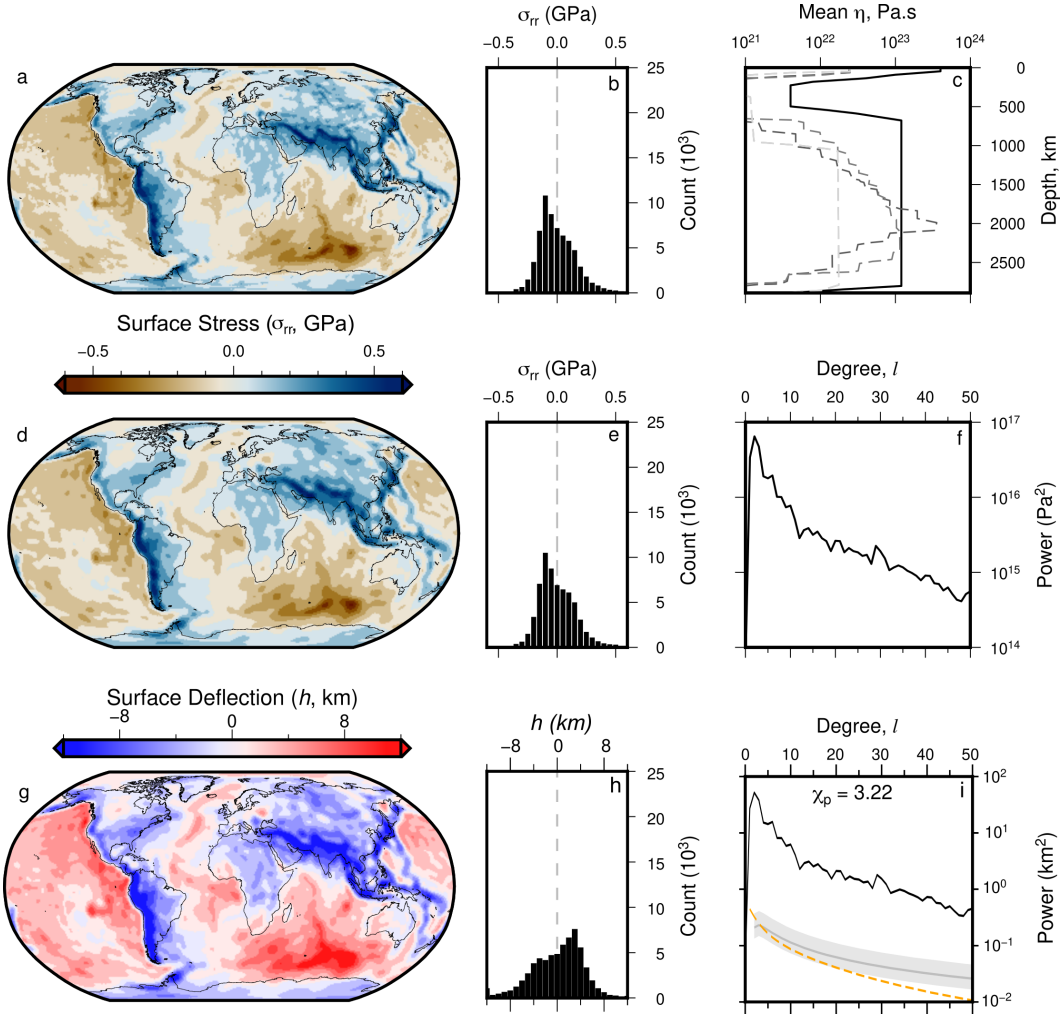

Figure 2. Surface stresses and deflections from numeric simulation of mantle convection with spherical harmonic expansion up to degree 50. (a) Predicted present-day surface radial stress, σ_{rr} (Model 1a). (b) Histogram of values shown in (a). (c) Black line = radial viscosity structure used to drive Model 1a and thus produce grid shown in panel (a). Gray dashed lines = alternative viscosity profiles of (from darkest to lightest) Mitrovica and Forte (2004), Steinberger and Calderwood (2006), and μ_1, μ_2 from Ghelichkhan et al. (2021). (d) Model 1b: Spherical harmonic fit to Model 1a (panel a) up to maximum degree $l = 50$ (minimum wavelength $\lambda \approx 792$ km). (e) Histogram of values shown in panel (d). (f) Power spectrum—total power per degree—of stress field shown in panel (d). (g) Spherical harmonic fit to surface deflections (Model 1b; up to degree $l = 50$). (h) Histogram of values shown in panel (g). (i) Black curve = power spectrum of calculated water-loaded surface deflections (panel g); gray line and band = expected dynamic topography from Kaula's rule using admittance $Z = 12 \pm 3$ mGal km^{-1} (Kaula, 1963). Orange dashed line = expected power spectrum for water-loaded residual topography (from Holdt et al., 2022) via analytic solution of special case of Equation 15. χ_p = root-mean-squared difference between calculated (black) and independent (orange & grey) surface deflection power (see Equation 20). All histograms are weighted by latitude to correct to equal-area. Figure S2 shows extended results including air-loaded deflections.

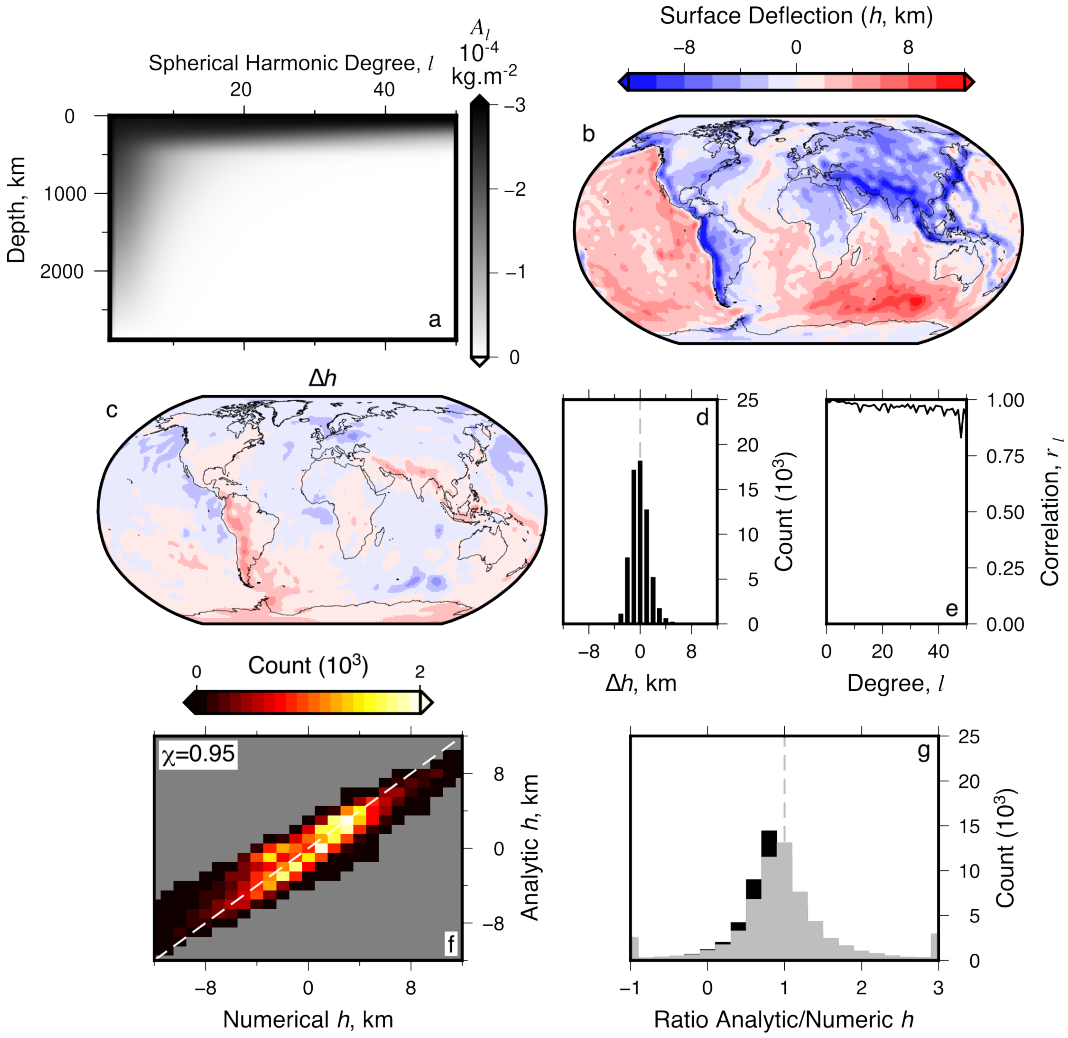

Figure 3. Comparisons of numeric (Model 1b) and analytic (Model 2) estimation of surface deflections from models with identical parameterization. (a) Surface deflection sensitivity kernel A_l as a function of spherical harmonic degree, l, and depth (Model 2). (b) Propagator matrix (analytic) solution for water-loaded surface deflection calculated using sensitivity kernel shown in panel (a). Figure S3 shows extended results including power spectra and air-loaded deflections. (c) Difference, Δh, of surface deflections in Models 1b and 2. (d) Histogram of difference values shown in (c). (e) Spectral correlation coefficient, r_l, between Models 1b and 2; Equation 8. (f) Comparison of predicted surface deflections; χ = root-mean-squared difference between predictions (Equation 7); gray dashed line = 1:1 ratio. (g) Black bars = histogram of ratios between analytic:numeric solutions for surface deflection as in (f). Gray dashed line = 1 (i.e., identical values). Gray bars = as black bars, but for propagator matrix solution amplitudes scaled up by optimal factor to fit numeric solution (=10%). All histograms are weighted by latitude to correct to equal-area.

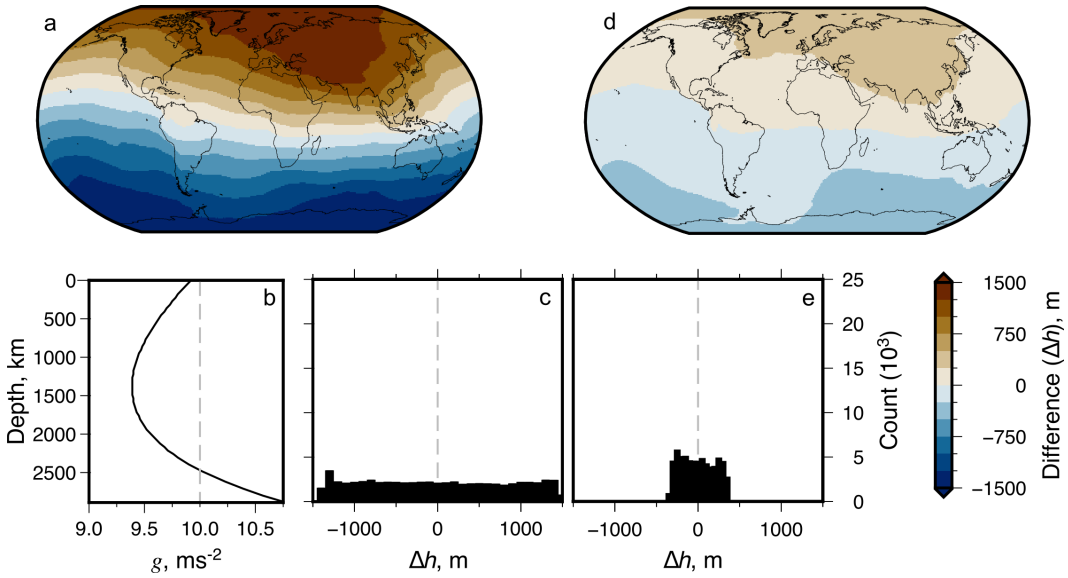

Figure 4. Impact of self-gravitation (a–c) and gravitational potential of deflected surfaces (d–e) on surface deflections calculated analytically. In these tests surface deflections from models with different gravity parameterizations are compared to predictions from Model 2. (a) Difference between water-loaded surface deflections calculated using the propagator matrix technique incorporating self-gravitation (Model 3; black curve in panel b) and g = 10 m s^{-2} (dashed line in panel b; Model 2). (c) Histogram of values in panel (a). (d–e) Differences in surface deflection from models with (Model 4) and without (Model 2) stress perturbations induced by gravitational potential of the deflected surface. All histograms are weighted by latitude to correct to equal-area, they show the full extent of the results. Figures S4–S5 show extended results including maps of calculated surface deflections.

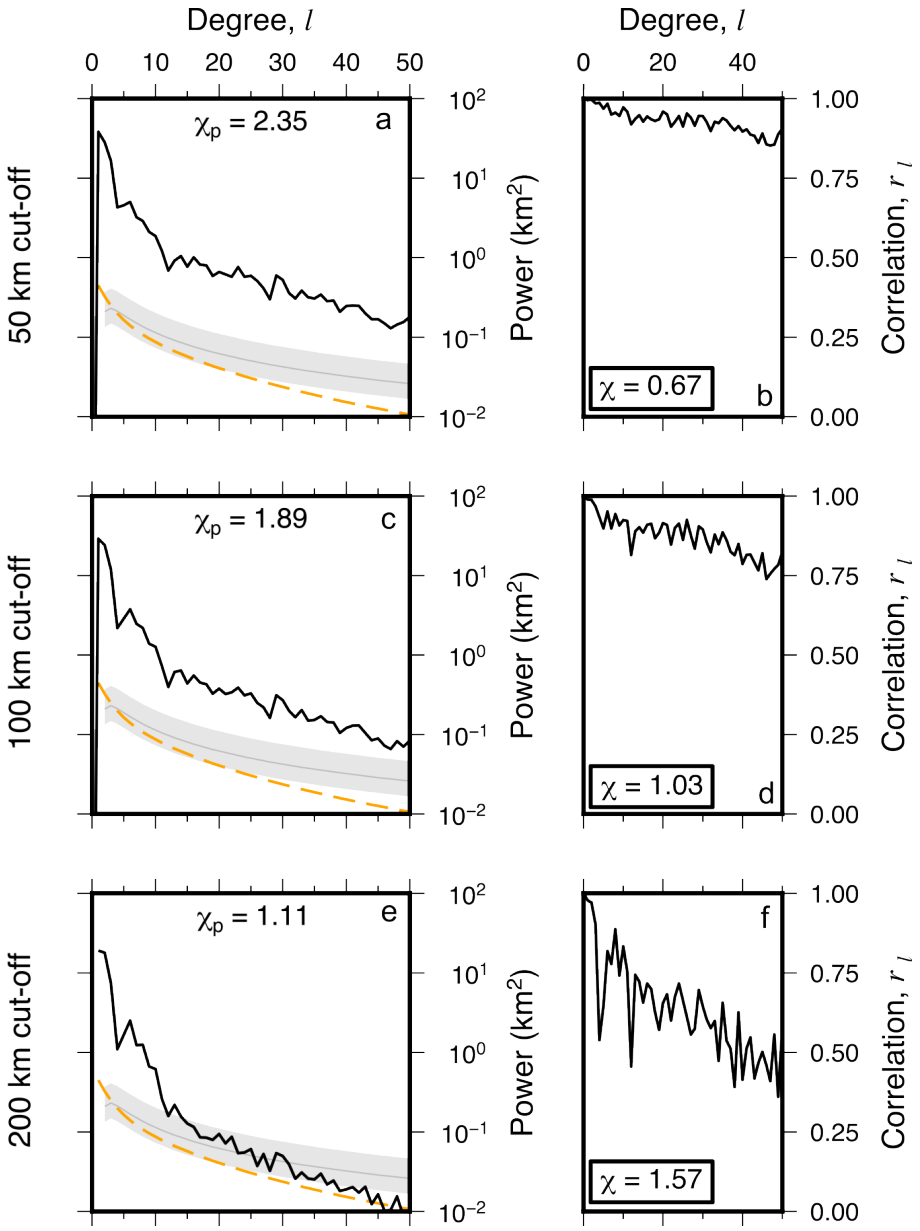

Figure 5. Effect of removing shallow structure on surface deflections calculated analytically. Surface deflections in models with shallow structure removed are compared to those predicted by Model 2. (a) Black line = Power spectra of predicted water-loaded surface deflection from propagator matrix solution for Model 2 (Figure 3b), but with effect of upper 50 km of density anomaly structure ignored in calculation (Model 5). Gray line and band = expected dynamic topography from Kaula's rule using admittance $Z = 12 \pm 3$ mGal km^{-1} (Kaula, 1963). Orange dashed line = expected power spectrum for water-loaded residual topography from Holdt et al. (2022), via analytic solution of special case of Equation 15. χ_p = root-mean-squared difference between calculated (black) and independent (orange & grey) surface deflection power (see Equation 20). (b) Spectral correlation coefficient, r_l, of surface deflections in Models 5 and 2 (see Equation 19). Inset χ = root-mean-squared difference in surface deflections of Models 5 and 2 (see Equation 18). (c–d) and (e–f) as (a–b) but for depth cut-offs of 100 (Model 6) and 200 km (Model 7), respectively. Figure S7 show extended results including maps of calculated surface deflections and differences with Model 2.

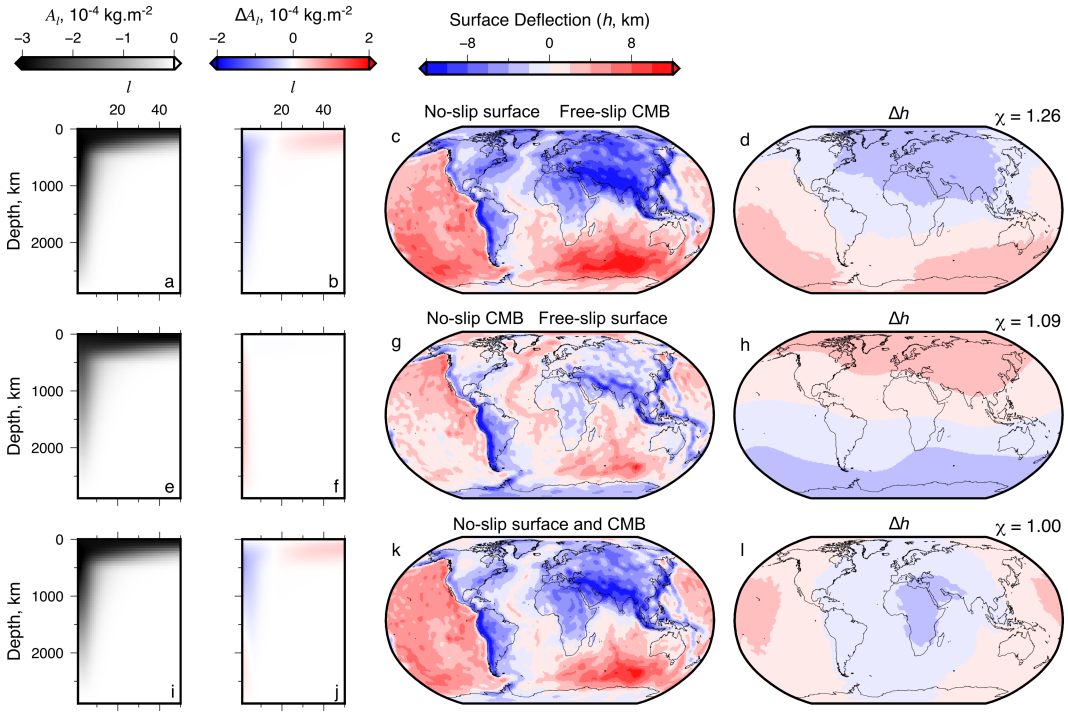

Figure 6. Impact of free- and no-slip surface and core-mantle boundary boundary conditions on surface deflections. This figure shows comparisons of surface deflections from models with different assumed boundary conditions and Model 2. (a) Water-loaded surface deflection sensitivity kernel A_l, for Model 8, which has a no-slip surface boundary condition, but otherwise is parameterised the same as Model 2. (b) Sensitivity kernel of Model 8 minus sensitivity kernel of Model 2. Note, positive difference implies reduced sensitivity compared to Model 2, and vice versa, since A_l is negative. (c) Predicted water-loaded surface deflection for Model 8. (d) Difference between surface deflection predictions for Model 8 and Model 2. (e–h) as (a–d) but for Model 9: free-slip surface boundary, no-slip CMB. (i–l) as (a–d) but for Model 10: no-slip surface and CMB boundaries.

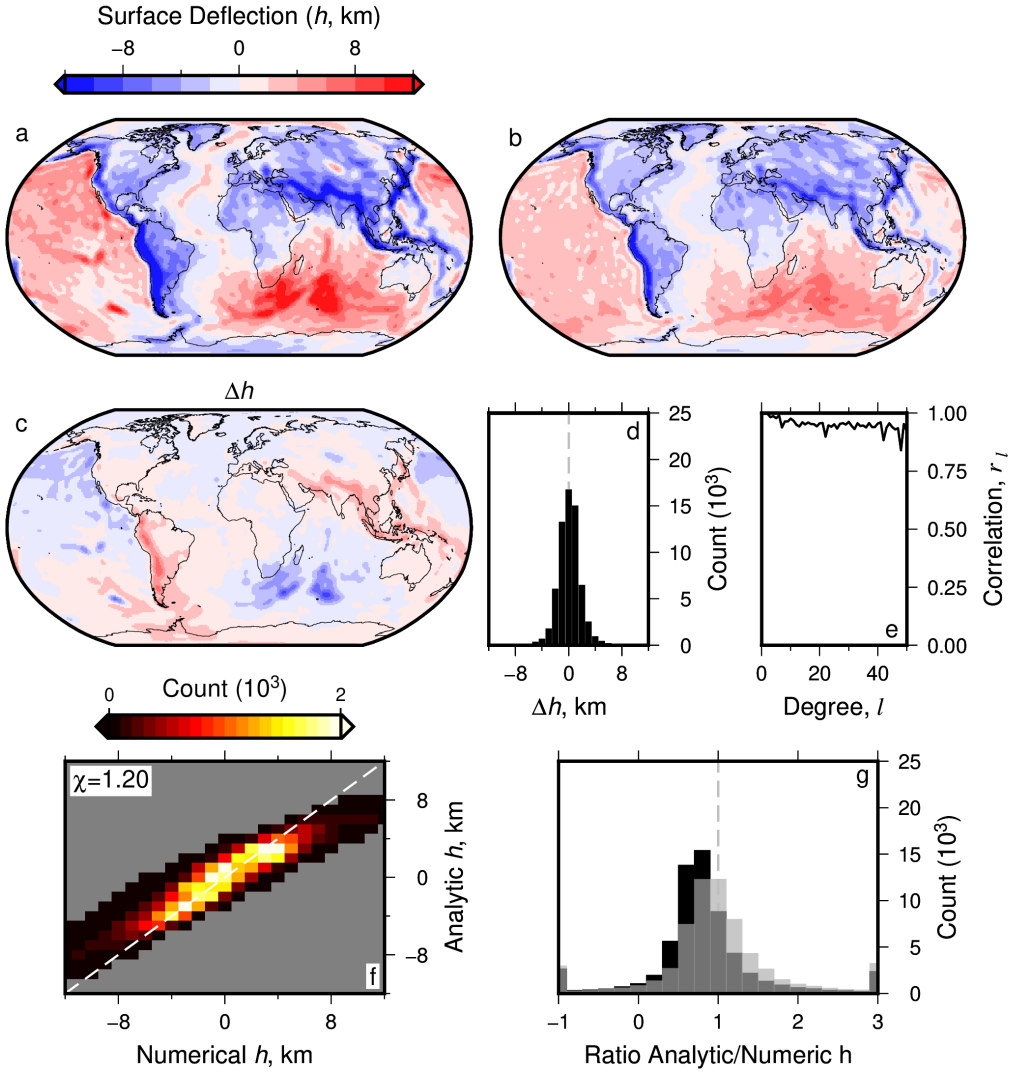

Figure 7. Comparison of surface deflections calculated numerically (Model 11b) and analytically (Model 12) using results from simulation with temperature dependent viscosity. (a) Model 11b: Spherical harmonic expansion of predicted present-day water-loaded surface deflection converted from stress output from numeric model TERRA (Model 11a), to maximum degree $l = 50$. (b) Model 12: As (a) but for prediction made using propagator matrix method. (c) Difference, Δh, between Models 11b and 12 (panels a and b). (d) Histogram of difference values shown in (c), weighted by latitude to correct to equal-area. (e) Spectral correlation coefficient, r_l, between predictions shown in panels (a) and (b); Equation 8. (f) Numeric (Model 11b) versus analytic (Model 12) predictions of surface deflection; χ = root-mean-squared difference between predictions, Equation 7; gray dashed line = 1:1 ratio. (g) Histogram of ratios between analytic:numeric solutions for surface deflection as in (f), weighted by latitude. Gray dashed line = 1 (i.e., identical values). Gray bars = as black bars, but for propagator matrix solution amplitudes scaled up by optimal factor to fit numeric solution (24%).

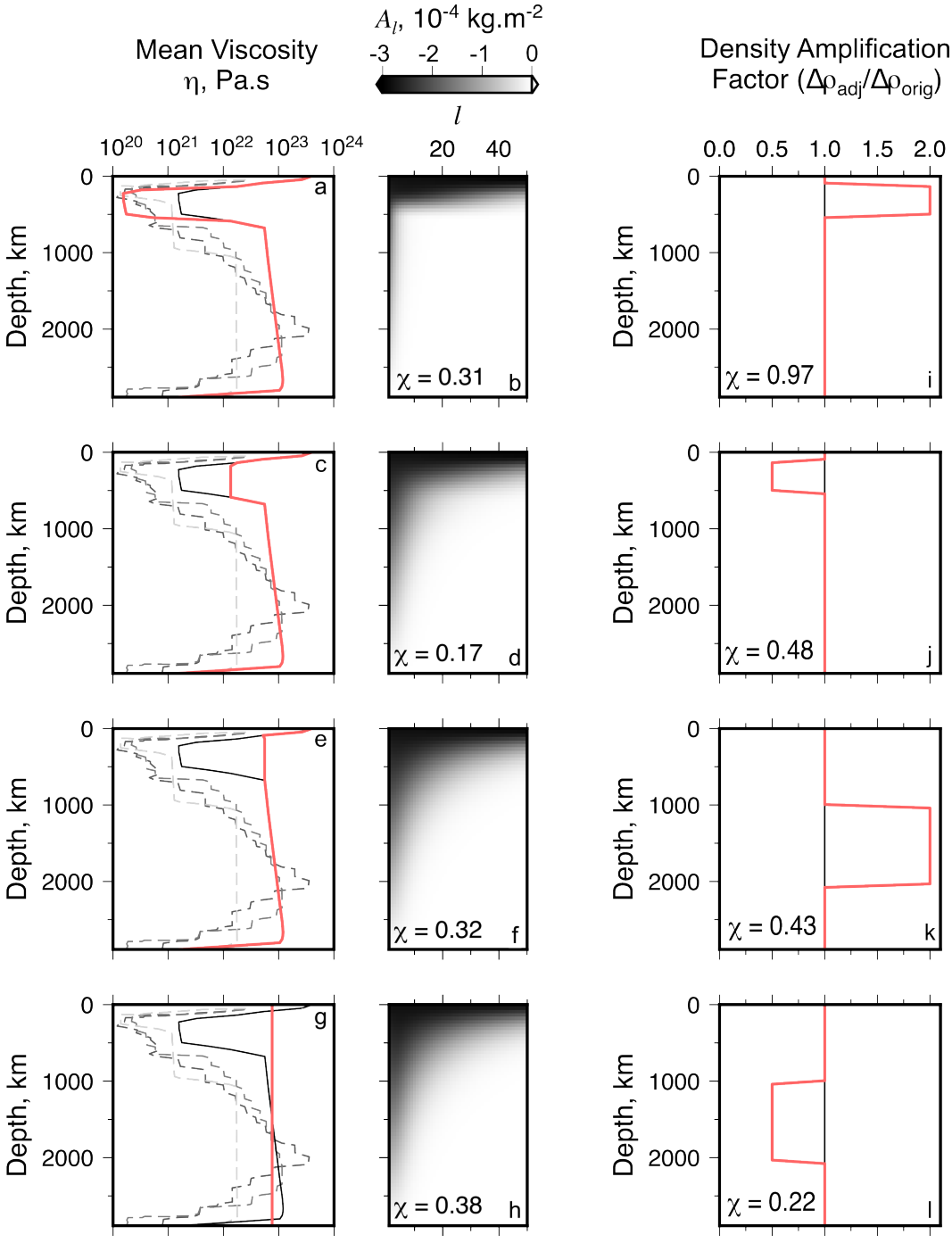
Mean Viscosity
η, Pa.s
A_l, 10^{-4} kg.m^{-2}
-3 -2 -1 0
l
Density Amplification
Factor ($\Delta\rho_{adj}/\Delta\rho_{orig}$)
10^{20} 10^{21} 10^{22} 10^{23} 10^{24}
20 40
0.0 0.5 1.0 1.5 2.0
Depth, km
0
1000
2000
a
b
χ = 0.31
c
d
χ = 0.17
e
f
χ = 0.32
g
h
χ = 0.38
i
χ = 0.97
j
χ = 0.48
k
χ = 0.43
l
χ = 0.22

Figure 8. Sensitivity of calculated analytic surface deflection to adjusted radial viscosity (a–h) and density anomalies (i–l). This figure shows comparisons of surface deflections calculated in models with modified viscosity and density to the results from Model 12 (see Table 1). (a) Black curve = unadjusted prediction of present-day radial mean viscosity from Model 11; red line = adjusted radial profile with viscosity decreased by a factor of 10 between depths of $\sim$ 300–500 km (Model 13); gray dashed lines = viscosity profiles used in other studies (see Figure 2). (b) Sensitivity kernel for the viscosity profile indicated by the red curve in panel a. Value of root-mean-squared difference, χ, between calculated surface deflections for unadjusted and adjusted viscosity is stated (see Equation 7). (c–h) Results from testing alternative radial viscosity (Models 14–16). Figure S13 shows extended results including maps of surface deflections and their differences. (i-l) Density anomalies (red line) adjusted by directly scaling spherical harmonic coefficients ($l > 0$) up or down by a factor of 2 (Models 17 & 19: panels e & g) or $\frac{1}{2}$ (Models 18 & 20: f & h). Viscosity structure applied in each case is same as that used to generate Figure 7b. Sensitivity kernels for surface deflections are not shown since they are invariant with respect to density anomalies, $\Delta\rho$, depending only on viscosity structure. Figure S14 shows extended results including maps of surface deflections and their differences.

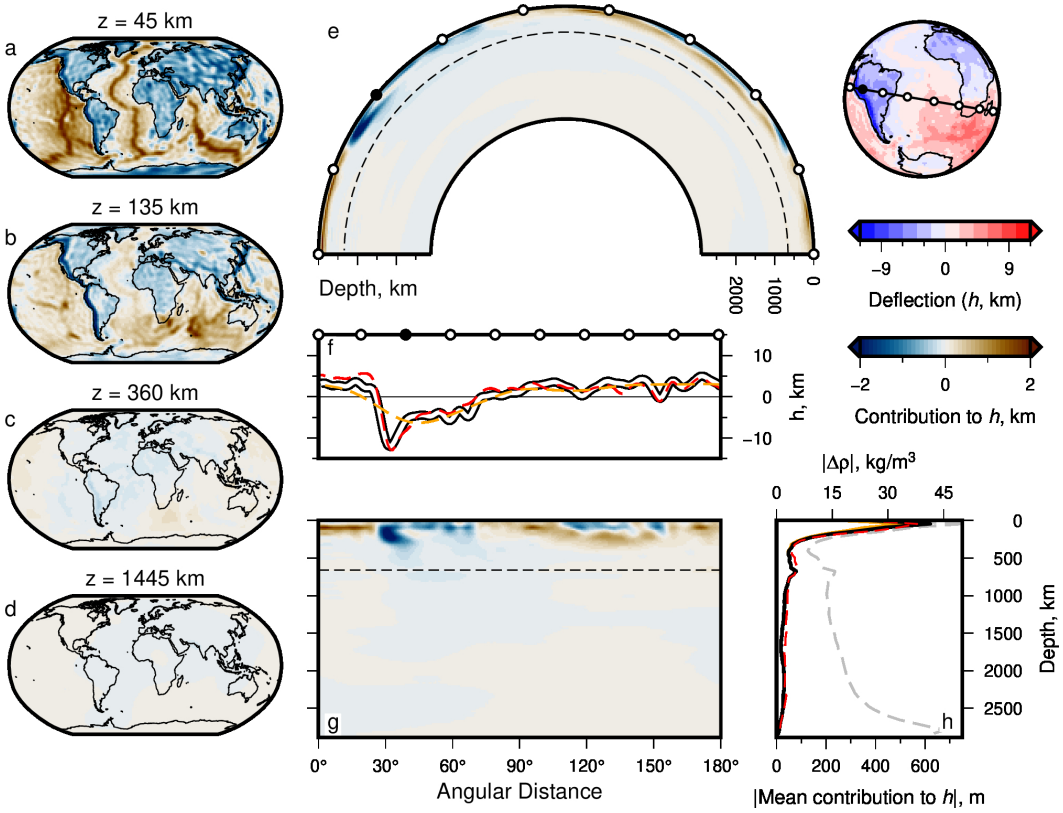

Figure 9. Effective density; contributions from density anomalies to surface deflection. (a–d) Maps of net contribution to present-day water-loaded surface deflection calculated using propagator matrix approach (Model 12; see body text for details). Depth slices at 45, 135, 360 and 1445 km depth incorporating all spherical harmonic degrees l and orders m, up to l = 50. (e) Great-circle slice (180°) showing contributions to surface deflection; globe to right shows transect location and calculated surface deflection (Model 12). White circles = 20° intervals; note filled black circle for orientation; dashed line = 660 km depth contour. (f) White-black curve = total surface deflection along transect shown atop globe in panel (e); abscissa aligned with panel g; orange dashed line = same but for maximum l = 10 (see Supporting Information Figure S18); red dashed curve = surface deflection from Model 2. (g) Cartesian version of panel (e); ordinate aligned with panel (h). (h) Grey dashed curve = mean absolute value of density anomalies in Model 12—see top axis for values. Black curve = global mean amplitude (modulus) of contribution from density structure in Model 12 to total surface deflection h, across all l and m; orange line = same but for maximum l = 10; red dashed line = results for Model 2 (see Section 6.3). See Figures S15–S19 for extended results, demonstrating sensitivity of surface deflections to maximum spherical harmonic degree.

Reconciling Surface Deflections From Simulations of Global Mantle Convection

Conor P. B. O'Malley[1,2], Gareth G. Roberts[1], James Panton[3], Fred D. Richards[1], J. Huw Davies[3], Victoria M. Fernandes[1,4], Sia Ghelichkhan[5]

[1]Department of Earth Science & Engineering, Imperial College London, London SW7 2BP, UK
[2]now at Cathie Group, 2-4 Hanover Square, Newcastle upon Tyne, NE1 3NP, UK
[3]School of Earth & Environmental Sciences, University of Cardiff, Park Place, Cardiff CF10 3AT, UK
[4]now at Section 4.6 Geomorphology, GFZ Potsdam, Telegrafenberg, 14473 Potsdam, Germany
[5]Research School of Earth Sciences, Australian National University, 142 Mills Road, Acton, ACT 0200, Australia

Key Points:

- Numeric and analytic predictions of surface deflections from mantle convection simulations are compared.
- Impact of gravitation, excising shallow structure, boundary conditions, and different viscosity and density distributions are quantified.
- Calculated effective contributions to surface deflection emphasize dominance of upper mantle structure.

Corresponding author: Conor O'Malley; Gareth Roberts, c_omalley1@msn.com; gareth.roberts@imperial.ac.uk

Abstract

The modern state of the mantle and its evolution on geological timescales is of widespread importance for the Earth sciences. For instance, it is generally agreed that mantle flow is manifest in topographic and drainage network evolution, glacio-eustasy and in the distribution of sediments. There now exists a variety of theoretical approaches to predict histories of mantle convection and its impact on surface deflections. A general goal is to make use of observed deflections to identify Earth-like simulations and constrain the history of mantle convection. Several important insights into the role of radial and non-radial viscosity variations, gravitation, and the importance of shallow structure already exist. Here we seek to bring those insights into a single framework to elucidate the relative importance of popular modelling choices on predicted instantaneous vertical surface deflections. We start by comparing results from numeric and analytic approaches to solving the equations of motion that are ostensibly parameterised to be as-similar-as-possible. Resultant deflections can vary by $\sim$10%, increasing to $\sim$ 25% when viscosity is temperature-dependent. Including self-gravitation and gravitational potential of the deflected surface are relatively small sources of discrepancy. However, spherical harmonic correlations between model predictions decrease dramatically with the excision of shallow structure to increasing depths, and when radial viscosity structure is modified. The results emphasise sensitivity of instantaneous surface deflections to density and viscosity anomalies in the upper mantle. They reinforce the view that a detailed understanding of lithospheric structure is crucial for relating mantle convective history to observations of vertical motions at Earth's surface.

Plain Language Summary

Flow of rock within Earth's interior plays a crucial role in evolving the planet. It moves heat and chemicals from deep depths to the surface, for instance. It also moves the lithosphere—the Earth's outer rocky shell—which in turn impacts processes including mountain building, sea-level change, formation of volcanoes, river network evolution, and natural resource distribution. Consequently, we wish to understand the present state, and history, of flowing rock within Earth's interior. Observations exist to address this problem, and mathematics and computing tools can also be used to predict histories of flow and their impact on Earth's surface. We explore how assumptions incorporated into such numeric models can affect calculations of the vertical deflection of Earth's surface. Predictions from different models are compared, with a view to identifying crucial modelling components. Surface sensitivity to deep flow is assessed, demonstrating how surface observations can enlighten flow histories.

1 Introduction

Mantle convection plays a crucial role in Earth's evolution (e.g., Hager & Clayton, 1989; Parsons & Daly, 1983; Pekeris, 1935). It is well understood, for instance, that flow in the mantle is fundamental in the transfer of heat and chemicals from the deep Earth to the surface, in driving horizontal and vertical lithospheric motions (thus tectonic processes), and in magnetism via interactions with the core (e.g., Biggin et al., 2012; Davies et al., 2023; Foley & Fischer, 2017; Hoggard et al., 2016; Holdt et al., 2022; Pekeris, 1935). In turn, many processes operating at or close to Earth's surface are impacted, including glacio-eustasy, magmatism, climate, sediment routing, natural resource distribution, drainage network evolution, and development of biodiversity (e.g., Bahadori et al., 2022; Ball et al., 2021; Braun, 2010; Chang & Liu, 2021; Hazzard et al., 2022; O'Malley et al., 2021; Salles et al., 2017; Stanley et al., 2021). Clearly, understanding the physical and chemical evolution of the mantle has broad implications. An important goal is to determine contributions to surface processes from the modern mantle and its history during, say, the last 100 million years.

Residual oceanic age-depth measurements, potential field data, seismic tomographic models and melting histories of young mafic rocks are providing increasingly coherent observational insights into the modern and recent state of the mantle (e.g., Ball et al., 2022; Davies et al., 2023; Fichtner et al., 2009, 2013; Fichtner & Villaseñor, 2015; French & Romanowicz, 2015; Hoggard et al., 2016; Holdt et al., 2022; Kaula, 1963; Lekić & Fischer, 2014; Priestley & McKenzie, 2013; F. D. Richards et al., 2021). Stratigraphic and geomorphic observations as well as magmatic histories provide clues about the history of mantle convection on geologic timescales (e.g., Al-Hajri et al., 2009; Czarnota et al., 2013; Flament et al., 2015; Fernandes et al., 2019; Fernandes & Roberts, 2021; Galloway et al., 2011; Gunnell & Burke, 2008; Gurnis et al., 2000; Hoggard et al., 2021; Lambeck et al., 1998; Morris et al., 2020; O'Malley et al., 2021; Stanley et al., 2021). Despite these advances, observations providing information about the history of mantle convection are sparse in places, especially within continental interiors and back in time (see e.g., Hoggard et al., 2021). Moreover, disentangling contributions from crustal, lithospheric and sub-lithospheric processes to surface deflections remains challenging and controversial (see e.g. Hoggard et al., 2021; Wang et al., 2022).

Theoretical approaches that retrodict histories of mantle convection can, in principle, be used to fill in spatio-temporal gaps in the observational record and disentangle contributions to surface observables from different geologic processes (e.g., Baumgardner, 1985; Bunge & Baumgardner, 1995; Davies et al., 2013; Flament et al., 2015; Ghelichkhan et al., 2021; Hager et al., 1985; Moucha & Forte, 2011; Steinberger & Antretter, 2006). Increasingly realistic geodynamic simulations incorporating, for instance, plate motions, gravitation and deflection of gravitational potential fields, complex rheologies, viscosity laws that can include temperature, pressure, composition, grain size and strain rate dependence, and assimilation of seismic tomographic information into flow solutions, result in a diverse array of retrodicted flow histories. Mineralogical phase changes, compressibility, different surface and core-mantle boundary slip conditions (e.g., no-slip, free-slip), chemical and thermal buoyancy, and plate motion constraints on mantle structure can also generate diverse predictions of mantle convection and resultant surface deflections (e.g., Baumgardner, 1985; Bunge et al., 2002, 2003; Corrieu et al., 1995; Crameri et al., 2012; Dannberg et al., 2017; "Topographic asymmetry of the South Atlantic from global models of mantle flow and lithospheric stretching", 2014; Forte, 2007; Ghosh & Holt, 2012; Glišović & Forte, 2016; Hager & Clayton, 1989; Heister et al., 2017; Liu & Gurnis, 2008; Panasyuk et al., 1996; Ribe, 2007; Ricard, 2007; Tackley et al., 1993; Zhong et al., 2008; Zhou et al., 2018). Aside from the fundamental choice of governing equations and parameterizations underpinning simulations, mathematical and computational approaches to solve the equations of motion generate different predictions of surface deflections. These approaches sit within two broad families: numeric simulations (e.g., ASPECT, CitcomS, TERRA; Bangerth et al., 2023; Baumgardner, 1985; Zhong et al., 2000), and propagator-matrix-based, quasi-analytic techniques, that can be solved in two or three dimensions, and importantly for our purposes, spherically and spectrally (e.g., Colli et al., 2016; Hager & O'Connell, 1979; Parsons & Daly, 1983).

A challenge then is to establish whether observed surface deflections can be used to discriminate between theoretical predictions of mantle convection, and, in turn, identify models that generate realistic and testable retrodictions. In this study we are principally concerned with establishing similarities and sensitivities of predicted instantaneous vertical surface deflections. We focus on vertical motions for two reasons. First, inventories of measurements of uplift and subsidence—on timescales of mantle convection—now exist for most continents and could be compared to predictions from global simulations in future work (e.g. Fernandes & Roberts, 2021, and references therein). Secondly, many geodynamic simulations incorporate horizontal motions of the lithosphere, which limits their use as a comparator.

From an observational perspective, it would be useful to establish rules-of-thumb that quantify sensitivity of surface deflections to choices made when predicting them. Many such rules are already well known from analytic and numeric solutions of the equations of motion (e.g., Colli et al., 2016; Hager & O'Connell, 1979; Holdt et al., 2022; Lees et al., 2020; Parsons & Daly, 1983). For instance, a suite of benchmark studies exist that compare predictions from numeric mantle convection simulations with analytic solutions (see e.g., Bauer et al., 2019; Kramer et al., 2021; Zhong et al., 2008, and references therein). Those papers tend to focus on establishing the fidelity of numeric models. In contrast, our goals are to, first, understand how calculated deflections are impacted by the choice of methodology used to solve the equations of motion and, secondly, to establish sensitivities to popular assumptions incorporated into simulations. We want to know the extent to which an improved fit between predictions and observations reflects a more Earth-like density and viscosity structure versus modelling choices. Our thesis is that performing all tests in a self-consistent framework, as we do in this study, provides a straightforward way to collate insights into the sensitivities of predicted surface deflections and to simplify the comparison of predictions from different suites of models.

1.1 Our Approach and Paper Structure

We start by exploring the consequences of solving the equations of motion numerically, using the TERRA software, and analytically, using Ghelichkhan et al. (2021)'s propagator matrix algorithms (see Figure 1 & Supporting Information). We make use of the flexibility of numeric approaches by incorporating a variety of assumptions and parameterizations that are not amenable to analytic attack (e.g., temperature-dependent viscosity). All numeric simulations presented in this paper were driven by the plate motion history of Merdith et al. (2021, see Figures 1g–h and S1). The models have a resolution of 60 km at their surface (see Supporting Information for details of model setup and execution). We note that they do not directly assimilate information about the mantle from tomographic models. Ensuring that numeric simulations are accurate and stable means that computational burden is often considerable and hence systematic exploration of parameter space remains challenging. In contrast, analytic approaches can yield calculated surface deflections that are (mathematically) accurate, whilst including features such as radial gravitation, with much less computational cost. Consequently, we make use of propagator matrix techniques to explore parameter space, examine benchmarks, and reproduce results. We establish the sensitivity of solutions to different parameterizations and approaches to solving the equations of motion.

There are at least two important considerations when solving the equations of motion analytically. First, solutions are only known to exist in the spherical harmonic domain for fluid bodies with radial viscosity (i.e., no lateral variability in viscosity). Second, generating solutions in the spherical harmonic domain places practical limits on spatial resolution of solutions. Consider that the number of spherical harmonic coefficients per degree $= 2l+1$, where l is degree, so for a given maximum degree L, there are $(L+1)^2$ coefficients in total. For instance, when $L = 50$ there are $2,601$ coefficients for each model. Consider also that spatial resolution increases approximately with the reciprocal of l (see Section 2.2). Incorporating full resolution output from the numeric models (60 km at the surface) would require $L \approx 880$, with $776,161$ coefficients, which is computationally cumbersome. Furthermore, observational constraints on mantle-related surface deflection are unlikely to be finer than the flexural wavelength of the overlying lithosphere, $l \approx 50$ (e.g., Holdt et al., 2022). With these limitations in mind, we compared surface deflections predicted using different approaches at the same resolution up to $l = 50$ (see Supporting Information and Section 2.3).

Most of the tests in this paper compare surface deflections calculated using the entirety of the model domains (i.e., from CMB to the surface). This approach simplifies like-for-like comparisons of model predictions and comparisons to increasingly complex

scenarios. However, amplitudes of calculated deflections will of course not reflect estimated amplitudes of dynamic topography. This approach purposefully avoids isolating passive or plate-driven surface deflections and sub-plate support from numeric simulations or analytic solutions. Since the central focus of this work is merely on quantifying contrasts that arise from choices made when simulating mantle convection, we wish to avoid incorporating additional modifications where possible. In subsequent tests we examine the consequences of simply removing shallow structure, a widely used approach for estimating dynamic support from simulations (see e.g., Flament et al., 2013; Flament, 2018; Wang et al., 2022).

With this framework in place we generate, compare and contrast predicted surface deflections. The first suite of tests are purposefully simple, e.g., incompressible, constant gravitational acceleration (no self-gravitation or radial variation in gravitation) and have radial viscosity independent of temperature. Results are compared to estimates of sub-plate support from oceanic age-depth residuals with a view to quantifying corrections necessary to convert predicted instantaneous surface deflections into estimates of sub-plate support. We then systematically examine the impact of incorporating radial variations in gravitational acceleration, contribution to flow from deflection of the gravitational potential field, removal of shallow density structure, choice of surface and CMB slip conditions, inclusion of temperature-dependent viscosity, and amplification or reduction of viscosity and density anomalies in the upper and lower mantle (Section 4; Tables 1–2). A closed-loop modelling strategy is explored in which predicted surface deflections from these relatively complex models are compared to results from simpler reference models. Finally, a methodology for assessing effective contributions to surface topography from mantle anomalies is presented.

2 Numeric and Analytic Calculations of Surface Deflection

The Supporting Information document summarises the formulations of Stokes' equations that are solved, model parameter values used and the numeric approach to calculating mantle convection using the TERRA finite-element software. Here, we move straight to explaining how those simulations are used to calculate radial stresses, σ_{rr}, thence vertical deflections, h, at Earth's surface (Figure 1). A methodology for representing model predictions in the spherical harmonic domain is then described. We then examine analytic solutions obtained using propagator matrix techniques.

2.1 Deflections calculated using radial stresses from numeric simulation

Following Parsons and Daly (1983), surface deformation is estimated from numeric simulations of mantle convection by making use of the requirement that normal stress is continuous across the upper boundary of the solid Earth (see also McKenzie, 1977; Ricard, 2015). In other words, radial stresses generated by the solid Earth are required to be balanced by stresses generated by the overlying (oceanic or atmospheric) fluid. There are three contributions to normal stress at this boundary from the mantle: hydrostatic stress that would exist even in the absence of convection, dynamic stress arising from convection, and viscous stress which opposes fluid motion (see Equations 2–6 in Supporting Information). To satisfy the continuity condition, these stresses must be balanced by those generated by the water (or air) column atop this boundary. If the pressure from the overlying column is hydrostatic, the resultant condition is

$$\rho_w g_s h = \rho_m g_s h + \sigma_{rr}, \tag{1}$$

where σ_{rr} incorporates deviatoric viscous stresses generated by mantle convection and dynamic pressure ($\sigma_{rr} = \tau_{rr} - p$), obtained by solving Equation 2 in Supporting Information. In practice, since values for this term are obtained by subtracting radial litho-

static stress from the total stress, values of σ_{rr} integrate to zero globally. g_s is gravitational acceleration at Earth's surface, ρ_m is the mean density for the surficial layer, and ρ_w is the density of the overlying fluid (see Table S1). Note that we do not impose additional oceanic plate cooling, e.g., due to hydrothermal circulation at ridges. Cooling and subsequent subsidence, as well as passive return flow at ridges, arise naturally from solution of the governing equations laid out in Section 2 of Supporting Information.

Surface deflection arising in response to predicted convective flow, h, is approximated by rearranging Equation 1,

$$h \approx -\frac{\sigma_{rr}}{(\rho_m - \rho_w)g_s}. \tag{2}$$

Deflections are estimated from radial stresses at times of interest (e.g., the present-day) by re-running one time-step of the TERRA model. During that time-step, a free-slip boundary condition, for which analytic approximations for surface deflection exist, is imposed instead of the plate-slip condition prescribed during the main model run routine (see Section 2.3; Ricard, 2015). The numeric models themselves apply a quasi-rigid condition at the surface, whereby flow is driven by estimates of real plate velocities (from Merdith et al., 2021), and so the surface layers behave as a series of rigid, laterally mobile plates rather than a single rigid shell. We assess the accuracy of modifying boundary conditions in this way by converting calculated deflections into the spherical harmonic domain and comparing them to predictions generated using the analytic propagator matrix approach. The consistent boundary flux (CBF) method provides an alternative means to accurately calculate normal stresses (Zhong et al., 1993). Previous benchmarking with TERRA has shown mean errors of a few percent or less for surface deflection predictions at low harmonic degrees, $l \leq 16$ (Davies et al., 2013).

2.2 Surface Deflections Calculated in the Spherical Harmonic Domain

Transforming stress, or surface deflections, calculated using numeric approaches into the frequency domain provides straightforward means of comparing results to analytic solutions and of quantifying spectral power, i.e., the magnitude of contribution to the total signal from different wavelengths. Since the models that we investigate are global in scope, we do so using spherical harmonics. The methodology for calculating spherical harmonics and the definition of power adopted in this study are included as Supporting Information. Figure 2 shows an example of surface stresses calculated using the TERRA code, their spherical harmonic representation, calculated surface deflections in the spherical harmonic domain, and associated statistics and power spectra.

Using the total power per degree convention, Hoggard et al. (2016) derived a rule-of-thumb for estimating the power spectrum of dynamic topography (see their Supporting Information), P_l^{DT}, using Kaula (1963)'s approximation for the long-wavelength gravity field of Earth as a function of l:

$$P_l^{DT} \approx \left(\frac{GM}{ZR^2}\right)^2 \left(\frac{2}{l} - \frac{3}{l^2} + \frac{1}{l^4}\right), \tag{3}$$

where G is the gravitational constant, $M = 5.97 \times 10^{24}$ kg is the mass of the Earth, $R \approx 6370$ km is Earth's radius. The value of low-degree admittance, Z, between gravity and topography varies as a function of viscosity, as well as the depth and wavelength of internal density anomalies (Colli et al., 2016). Hoggard et al. (2016) found that assuming an average value of $Z = 12$ mGal km^{-1} provides a reasonable approximation of observed residual topographic trends, thus we make use of that value in the remainder of the paper. Finally, it is useful to note that Jeans (1923) related spherical harmonic degree to wavelength λ, which at Earth's surface can be approximated via $\lambda \approx 2\pi R/\sqrt{l(l+1)}$.

2.3 Surface Deflections Calculated Analytically

The second methodology used to calculate surface deflection in response to mantle convection is the analytic propagator matrix technique (e.g., Craig & McKenzie, 1987; Gantmacher, 1959; Ghelichkhan et al., 2021; Parsons & Daly, 1983; M. A. Richards & Hager, 1984). The approach we take stems from the work of Hager and O'Connell (1981) who used Green's functions to solve the equations of motion in the spherical harmonic domain. Those solutions are used to generate sensitivity kernels that straightforwardly relate, for example, density or temperature anomalies in the mantle to surface deflections. The kernels are generated in the frequency domain, and constructed such that surface deflection sensitivity to mantle (e.g., density) anomalies is calculated as a function of depth (or radius) and wavenumber. A global spherical harmonic implementation introduced by Hager et al. (1985) has been extended to include compressibility, the effect of warping of the gravitational potential by subsurface density distributions, and radial gravity variations calculated using radial mean density values (Corrieu et al., 1995; Forte & Peltier, 1991; Hager & O'Connell, 1981; M. A. Richards & Hager, 1984; Thoraval et al., 1994).

In this study, following Ghelichkhan et al. (2021), surface deflection for each spherical harmonic coefficient, h_{lm}, is calculated in the spectral domain such that

$$h_{lm} = \frac{1}{(\rho_m - \rho_w)} \int_{R_{\mathrm{CMB}}}^{R} A_l \delta\rho_{lm}(r) \cdot \mathrm{d}r. \tag{4}$$

Products of the sensitivity kernel, A_l, and density anomalies, $\delta\rho_{lm}$, of spherical harmonic degree, l, and order, m, are integrated with respect to radius, r, between the core-mantle boundary and Earth's surface radii, R_{CMB} and R, respectively. The sensitivity kernel is given by

$$A_l = -\left(\frac{\eta_0}{R g_R}\right)\left(u_1 + \frac{\rho_w}{\rho_0} u_3\right), \tag{5}$$

where $u_n(r)$ represents a set of poloidal variables, which are posed for solution of the set of simultaneous equations by matrix manipulation, such that

$$u(r) = \begin{bmatrix} y_1\eta_0 & y_2\eta_0\Lambda & (y_3 + \bar{\rho}(r)y_5)r & y_4 r\Lambda & y_5 r\rho_0\Lambda & y_6 r^2\rho_0 \end{bmatrix}^T, \tag{6}$$

where $\Lambda = \sqrt{l(l+1)}$, and y_1 to y_6 represent the spherical harmonic coefficients of radial velocity v_r, lateral velocity $v_{\theta,\phi}$, radial stress σ_{rr}, lateral stress $\sigma_{r\theta,\phi}$, gravitational potential V, and gravitational potential gradient $\partial V/\partial r$, respectively (Hager & Clayton, 1989; Panasyuk et al., 1996). $\bar{\rho}$ is the layer mean ($l = 0$) density. The kernel A_l includes both u_1 and u_3, two terms in the matrix solution to the governing equations that affect surface topography by directly exerting stress on the surface boundary (u_1), and by changing the gravitational potential at the surface (u_3). The functional forms of calculated sensitivity kernels depend on chosen radial viscosity profiles and boundary conditions (e.g., free-slip or no-slip; Parsons & Daly, 1983).

3 Spatial and Spectral Comparison of Model Predictions

To quantify impacts of modelling assumptions and approaches used to solve the equations of motion we compare calculated surface deflections using the following metrics.

3.1 Euclidean Comparisons of Amplitudes

First, we calculate root-mean-squared difference, χ, between predicted surface deflections in the spatial domain,

$$\chi = \sqrt{\frac{1}{N}\sum_{n=1}^{N} w_\phi \left(h_n^a - h_n^b\right)^2}, \tag{7}$$

where h_n^a and h_n^b are predicted surface deflections from the two models being compared. N = number of points in the 1×1° gridded maps being compared (e.g., Figure 3b; N = 65341). The prefactor w_ϕ is proportional to $\cos\phi$, where ϕ is latitude, and is included to correct biases in cell size with latitude; mean $w_\phi = 1$. This metric is closely associated with the mean vertical distance (L^2-norm distance) between predicted and reference surfaces, i.e., $\Delta\bar{h} = 1/N \sum_{n=1}^{N} w_\phi |h_n^a - h_n^b|$. These metrics are sensitive to differences in amplitudes and locations of surface deflections.

3.2 Spectral Correlation Coefficients

Second, we use pyshtools v4.10 to compute correlation coefficients, r_l, between predicted surface deflections in the spectral domain (Wieczorek & Meschede, 2018). Correlation coefficients as a function of degree l, adapted from Forte (2007), are calculated such that

$$r_l = \frac{\sum f_1^* f_2}{\sqrt{\sum f_1^* f_1}\sqrt{\sum f_2^* f_2}}, \quad \text{where} \quad \sum = \sum_{m=-l}^{+l}, \tag{8}$$

f_1 and f_2 are the spherical harmonic coefficients of the two fields (i.e., surface deflections) being compared, which vary as a function of order, m, and l; $f = f_l^m$. * indicates complex conjugation (see also Becker & Boschi, 2002; O'Connell, 1971). This metric is sensitive to the difference between predicted and reference surface deflection signals in the frequency domain, but not to their amplitudes. To summarize spectral similarity between models concisely, we later refer to the mean value of r_l over every degree (0–50) as $\bar{r_l}$. We refer to the standard deviation of r_l across degrees as s_r.

3.3 Comparing Calculated Power Spectra

Lastly, to estimate closeness of fit between power spectra of surface deflections predicted in this study and independent estimates, we calculate

$$\chi_p = \sqrt{\frac{1}{L}\sum_{l=1}^{L}\left(\log_{10}P_l - \log_{10}P_l^K\right)^2} + \sqrt{\frac{1}{L}\sum_{l=1}^{L}\left(\log_{10}P_l - \log_{10}P_l^H\right)^2}, \tag{9}$$

where L = number of spherical harmonic degrees being compared ($L = 50$). P_l = power of predicted surface deflections generated in this study at degrees $1 \leq l \leq L$ (Equation 11 in Supporting Information). P_l^K = power of surface deflections estimated using Kaula's law (Equation 3). P_l^H = power of residual oceanic age-depth measurements from Holdt et al. (2022).

4 Model Parameterizations

The models examined in this paper are summarised in Table 1. In terms of assumptions tested there are two families of models, those with viscosity independent of tem-

Table 1. Summary of mantle convection simulations. Column labeled 'Method' indicates surface deflections calculated using either '*Numeric*' (i.e., from surface normal stresses calculated using TERRA) or '*Analytic*' (i.e., propagator matrix) approaches; '*Mixed*' indicates spherical harmonic fitting of surface stresses calculated using numeric code, enabling comparison with solutions to propagator matrix code. $\eta(r)$ indicates models with radial viscosity (e.g. independent of temperature; Models 1–10). $\eta(r,T)$ indicates models with temperature-dependent (therefore laterally varying) viscosity (Models 11–20); note that analytic Models 12–20 incorporate radial viscosity calculated using mean radial viscosity from Model 11a. †indicates with respect to Model 12. See Table 1, Section 4 and figures referred to in column 5 for details.

Model	Method	Viscosity	Parameterizations	Figures
1a	Numeric	$\eta(r)$	Full resolution numeric model	1g-h, 2a-c, S1-2
1b	Mixed	$\eta(r)$	Spherical harmonic fit to 1a	2d–i
2	Analytic	$\eta(r)$	Propagator matrix solutions	3, S3
3	Analytic	$\eta(r)$	Radial gravitation, $g(r)$	4a-c, S4
4	Analytic	$\eta(r)$	Gravitational potential terms	4d-e, S5
5	Analytic	$\eta(r)$	Removing upper 50 km of mantle	5a-b, S7a-d
6	Analytic	$\eta(r)$	Removing upper 100 km of mantle	5c-d, S7e-h
7	Analytic	$\eta(r)$	Removing upper 200 km of mantle	5e-f, S7i-l
8	Analytic	$\eta(r)$	No-slip surface, free CMB	6a-d
9	Analytic	$\eta(r)$	Free surface, no-slip CMB	6e-h
10	Analytic	$\eta(r)$	No-slip surface, no-slip CMB	6i-l
11a	Numeric	$\eta(r,T)$	Full resolution numeric model	S8-S10, S12a-c
11b	Mixed	$\eta(r,T)$	Spherical harmonic fit to 11a	7, S8-10, S12d-g
12	Analytic	$\eta(r)$	Mean radial $\eta(r,T)$ from Model 11a	7, S11, S12h-k
13	Analytic	$\eta(r)$	Decrease† radial upper mantle η	8a-b, S13a-d
14	Analytic	$\eta(r)$	Increase† radial upper mantle η	8c-d, S13e-h
15	Analytic	$\eta(r)$	Increase† radial upper mantle η	8e-f, S13i-l
16	Analytic	$\eta(r)$	Constant radial η	8g-h, S13m-p
17	Analytic	$\eta(r)$	Upper mantle densities $\times 2^{\dagger}$	8i, S14a-c
18	Analytic	$\eta(r)$	Upper mantle densities $\times 1/2^{\dagger}$	8j, S14d-f
19	Analytic	$\eta(r)$	Lower mantle densities $\times 2^{\dagger}$	8k, S14g-i
20	Analytic	$\eta(r)$	Lower mantle densities $\times 1/2^{\dagger}$	8l, S14j-l

perature (Models 1–10), and those with temperature-dependent viscosity (Models 11–20). We note that Models 12-20 incorporate mean radial viscosity from the numeric Model 11a in which viscosity depends on temperature. The two approaches used to solve the equations of motion are annotated 'Numeric' and 'Analytic' in Table 1, which refers to solutions from the TERRA and propagator matrix code, respectively. Viscosities and densities calculated using TERRA were used as input for the propagator matrix code and thus used to generate analytic estimates of surface deflection. Since analytic solutions are obtained by spherical harmonic expansion, surface deflections from TERRA were fit using spherical harmonics before predicted deflections were compared (annotated 'Mixed' in Table 1; Section 2.2). We compare predicted deflections that arise from flow across entire model domains, i.e., from the CMB to the surface. Parameterizations of these models and resultant surface deflections are discussed in the following sections, with summary statistics given in Table 2.

346

347 ## 4.1 Models with Viscosity Independent of Temperature

348 ### *4.1.1 Reference models*

349 Models 1 and 2 are the simplest explored in this paper. They were designed to be
350 as similar as possible, with a view to quantifying differences and similarities arising solely
351 from the choice of numeric or analytic methodology used to solve equations of motion
352 and to calculate surface deflections. Model 1 was parameterized with the radial viscos-
353 ity structure shown in Figure 2c. Radial viscosity used in other geodynamic studies are
354 shown alongside for comparison (Ghelichkhan et al., 2021; Mitrovica & Forte, 2004; Stein-
355 berger & Calderwood, 2006). Figure 2d shows spherical harmonic expansion of the sur-
356 face stress field predicted by Model 1 at 0 Ma (cf. Figure 2a). We call this result Model
357 1b. The original, full-resolution, numerical result is referred to as Model 1a.

358 Model 2 is the analytic model parameterized to be as similar as possible to Model
359 1. Its sensitivity kernel, generated assuming water loading ($\rho_w = 1030$ kg /m^3), free-
360 slip surface and CMB boundary conditions, and the radial viscosity profile shown in Fig-
361 ure 2c, is shown in Figure 3a. Values of the other parameters used to generate these ker-
362 nels are stated in Table S1. Similar to many previous studies, the kernel indicates that
363 surface deflections will be especially sensitive (across all degrees incorporated, $l \leq 50$)
364 to density anomalies in the upper mantle (Parsons & Daly, 1983; Hager & Clayton, 1989;
365 Ghelichkhan et al., 2021). Models 1 and 2 are used as points of reference for other more
366 complex models explored in the remainder of this paper.

367 ### *4.1.2 Gravitation*

368 We start by incorporating more complex parameterizations of gravitation. The an-
369 alytic Model 3 was parameterized in the same way as Model 2 with the addition of ra-
370 dial gravitation (following Hager & Clayton, 1989; Panasyuk et al., 1996, see Equation
371 5). The solid curve in Figure 4b shows the radial gravity function used to calculate sur-
372 face deflections. It was generated using the density distribution produced by (the nu-
373 merical) Model 1a (see Figure S1) by calculating

$$g(r) = \frac{4\pi G}{r^2}\left[\int_{R_{\mathrm{CMB}}}^{r} \bar{\rho}(r')\, r'^2\, \mathrm{d}r'\right] + F_{core}, \tag{10}$$

374 where $\bar{\rho}(r)$ is layer mean density and F is a factor chosen to account for core mass, and
375 such that $g = 9.8$ m s^{-2} at the surface. This formulation is derived from Gauss's law
376 assuming spherically symmetric density, combined with Newton's law of universal grav-
377 itation (Turcotte & Schubert, 2002).

378 The analytic Model 4 incorporates stress perturbations induced by deflections of
379 the gravitational potential field. This model assumes $g = 10$ m s^{-2} everywhere, even
380 within the deflected surface layer, as was the case for Models 1–2. Following Hager and
381 Clayton (1989) and Panasyuk et al. (1996), when solving for surface deflection using prop-
382 agator matrices, the effect on flow of perturbation of gravitational potential is included
383 via the u_3 term in Equation 6 (see also Ribe, 2007; Ricard, 2015). Sensitivity kernels for
384 Models 3 and 4 are shown in Figure S6. TERRA simulations do not include this com-
385 ponent in flow calculations (see Supporting Information).

386 ### *4.1.3 Discarding Shallow Structure*

387 The uppermost few hundred kilometers of geodynamic simulations are often not
388 included in predictions of surface deflections (see e.g. Flament et al., 2013; Flament, 2018;

Davies et al., 2019, and references therein). To quantify the impact of discarding shallow structure on our calculations, we examine differences in calculated deflections in the spatial and spherical harmonic domains. We present three tests, resulting in Models 5, 6 and 7, where structure shallower than 50, 100 and 200 km is removed from Model 2.

4.1.4 Changing Boundary Conditions

Up to now, we have only considered instantaneous analytic and numeric solutions for surface deflection where both the surface and CMB have free-slip conditions imposed (i.e., vertical component of flow velocity $\mathbf{u_r} = 0$, horizontal components are allowed to freely vary). No gradient/Neumann constraint (e.g., on $\partial\mathbf{u}/\partial z$) is imposed. This condition is generally deemed appropriate for the surface of the convecting mantle, and CMB, since at both boundaries, cohesion within convecting mantle is thought to be much stronger than adhesion to the boundary. Analytic solutions for sensitivity kernels for propagator matrices also exist for no-slip Dirichlet boundary conditions, where horizontal components of $\mathbf{u} = 0$, which may be more appropriate when the Earth's lithosphere is implicitly included in mantle convection models, as is the case here (Parsons & Daly, 1983; Thoraval & Richards, 1997). Therefore, we test the effect of changing the surface boundary condition to no-slip on predicted surface deflections (Model 8). Although there is little reason to believe the adhesion of the CMB would be strong, for completeness, we test scenarios in which no- and free-slip conditions are assumed for the CMB and the surface, respectively (Model 9), and both have no-slip conditions (Model 10).

4.2 Models with Temperature-Dependent Viscosity

We investigate the impact of including the temperature dependence of viscosity, $\eta(r, T)$, on predicted global mantle flow in numeric models, and on subsequent estimates of surface deflection. We do so by first generating the numeric Model 11, which is identical to Model 1 in terms of all boundary conditions, initialization, and physical parameters, except for the fact that viscosity depends on temperature in the manner described by Equation 7 in Supporting Information.

The radial distribution of viscosity, but not its absolute value, plays a crucial role in determining sensitivity of instantaneous solutions for surface deflections to density (and thermal) anomalies in the mantle (e.g., Parsons & Daly, 1983; Hager, 1984). Consequently, to assess sensitivity of surface deflections to arbitrary changes to radial viscosity, $\eta(r)$, we performed a suite of analytic tests. Since the analytic approaches require viscosity to only vary as a function of radius, we first test the impact of inserting layer-mean viscosity from the present-day 3D temperature-dependent viscosity structure predicted by numeric Model 11 (Figure S8). This parameterization is used to generate (the analytic) Model 12. The sensitivity kernel for Model 12 is shown in Figure S11a.

We stress that in Models 3–10 analytic instantaneous solutions for surface deflection, with adjusted parameters and boundary conditions, were simply compared with Model 2; no new numeric models were generated using TERRA. In contrast, the additional tests examined here correspond to a new TERRA model (Model 11) in which temperature dependence of viscosity affects mantle flow across the entire run time.

The sensitivity of surface deflections to arbitrary modification of upper and lower mantle viscosity and densities were then examined. Mean upper and lower mantle (radial) temperature-dependent viscosity was decreased or increased by an order of magnitude from that used to generate Model 12 (see solid black curve in Figure 8). The resultant impact on calculated surface deflections (Models 13–16) was quantified by comparison with results generated using reference Model 12 (Figure S11). Figures 8i–l and S14 show the amplitudes of density anomalies in the upper and lower mantle that were systematically increased or decreased to generate Models 17–20. Similar to the tests shown

in Figures 8a–h and S13, densities are amplified relative to Model 12. Radial viscosity is constant for each of these tests (black curve in Figure 8a; i.e., same as that used to generate Model 12).

5 Results

5.1 Models with Viscosity Independent of Temperature

5.1.1 Reference Models: Comparing Numeric and Analytic Solutions

We first compare solutions generated from numeric Model 1a, with its spherical harmonic representation (Model 1b), and analytic Model 2, which were designed to be as similar as possible. Figure 1g–h shows calculated densities that arise in Model 1a at 0 and 100 Ma (see Figure S1 for extended results). The history of plate motions used to drive these models is also indicated on these figures. The resultant normal stresses, σ_{rr}, calculated at the surface of Model 1, and associated statistics are shown in Figure 2a–b. By convention, positive stresses imply compression and hence downward surface deflection, which could be manifest as lithospheric drawdown, i.e., subsidence. Prominent regions of positive stress anomalies in this model include locations atop imposed collision zones, where subduction naturally results, e.g., along the Pacific margin of South America. Negative stresses imply dilation and hence positive lithospheric support (i.e., surface uplift). Figure 2a shows dilatational stresses beneath Southern Africa, for example, and along mid-oceanic ridges in the Indian and Atlantic Oceans.

Surface stresses calculated by fitting radial stresses from Model 1a with a global spherical harmonic interpolation up to maximum degree $l = 50$, i.e., minimum wavelength of ≈ 800 km, is shown in Figure 2d–e. The resultant power spectrum in terms of total power at each degree is shown in Figure 2f. Aside from the lack of structure at degree 0, amplitudes decrease steadily with increasing degree (i.e., decreasing wavelength) and can be approximated by red noise. The spherical harmonic representation of deflections calculated by converting stress using Equation 2, assuming water loading, are shown in Figures 2g and S2. A comparison of calculated power spectra, expected surface deflection from Kaula's rule (Equation 3), and spectra generated from observed residual ocean age-depth measurements is also included in Figures 2 and S2 (Kaula, 1963; Hoggard et al., 2016; Holdt et al., 2022). For completeness, surface deflections calculated assuming air loading are shown in Figure S2f-j.

Surface deflections predicted by Model 2 and its associated sensitivity kernel are shown in Figure 3a-b. An expanded set of results including sensitivity kernels for water and air loading, and histograms of deflection and associate power spectra are included in Figure S3.

Deflections predicted from these numeric and analytic models are visually similar (cf. Figures 2g & 3b). Absolute differences in amplitudes are greatest close to subduction zones (e.g., in South America and Asia; Figure 3c). The differences are broadly normally distributed and centred on 0 (Figure 3d). The spherical harmonic correlation between these models is high (close to 1 for all degrees; cf. Forte, 2007, Figure 3e). The ratios between surface deflection values in these predictions indicate that analytic solutions tend to be damped compared to numeric solutions. This result is emphasized by the histogram shown in Figure 3g. Multiplying amplitudes of deflections from the propagator matrix solutions by a factor of 1.1 brings them in-line with the numeric solutions. These results indicate that the propagator matrix approach dampens solutions by $\approx 10\%$. We note that power spectral slopes between Model 1b and 2 are similar (cf. Figures 2i and S3d). These and all other results are discussed in Section 6.

5.1.2 Incorporating Self-Gravitation and Gravitational Potential of the Deflected Surface

Differences in deflections predicted by Model 2, which assumes constant $g = 10$ m s^{-2} across all radii, and Model 3, which incorporates self-consistently calculated radial gravitation, are shown in Figure 4a and 4c. Deviations in predicted instantaneous deflections are $\sim 10\%$ of maximum amplitudes predicted by Model 2 (see Table 2). Note that, for the viscosity structure used in these models, changing g in this way impacts sensitivity kernels most at low degrees $l \lesssim 10$ in the mid-mantle (see Figures 2c, 3a and S6).

We suggest that the broadly hemispherical differences in calculated deflections arise from three contributing factors. First, deviations in g between the two models are greatest in the mid-mantle, which, secondly, results in subtly different sensitivity kernels (see Figure S6). In general, surface deflection sensitivity to mid-mantle structure is highest at low degrees (l =1–3), and is almost negligible at higher degrees compared to contributions from the near-surface. Thus it seems likely that differences between these kernels would be manifest in low-degree (e.g. hemispherical) differences in surface deflections. Third, in the final timestep, which is used to calculate deflections, there occurs a greater proportion of negative and positive deflections in the northern and southern hemispheres, respectively.

We note that incorporating radially varying gravitation into numeric simulations, which is not trivial, might materially impact calculated mantle flow fields and hence predictions of surface deflections. Our results are consistent with the rule of thumb outlined in Section 7.02.2.5.2 of Ricard (2015), whereby magnitudes of differences incurred by inclusion of full self-gravitation, i.e., $g(\theta, \phi, r)$, decay as a function of spherical harmonic degree, proportionately to $3/(2l + 1)$.

As expected, induced differences in surface displacement predictions are much lower in magnitude when gravitational potential of the deflected surface is included compared to when radial gravitation is incorporated (cf. Figure 4a and 4d). We note that they are of the same order of magnitude as the geoid height anomalies predicted by these models. The mean Euclidean distance between the two predicted surfaces in Models 2 and 4 is only $\sim$110 m (compared to maximum amplitudes > 8 km), and the spherical harmonic correlation is very high across all degrees (see Table 2). Similar to the results for Model 3, the differences are concentrated at low spherical harmonic degree l. We stress that this test investigates the effect of the u_3 term on instantaneous solution for surface deflection (Equation 5). It cannot be ruled out from this test that inclusion of the effect of gravitational potential field perturbation would result in greater differences across the entire model run time of a numeric model, although it is unlikely (Zhong et al., 2008).

5.1.3 Excising Shallow Structure

As expected from examination of surface deflection sensitivity kernels (e.g., Figure 3a), removal of shallow structure (Models 4–6) results in significantly reduced amplitudes of surface deflections (Figure 5). Doing so results in amplitudes of power spectra that more closely align with independent estimates (Figure 5b, f, j). The reduction in differences is largely due to the fact that the reference Model 2 has surface deflections that are much larger than independent estimates of dynamic topographic power across all degrees. We note that power spectral slopes for predicted surface deflection from Model 2 are close to those generated from Kaula's rule, and observed oceanic residual depths (Figures 2i, S2 and S3). Removing shallow structure steepens spectral slopes (i.e., reduces power at high degrees) beyond those expected from theoretical considerations (Kaula's rule) or observed from oceanic residual depths, akin to results from other work that excised shallow structure (e.g., Flament et al., 2013; Moucha et al., 2008; Steinberger, 2007). This result is emphasized by calculated spectral coherence, r_l, between deflections with

and without shallow structure removed (cf. Figure 5b, d, f). While degree 1 and 2 structure remains coherent, coherence across degrees $\gtrsim$ 20 decreases from $\sim$ 0.9 to as low as 0.5, which are the largest discrepancies between any models examined in this study (Figure S7).

5.1.4 Adjusting Boundary Conditions

Figure 6a, e and i show predicted sensitivity kernels as a function of depth and degree, for no-slip/free-slip, free-slip/no-slip and no-slip/no-slip boundaries respectively, where the first condition is the surface slip condition, and the second the CMB slip condition. Differences to the sensitivity kernel for Model 2 (free-slip/free-slip; Figure 3a) are shown in panels b, f and j. Those panels, and panels c, g and k, demonstrate that when the surface boundary condition is 'no-slip', there is decreased sensitivity to short wavelength shallow structure, and increased sensitivity to long-wavelength (low degree) structure across all depths. Figure 6d, h and l reveal that induced misfit in the spatial domain is impacted to a greater degree than in tests of gravitation (Models 3 & 4), but not necessarily more severely than for removal of, say the upper 200 km of density structure from surface deflection calculations. Spectral correlation with Model 2 is most severely impacted when both surface and CMB boundaries are no-slip, which is probably physically unrealistic (Model 7; see Table 2; Section 4.1.4).

5.2 Adjusting Viscosity and Density Anomaly Amplitudes

5.2.1 Temperature-Dependent Viscosity

Slices through the three-dimensional viscosity and density structure of Model 11, which incorporated temperature-dependent viscosity, are shown in Figure 1a, c and e. Density anomalies in the models parameterized with temperature-dependent viscosity are more localised ('sharper') than in the models with viscosity independent of temperature (e.g., Model 1; see Figures 7 & S8–S10). This result is unsurprising since temperature-dependent viscosity provides stronger mechanical contrasts between cooler subducting regions and surrounding asthenosphere (cf. Figure 1g–h & S9; Zhong et al., 2000). Nonetheless, power spectra of calculated surface deflections are very similar (cf. Figure S10j & 2i). This result emphasises the relatively small impact incorporating temperature-dependent viscosity has on surface deflections compared to, say, excising shallow structure.

Calculated power spectra from the analytic Model 12, which was generated using layer-mean (radial) viscosity from Model 11a, reinforces this view (cf. Figure S3a-d & Figure S11a-d). Similar to the results obtained for models without temperature-dependent viscosity (Figure 3), deflections calculated analytically are damped relative to numeric solutions (see Figure 7f). The best fit amplification factor to align propagator matrix and numeric solutions is 1.24 (24%). The effect is greater than that seen when comparing Models 1b and 2 because of increased short wavelength structure in Model 11 (see also Zhong et al., 2000). Nonetheless, spherical harmonic correlations, r_l, are > 0.75 for all degrees examined ($l \leq 50$), and > 0.85 for most degrees. Cell-to-cell differences in surface deflections are broadly normally distributed and centred on zero (Figure 7d).

A summary of comparisons between models with and without temperature-dependent viscosity is shown in Figure S12. Discrepancies in cell-to-cell deflections are broadly normally distributed and centred on zero, clustering along the 1:1 relationship with maximum $\chi = 1.51$ for full resolution (numeric) models (Figure S12b-c; see Table 2). Unsurprisingly, spherical harmonic fits and analytic results have tighter normal distributions and lower χ values. Correlation coefficients are > 0.75 for nearly all degrees in all comparisons.

5.2.2 Sensitivity to Upper/Lower Mantle Viscosity and Density Anomalies

In order to explore the consequences of modified viscosity and density on calculated deflections we also systematically increased and decreased contrasts in the upper and lower mantle (Models 13–20) with respect to Model 12. Figure 8 summarises the results, which include decreasing upper mantle viscosity by an order of magnitude and show the impact of using increasingly simple radial viscosity in analytic calculations. Calculated sensitivity kernels for the adjusted viscosity profiles demonstrate that decreasing upper mantle viscosity reduces sensitivity of surface deflections to long-wavelength density structure, especially in the lower mantle (Figures S13 & 8d, f, h). Models 13–16 have broad similarities with the reference Model 12 even when $\eta(r)$ is drastically varied: average χ misfit = 0.17–0.38 km, and $r_l > 0.97$ across all degrees. These results emphasize that the viscosity adjustments we examined exert a relatively minor control on the amplitudes of instantaneous surface deflection (Table 2, see, e.g., Ghosh et al., 2010; Moucha et al., 2007; Lu et al., 2020).

In contrast, increasing (Model 17) or decreasing (Model 18) upper mantle densities is much more impactful on amplitudes of calculated surface deflections (see Figure 8i–l, and S14). For instance, increasing or decreasing upper mantle densities by a factor of two (relative to Model 12) results in χ values of 0.97 and 0.48, respectively. Modifying lower mantle densities has a much smaller impact on amplitudes of deflection (Models 18 & 19). Spherical harmonic correlation between models is approximately as good as for the radial viscosity tests (Models 13–16), which is to be expected since we do not vary locations of density anomalies here, only their amplitudes, and r_l is insensitive to amplitudes of the two results being compared. Significant is the fact that mean vertical differences between Models 17–20 and 12 (i.e., χ and $\Delta\bar{h}$) are higher than those calculated for Models 13–16 (in which viscosity is varied; see Table 2).

These results emphasize the relative sensitivity of instantaneous surface deflections to upper mantle density anomalies compared to, say, radial viscosity or lower mantle densities. Even quite large uncertainties in lower mantle density anomalies have relatively little impact on instantaneous surface deflections. These results reinforce the view that accounting for shallow (e.g., lithospheric and asthenospheric) densities is crucial when estimating surface deflection, and dynamic topography, from mantle convection simulations (e.g., Colli et al., 2016; Flament et al., 2013; Holdt et al., 2022; Wang et al., 2022).

6 Discussion

6.1 Similarities of Analytic and Numeric Solutions

In this paper we compare numeric and analytic predictions of instantaneous surface deflections generated by mantle convection simulations. First, we simply compared predictions from numeric and analytic approaches parameterised to be as similar as possible. In this test, the models were purposefully simple: viscosity is radial, models are incompressible, and they do not include self-gravitation, or radial variation in g. Numeric solutions were transformed into the frequency (spherical harmonic) domain so that they could be compared with analytic solutions, and so that power spectra could be directly compared at appropriate scales. The results show that, for as-similar-as-possible parameterizations, amplitudes of analytic solutions are $\approx 10\%$ lower than numeric solutions (Figure 3). If the numeric model incorporates temperature-dependent viscosity, this discrepancy increases to 25% (Figure 7). We interpret these results in two ways. First, once armed with viscosity and density fields, numeric and analytic approaches broadly yield

Table 2. Inter-model comparison of predicted surface deflections. Models being compared are summarised in Table 1. Metrics: root-mean-squared difference (χ, km), mean Euclidean (L^2-norm) difference in predicted deflection ($\Delta\bar{h}$, km), and mean spherical harmonic correlation between models ($\bar{r}_l$). Standard deviation of r_l distribution across degrees (s_r) is also stated: note that $r_l \leq 1$. All spherical harmonic representations of output from numeric code and generated by the propagator matrix code are expanded up to maximum degree, $l = 50$. See body text, figures referred to in column 6, and Table 1 for details.

Models	χ	$\Delta\bar{h}$	$\bar{r}_l$	s_r	Figures
1b & 2	0.95	0.69	0.97	0.02	3
2 & 3	0.57	0.47	0.99	4×10^{-4}	4
2 & 4	0.13	0.11	0.99	2×10^{-5}	4
2 & 5	0.67	0.48	0.93	0.04	5a-b
2 & 6	1.03	0.74	0.87	0.06	5c-d
2 & 7	1.57	1.12	0.63	0.15	5e-f
2 & 8	1.26	1.04	0.99	1×10^{-3}	6a-d
2 & 9	1.09	0.97	0.99	0.04	6e-h
2 & 10	1.00	0.74	0.96	0.28	6i-l
1a & 11a	1.51	1.04	—	—	S12a-c
1b & 11b	1.44	0.98	0.79	0.26	S12d-g
11b & 12	1.20	0.80	0.95	0.02	7
2 & 12	0.92	0.64	0.85	0.27	S12h-k
12 & 13	0.31	0.20	0.99	9×10^{-3}	8a-b, S13a-d
12 & 14	0.17	0.10	0.99	3×10^{-3}	8c-d, S13e-h
12 & 15	0.32	0.20	0.98	0.01	8e-f, S13i-l
12 & 16	0.38	0.23	0.98	0.01	8g-h, S13m-p
12 & 17	0.97	0.64	0.98	7×10^{-3}	8i, S14a-c
12 & 18	0.48	0.32	0.98	6×10^{-3}	8j, S14d-f
12 & 19	0.43	0.29	0.99	3×10^{-3}	8k, S14g-i
12 & 20	0.22	0.14	0.99	1×10^{-3}	8l, S14j-l

similar estimates of surface deflections. Second, the relatively damped analytic solutions are a consequence of smoothing steps in the propagator matrix approach.

The smoothness of analytic solutions, and subsequent damping of topographic amplitudes, is perhaps surprising, given the fact that they are being compared with numeric models expanded into the spherical harmonic domain to the same maximum degree, $l = 50$. However, the surface stresses used to generate Model 1a have full horizontal resolution (≈ 45 km) across depths, and *only* the surface layer is smoothed by spherical harmonic fitting, to generate Model 1b. Therefore, Model 1b inherently contains some contribution from degrees ≥ 50, in the sense that finer-resolution density structure at depth could affect longer-wavelength flow nearer the surface. In contrast, to generate the analytic solution (Model 2), the density structure of each layer of the model is smoothed, by expansion to maximum $l = 50$, *before* integration of their contributions to surface deflection. The analytic solution would provide a better match to stress estimates from numeric models if such estimates were calculated using density structure smoothed to the same maximum l across all depths, which is currently challenging (see Section 1.1).

Nonetheless, the similarity of results indicates that the relatively low-cost propagator matrix approach can be used to explore consequences of including additional model complexity. A systematic sweep of parameters, including radial gravitation (Figure 4a-c) and gravitational potential field effects (Figure 4d-e) indicates that their effects on surface deflection are relatively modest. A useful rule of thumb is that self-gravitation perturbs instantaneous surface deflections by $O(1\text{–}10)\%$ when compared to models with constant gravitational acceleration, and even less difference is observed at high degree (e.g., Ricard, 2015, their Section 7.02.2.5.2). Incorporating the effect of deflections of gravitational potential field on flow has a modest impact on amplitudes of surface deflections at degrees 1–2, but overall it contributes even less than radial variation in g to surface deflections across the scales of interest. We note that incorporating full 3-D self-gravitation into numeric simulations is currently challenging. Nonetheless, establishing its impact on the flow field over time, and resultant impact on surface deflections, may be important future work.

6.2 Importance of Viscosity and Shallow Density Anomalies for Isolating Dynamic Support

Figure 8 demonstrates that even quite large (order of magnitude) variations in viscosity do not have much impact on instantaneous surface deflections when compared to, say, modified upper mantle density anomalies, which appears to agree with the results of Davies et al. (2019) (see also Flament, 2019; Steinberger et al., 2019). Assuming no-slip boundary conditions at Earth's surface may be appropriate for driving near-surface (lithospheric) flow throughout the main model run time, but it less clear whether no- or free-slip boundary conditions are most appropriate for calculating instantaneous dynamic topography (see, e.g., Forte & Peltier, 1994; Thoraval & Richards, 1997). Nonetheless, all calculated sensitivity kernels in this study indicate that shallow density anomalies make significant contributions to surface topography regardless of viscosity profile or boundary conditions chosen (e.g., Figure 3a; see also Colli et al., 2016; Parsons & Daly, 1983).

It is well known that disentangling contributions to Earth's surface topography from mantle convection, lithospheric isostasy and flexure is important but not trivial (see, e.g., Davies et al., 2019; Cao & Liu, 2021; Fernandes & Roberts, 2021; Hoggard et al., 2021; Steinberger, 2016; Stephenson et al., 2021; Zhou & Liu, 2019; Wang et al., 2022). Previous studies simulating mantle convection have addressed this issue by discarding density anomalies in radial shells shallower than specified depths before calculating surface stresses (e.g., Spasojevic & Gurnis, 2012; Flament et al., 2013; Molnar et al., 2015). Similarly, analytic approaches have isolated contributions from the convecting mantle by only

incorporating information from deep shells (e.g., Colli et al., 2018). This method has the advantage of effectively removing the effect of lithospheric cooling through time from surface deflection estimates. It also avoids the need to incorporate, say, realistic crustal or depleted lithospheric layers within the viscous flow parameterization. However, uncertain oceanic and continental lithospheric thicknesses mean that choosing appropriate cut-off depths is not simple.

Out of all the tests performed in this study, removing shallow structure resulted in the largest impact on predicted surface deflections. It modifies amplitudes of deflections, locations of uplift and subsidence, and degrees over which they are resolved, and hence modifies power spectral scalings (Table 2, Figure 5). Making quantitative predictions of dynamic topography from such an approach is fraught for at least two reasons. First, if the chosen depth is shallower than the lithosphere-asthenosphere boundary in places, plate and sub-plate contributions to topography will be entangled. Second, discarding deeper layers to ensure that all plate contribution is definitely avoided means that some contributions from asthenospheric flow will be missed. Thus, such a step is unlikely to be desirable if mantle flow models are to be used to understand, say, lithospheric vertical motions, or vice versa (see e.g., Figure 3a; Davies et al., 2019; Hoggard et al., 2016). Given the calculated sensitivity kernels, excising layers in the upper few 100 km is likely to result in predictions of surface deflections that are especially inaccurate at short wavelengths, i.e., high spherical harmonic degree. An alternative approach, which may be fruitful future work, is removal of structure based on appropriately calibrated plate models, or globally averaged age-dependent density trends (e.g., F. D. Richards et al., 2020, 2023).

6.3 Assessing 'Effective' Contributions to Instantaneous Deflections

The results emphasise the importance of considering sensitivities of instantaneous vertical surface deflections to the location and scale of flow in the mantle. Taking inspiration from Hager and O'Connell (1981) and Parsons and Daly (1983), we calculate the net contributions from density anomaly structure to deflections, as a function of radius, latitude and longitude across all spherical harmonic degrees considered (i.e., $l = 1$ to 50). Contributions to deflections from densities at particular radii r, across all spherical harmonic degrees and orders, for each latitude and longitude, (θ, ϕ), are calculated such that

$$h_e(\theta, \phi, r) = \sum_{l=1}^{L} \sum_{m=-l}^{m=l} \left[Y_{lm}(\theta, \phi) \cdot \delta\rho_{lm}(r) \cdot A_l(r) \cdot \Delta r \right], \tag{11}$$

where Δr is the radial width of the spherical shell included in the calculation (≈ 45 km for all shells from the surface to the CMB; see Supporting Information) and Y_{lm} are spherical harmonic coefficients. Mean density anomalies, $\delta\rho_{lm}$, within each shell at each latitude and longitude, and sensitivities A_l at the top of each shell are used to calculate h_e (see Section 2.3). Contributions at specific locations to surface deflections as a function of latitude and longitude, and spherical shell depth are shown in Figure 9 for Model 12, for $1 \leq l \leq 50$. Results for lower maximum degrees are shown in Supporting Information. Panels a-d show slices through effective density in the upper (at 45, 135, 360 km) and lower mantle (1445 km). A 180° cross-section showing effective densities from the core-mantle-boundary to the surface beneath the Pacific to the Indian Ocean encompassing South America and southern Africa (the same transect as shown in Figure 1) is shown in panel e. This figure again emphasizes the contribution of density anomalies in the upper mantle to surface deflections, and the risks associated with discarding shallow structure when predicting dynamic topography.

6.4 Summary and Future Work

Encouragingly, although predicted instantaneous surface deflections are sensitive to different parameterizations, broadly coherent patterns emerge in all models tested. Moreover, calculated deflections are relatively insensitive to the methodologies used to solve the equations of motion. For instance, incorporation of gravitational potential of deflected surfaces, self-gravitation and viscosity anomalies each generate subtly different surface deflections. Choosing to solve the equations of motion analytically or numerically changes calculated deflections by $< 25\%$, even when temperature-dependent viscosity is included throughout the duration of a simulation.

In contrast, removal of shallow structure produces much larger discrepancies between predicted deflections. For instance, surface deflections calculated using the entire modelling domain (core-mantle boundary to surface) have spectral slopes consistent with those of oceanic age-depth residuals, however amplitudes are over-predicted by 1–2 orders of magnitude. In contrast, by not including the shallowest 200 km, calculated power spectra more closely match observed amplitudes, especially at spherical harmonic degrees > 10 (Figure 5). However, the spectral slopes of predicted deflections are redder than for the oceanic residuals, which implies that a different approach to removing the contribution of lithospheric structure is required.

An obvious necessary next step for accurately predicting modern dynamic support from mantle convection simulations is to incorporate accurate information about lithospheric structure from, for instance, tomographic models (e.g., Priestley & McKenzie, 2013; F. D. Richards et al., 2020). Another useful next step is to establish sensitivity of surface deflections to time-dependent parameters that impact predicted flow histories, including plate motions. The results in this paper indicate that comparing predicted and observed surface deflections, combined with knowledge of lithospheric structure, could be used to identify optimal models.

Finally, the body of geologic and geomorphologic observations that could be used to test predicted histories of surface deflections from mantle convection simulations has grown substantially in the last decade (e.g., uplift and subsidence histories; Section 1; see, e.g., Hoggard et al., 2021, and references therein). A suite of other geologic and geophysical observables are also predicted by, or can be derived from, such simulations (e.g., mantle temperatures, heat flux, geoid, seismic velocities, true polar wander). Using them alongside histories of surface deflections to identify optimal simulations is an obvious avenue for future work (e.g., Ball et al., 2021; Lau et al., 2017; Panton et al., 2023; F. D. Richards et al., 2023). Using such data and the methodologies explored in this paper may be a fruitful way of identifying optimal simulations from the considerable inventory that already exists.

7 Conclusions

This study is concerned with quantifying sensitivities and uncertainties of Earth's surface deflections that arise in simulations of mantle convection. Calculated sensitivities of instantaneous deflection of Earth's surface to mantle density structure emphasise the importance of accurate mapping of the upper mantle. Surface deflections are somewhat sensitive to the distribution of viscosity throughout the mantle, but especially to the locations and scales of density anomalies in the upper mantle. The largest discrepancies between predicted deflections seen in this study are generated when upper mantle structure is excised or altered. Doing so changes both the amplitude and distribution of calculated deflections, modifying their power spectral slopes. These results emphasise the importance of incorporating accurate models of lithospheric structure into calculation of sub-plate support of topography, and also the need to accurately determine plate contributions to topography. In contrast, the choice of methodology to es-

timate surface deflections—analytic or numeric—or boundary conditions are relatively small sources of uncertainty. Similarly, assumed gravitational profiles and temperature dependence of viscosity are relatively minor contributors to uncertainty given reasonable, Earth-like, parameterizations. Nonetheless, these parameterizations may impact surface deflections through their role in determining how upper mantle flow evolves through geologic time. A fruitful next step could be to use the approaches developed in this paper, in combination with careful isolation of plate cooling signatures from surface deflection predictions, to test mantle convection simulations using the existing and growing body of geologic, geomorphologic and geophysical observations.

Open Research Section

TERRA models are archived [here]. The propagator matrix code is archived [here]. Parameterization files are archived [here]. [TO ED: this section will be completed upon final submission, when confirmation of the precise models published is obtained after review.]

Acknowledgments

We thank A. Biggin, H. Brown, C. Davies, A. Ferreira, M. Holdt, P. Japsen, P. Koelemeijer, F. M^{c}Nab, R. Myhill and J. Ward for helpful discussion. We also thank N. Flament and an anonymous reviewer for helping us to clarify our thesis. C.O., J.P. and V.M.F. were supported by NERC Grant NE/T01684/1.

References

Al-Hajri, Y., White, N., & Fishwick, S. (2009). Scales of transient convective support beneath Africa. *Geology*, *37*(10), 883–886. doi: 10.1130/G25703A.1

Bahadori, A., Holt, W., & Feng, R. e. a. (2022). Coupled influence of tectonics, climate, and surface processes on landscape evolution in southwestern North America. *Nat Commun*, *13*(4437). doi: 10.1038/s41467-022-31903-2

Ball, P. W., Duvernay, T., & Davies, D. R. (2022). A coupled geochemical-geodynamic approach for predicting mantle melting in space and time. *Geochemistry, Geophysics, Geosystems*, *23*, 1–31. doi: 10.1029/2022gc010421

Ball, P. W., White, N. J., Maclennan, J., & Stephenson, S. N. (2021). Global Influence of Mantle Temperature and Plate Thickness on Intraplate Volcanism. *Nature Communications*, *12*(2045), 1–13. doi: 10.1038/s41467-021-22323-9

Bangerth, W., Dannberg, J., Fraters, M., Gassmoeller, R., Glerum, A., Heister, T., ... Naliboff, J. (2023). ASPECT v2.5.0 [Computer software manual]. Retrieved 2023-08-04, from `https://zenodo.org/record/3924604` doi: 10.5281/zenodo.8200213

Bauer, S., Huber, M., Ghelichkhan, S., Mohr, M., Rüde, U., & Wohlmuth, B. (2019). Large-scale simulation of mantle convection based on a new matrix-free approach. *Journal of Computational Science*, *31*, 60–76. Retrieved from `https://doi.org/10.1016/j.jocs.2018.12.006` doi: 10.1016/j.jocs.2018.12.006

Baumgardner, J. R. (1985). Three-dimensional treatment of convective flow in the Earth's mantle. *Journal of Statistical Physics*, *39*(5-6), 501–511. doi: 10.1007/BF01008348

Becker, T. W., & Boschi, L. (2002). A comparison of tomographic and geodynamic mantle models. *Geochemistry, Geophysics, Geosystems*, *3*(1), 1–48. doi: 10.1029/2001GC000168

Biggin, A. J., Steinberger, B., Aubert, J., Suttie, N., Holme, R., Torsvik, T. H., ... Van Hinsbergen, D. J. (2012). Possible links between long-term geomagnetic variations and whole-mantle convection processes. *Nature Geoscience*, *5*(8),

526–533. doi: 10.1038/ngeo1521

Braun, J. (2010). The many surface expressions of mantle dynamics. *Nature Geoscience*, *3*(12), 825–833. doi: 10.1038/ngeo1020

Bunge, H.-P., & Baumgardner, J. R. (1995). Mantle convection modeling on parallel virtual machines. *Computers in Physics*, *9*(2), 207–215. doi: 10.1063/1.168525

Bunge, H.-P., Hagelberg, C. R., & Travis, B. J. (2003). Mantle circulation models with variational data assimilation: inferring past mantle flow and structure from plate motion histories and seismic tomography. *Geophysical Journal International*, *152*, 280–301. doi: 10.1046/j.1365-246X.2003.01823

Bunge, H.-P., Richards, M. A., & Baumgardner, J. R. (2002). Mantle-circulation models with sequential data assimilation: Inferring present-day mantle structure from plate-motion histories. *Philosophical Transactions of the Royal Society A: Mathematical, Physical and Engineering Sciences*, *360*(1800), 2545–2567. doi: 10.1098/rsta.2002.1080

Cao, Z., & Liu, L. (2021). Origin of Three-Dimensional Crustal Stress Over the Conterminous United States. *Journal of Geophysical Research: Solid Earth*, *126*(11), e2021JB022137. (e2021JB022137 2021JB022137) doi: https://doi.org/10.1029/2021JB022137

Chang, C., & Liu, L. (2021). Investigating the formation of the Cretaceous Western Interior Seaway using landscape evolution simulations. *GSA Bulletin*, *133*(1-2), 347–361. doi: 10.1130/B35653.1

Colli, L., Ghelichkhan, S., & Bunge, H.-P. (2016). On the ratio of dynamic topography and gravity anomalies in a dynamic Earth. *Geophysical Research Letters*, *43*, 2510–2516. doi: 10.1002/2016GL067929

Colli, L., Ghelichkhan, S., Bunge, H.-P., & Oeser, J. (2018). Retrodictions of Mid Paleogene mantle flow and dynamic topography in the Atlantic region from compressible high resolution adjoint mantle convection models: Sensitivity to deep mantle viscosity and tomographic input model. *Gondwana Research*, *53*, 252–272. doi: 10.1016/j.gr.2017.04.027

Corrieu, V., Thoraval, C., & Ricard, Y. (1995). Mantle dynamics and geoid Green functions. *Geophysical Journal International*, *120*(2), 516–523. doi: 10.1111/j.1365-246X.1995.tb01835.x

Craig, C. H., & McKenzie, D. (1987). Surface deformation, gravity and the geoid from a three-dimensional convection model at low Rayleigh numbers. *Earth and Planetary Science Letters*, *83*, 123–136. doi: 10.1016/0012-821X(87)90056-2

Crameri, F., Schmeling, H., Golabek, G. J., Duretz, T., Orendt, R., Buiter, S. J., ... Tackley, P. J. (2012). A comparison of numerical surface topography calculations in geodynamic modelling: An evaluation of the 'sticky air' method. *Geophysical Journal International*, *189*(1), 38–54. doi: 10.1111/j.1365-246X.2012.05388.x

Czarnota, K., Hoggard, M. J., White, N., & Winterbourne, J. (2013). Spatial and temporal patterns of Cenozoic dynamic topography around Australia. *Geochemistry, Geophysics, Geosystems*, *14*(3), 634–658. doi: 10.1029/2012GC004392

Dannberg, J., Eilon, Z., Faul, U., Gassmöller, R., Moulik, P., & Myhill, R. (2017). The importance of grain size to mantle dynamics and seismological observations. *Geochemistry, Geophysics, Geosystems*, *18*(8), 3034-3061. doi: 10.1002/2017GC006944

Davies, D. R., Davies, J. H., Bollada, P. C., Hassan, O., Morgan, K., & Nithiarasu, P. (2013). A hierarchical mesh refinement technique for global 3-D spherical mantle convection modelling. *Geoscientific Model Development*, *6*(4), 1095–1107. doi: 10.5194/gmd-6-1095-2013

Davies, D. R., Ghelichkhan, S., Hoggard, M. J., Valentine, A. P., & Richards, F. D.

(2023). Observations and Models of Dynamic Topography: Current Status and Future Directions. In J. Duarte (Ed.), *Dynamics of plate tectonics and mantle convection* (pp. 223–269). Elsevier. doi: 10.1016/B978-0-323-85733-8.00017-2

Davies, D. R., Valentine, A. P., Kramer, S. C., Rawlinson, N., Hoggard, M. J., Eakin, C. M., & Wilson, C. R. (2019). Earth's multi-scale topographic response to global mantle flow. *Nature Geoscience*, *12*, 845–850. doi: 10.1038/s41561-019-0441-4

Fernandes, V. M., & Roberts, G. G. (2021). Cretaceous to Recent net continental uplift from paleobiological data: Insights into sub-plate support. *GSA Bulletin*, *133*, 1–20. doi: 10.1130/b35739.1

Fernandes, V. M., Roberts, G. G., White, N., & Whittaker, A. C. (2019). Continental-Scale Landscape Evolution: A History of North American Topography. *Journal of Geophysical Research: Earth Surface*, *124*, 1–34. doi: 10.1029/2018jf004979

Fichtner, A., Kennett, B. L. N., Igel, H., & Bunge, H.-P. (2009). Full seismic waveform tomography for upper-mantle structure in the Australasian region using adjoint methods. *Geophysical Journal International*, *179*(3), 1703–1725. doi: 10.1111/j.1365-246X.2009.04368.x

Fichtner, A., Trampert, J., Cupillard, P., Saygin, E., Taymaz, T., Capdeville, Y., & Villaseñor, A. (2013). Multiscale full waveform inversion. *Geophysical Journal International*, *194*, 534–556. doi: 10.1093/gji/ggt118

Fichtner, A., & Villaseñor, A. (2015). Crust and upper mantle of the western Mediterranean - Constraints from full-waveform inversion. *Earth and Planetary Science Letters*, *428*, 52–62. doi: 10.1016/j.epsl.2015.07.038

Flament, N. (2018). Present-day dynamic topography and lower-mantle structure from palaeogeographically constrained mantle flow models. *Geophysical Journal International*, *216*(3), 2158–2182. doi: 10.1093/gji/ggy526

Flament, N. (2019). Present-day dynamic topography and lower-mantle structure from palaeogeographically constrained mantle flow models. *Geophysical Journal International*, *216*(3), 2158–2182. doi: 10.1093/gji/ggy526

Flament, N., Gurnis, M., & Muller, R. D. (2013). A review of observations and models of dynamic topography. *Lithosphere*, *5*(2), 189–210. doi: 10.1130/L245.1

Flament, N., Gurnis, M., Müller, R. D., Bower, D. J., & Husson, L. (2015). Influence of subduction history on South American topography. *Earth and Planetary Science Letters*, *430*, 9–18. doi: 10.1016/j.epsl.2015.08.006

Foley, S. F., & Fischer, T. P. (2017). An essential role for continental rifts and lithosphere in the deep carbon cycle. *Nature Geoscience*, *10*(12), 897–902. doi: 10.1038/s41561-017-0002-7

Forte, A. M. (2007). Constraints on Seismic Models from Other Disciplines - Implications for Mantle Dynamics and Composition. In B. Romanowicz & A. Dziewonski (Eds.), *Seismology and the structure of the earth* (pp. 805–858). Elsevier B.V. doi: 10.1016/B978-044452748-6.00027-4

Forte, A. M., & Peltier, R. (1991). Viscous Flow Models of Global Geophysical Observables 1. Forward Problems. *Journal of Geophysical Research*, *96*(B12), 20131–20159. doi: 10.1029/91JB01709

Forte, A. M., & Peltier, W. R. (1994). The Kinematics and Dynamics of Poloidal-Toroidal Coupling in Mantle Flow: The Importance of Surface Plates and Lateral Viscosity Variations. *Advances in Geophysics*, *36*, 1–119. doi: 10.1016/S0065-2687(08)60537-3

French, S. W., & Romanowicz, B. (2015). Broad plumes rooted at the base of the Earth's mantle beneath major hotspots. *Nature*, *525*(7567), 95–99. doi: 10.1038/nature14876

Galloway, W. E., Whiteaker, T. L., & Ganey-Curry, P. (2011). History of Cenozoic North American drainage basin evolution, sediment yield, and accumulation in the Gulf of Mexico basin. *Geosphere*, *7*(4), 938–973. doi:

10.1130/GES00647.1

Gantmacher, F. R. (1959). *The Theory of Matrices*. New York: Chelsea Publishing Company.

Ghelichkhan, S., Bunge, H.-P., & Oeser, J. (2021). Global mantle flow retrodictions for the early Cenozoic using an adjoint method: Evolving dynamic topographies, deep mantle structures, flow trajectories and sublithospheric stresses. *Geophysical Journal International*, *226*(2), 1432–1460. doi: 10.1093/gji/ggab108

Ghosh, A., Becker, T. W., & Zhong, S. J. (2010). Effects of lateral viscosity variations on the geoid. *Geophysical Research Letters*, *37*(1), 2–7. doi: 10.1029/2009GL040426

Ghosh, A., & Holt, W. E. (2012). Plate Motions and Stresses from Global Dynamic Models. *Science*, *335*(6070), 838–843. doi: 10.1126/science.1214209

Glišović, P., & Forte, A. M. (2016). A new back-and-forth iterative method for time-reversed convection modeling: Implications for the Cenozoic evolution of 3-D structure and dynamics of the mantle. *Journal of Geophysical Research: Solid Earth*, *121*(6), 4067–4084. doi: 10.1002/2016JB012841

Gunnell, Y., & Burke, K. (2008). The African Erosion Surface: A Continental-Scale Synthesis of Geomorphology, Tectonics, and Environmental Change over the Past 180 Million Years. *Memoir of the Geological Society of America*, *201*, 1–66. doi: 10.1130/2008.1201

Gurnis, M., Mitrovica, J. X., Ritsema, J., & Van Heijst, H.-J. (2000). Constraining mantle density structure using geological evidence of surface uplift rates: The case of the African Superplume. *Geochemistry, Geophysics, Geosystems*, *1*(7), 1–35. doi: 10.1029/1999GC000035

Hager, B. H. (1984). Subducted Slabs and the Geoid: Constraints on Mantle Rheology and Flow. *Journal of Geophysical Research*, *89*(B7), 6003–6015.

Hager, B. H., & Clayton, R. W. (1989). Constraints on the Structure of Mantle Convection Using Seismic Observations, Flow Models, and the Geoid. In W. R. Peltier (Ed.), *Mantle convection: Plate tectonics and global dynamics* (pp. 657–763). New York: Gordon and Breach Science Publishers.

Hager, B. H., Clayton, R. W., Richards, M. A., Comer, R. P., & Dziewonski, A. M. (1985). Lower mantle heterogeneity, dynamic topography and the geoid. *Nature*, *313*, 541–545. doi: 10.1038/314752a0

Hager, B. H., & O'Connell, R. J. (1979). Kinematic Models of Large-Scale Flow in the Earth's Mantle. *Journal of Geophysical Research*, *84*(B3), 1031–1048.

Hager, B. H., & O'Connell, R. J. (1981). A Simple Global Model of Plate Dynamics and Mantle Convection. *Journal of Geophysical Research*, *86*(B6), 4843–4867. doi: 10.1029/JB086iB06p04843

Hazzard, J. A. N., Richards, F. D., Goes, S. D. B., & Roberts, G. G. (2022). Probabilistic Assessment of Antarctic Thermomechanical Structure: Impacts on Ice Sheet Stability. *EarthArXiv*. doi: 10.31223/X5C35R

Heister, T., Dannberg, J., Gassmöller, R., & Bangerth, W. (2017). High accuracy mantle convection simulation through modern numerical methods – II: realistic models and problems. *Geophysical Journal International*, *210*(2), 833–851. doi: 10.1093/gji/ggx195

Hoggard, M. J., Austermann, J., Randel, C., & Stephenson, S. (2021). Observational Estimates of Dynamic Topography Through Space and Time. In *Mantle convection and surface expressions* (pp. 371–411). AGU. doi: 10.1002/9781119528609.ch15

Hoggard, M. J., White, N., & Al-Attar, D. (2016). Global dynamic topography observations reveal limited influence of large-scale mantle flow. *Nature Geoscience*, *9*(May), 1–8. doi: 10.1038/ngeo2709

Holdt, M. C., White, N. J., Stephenson, S. N., & Conway-Jones, B. W. (2022). Densely Sampled Global Dynamic Topographic Observations and Their Signifi-

cance. *Journal of Geophysical Research: Solid Earth*, *127*, 1–32.

Jeans, J. H. (1923). The Propagation of Earthquake Waves. *Proceedings of the Royal Society of London A*, *102*(718), 554–574.

Kaula, W. M. (1963). Determination of the Earth's Gravitational Field. *Reviews of Geophysics*, *1*(4), 507–551.

Kramer, S. C., Davies, D. R., & Wilson, C. R. (2021). Analytical solutions for mantle flow in cylindrical and spherical shells. *Geoscientific Model Development*, *14*(4), 1899–1919. doi: 10.5194/gmd-14-1899-2021

Lambeck, K., Smither, C., & Johnston, P. (1998). Sea-level change, glacial rebound and mantle viscosity for northern Europe. *Geophysical Journal International*, *134*, 102–144. doi: 10.1046/j.1365-246X.1998.00541.x

Lau, H. C. P., Mitrovica, J. X., Davis, J. L., Tromp, J., Yang, H.-Y., & Al-Attar, D. (2017). Tidal tomography constrains Earth's deep-mantle buoyancy. *Nature*, *551*(7680), 321–326. doi: 10.1038/nature24452

Lees, M. E., Rudge, J. F., & McKenzie, D. (2020). Gravity, topography, and melt generation rates from simple 3D models of mantle convection. *Geochemistry, Geophysics, Geosystems*, *21*, 1–29. doi: 10.1029/2019gc008809

Lekić, V., & Fischer, K. M. (2014). Contrasting lithospheric signatures across the western United States revealed by Sp receiver functions. *Earth and Planetary Science Letters*, *402*, 90–98. doi: 10.1016/j.epsl.2013.11.026

Liu, L., & Gurnis, M. (2008). Simultaneous inversion of mantle properties and initial conditions using an adjoint of mantle convection. *Journal of Geophysical Research: Solid Earth*, *113*(B8), 1–17. doi: 10.1029/2008jb005594

Lu, C., Forte, A. M., Simmons, N. A., Grand, S. P., Kajan, M. N., Lai, H., & Garnero, E. J. (2020). The Sensitivity of Joint Inversions of Seismic and Geodynamic Data to Mantle Viscosity. *Geochemistry, Geophysics, Geosystems*, *21*(4), 1–29. doi: 10.1029/2019gc008648

McKenzie, D. (1977). Surface deformation, gravity anomalies and convection. *Geophysical Journal of the Royal Astronomical Society*, *48*, 211–238. doi: 10.1111/j.1365-246X.1977.tb01297.x

Merdith, A. S., Williams, S. E., Collins, A. S., Tetley, M. G., Mulder, J. A., Blades, M. L., ... Müller, R. D. (2021). Extending full-plate tectonic models into deep time: Linking the Neoproterozoic and the Phanerozoic. *Earth-Science Reviews*, *214*(103477), 1–44. doi: 10.1016/j.earscirev.2020.103477

Mitrovica, J. X., & Forte, A. M. (2004). A new inference of mantle viscosity based upon joint inversion of convection and glacial isostatic adjustment data. *Earth and Planetary Science Letters*, *225*(1-2), 177–189. doi: 10.1016/j.epsl.2004.06.005

Molnar, P., England, P. C., & Jones, C. H. (2015). Mantle dynamics, isostasy, and the support of high terrain. *Journal of Geophysical Research: Solid Earth*, *120*(3), 1932–1957. doi: 10.1002/2014JB011724

Morris, M., Fernandes, V. M., & Roberts, G. G. (2020). Extricating dynamic topography from subsidence patterns: Examples from Eastern North America's passive margin. *Earth and Planetary Science Letters*, *530*(115840), 1–13. doi: 10.1016/j.epsl.2019.115840

Moucha, R., & Forte, A. M. (2011). Changes in African topography driven by mantle convection: supplementary information. *Nature Geoscience*, *4*(10), 707–712. doi: 10.1038/ngeo1235

Moucha, R., Forte, A. M., Mitrovica, J. X., & Daradich, A. (2007). Lateral variations in mantle rheology: Implications for convection related surface observables and inferred viscosity models. *Geophysical Journal International*, *169*(1), 113–135. doi: 10.1111/j.1365-246X.2006.03225.x

Moucha, R., Forte, A. M., Mitrovica, J. X., Rowley, D. B., Quéré, S., Simmons, N. A., & Grand, S. P. (2008). Dynamic topography and long-term sea-level variations: There is no such thing as a stable continental platform. *Earth and*

Planetary Science Letters, *271*(1-4), 101–108. doi: 10.1016/j.epsl.2008.03.056

O'Connell, R. J. (1971). Pleistocene Glaciation and the Viscosity of the Lower Mantle. *Geophysical Journal of the Royal Astronomical Society*, *23*(3), 299–327. doi: 10.1111/j.1365-246X.1971.tb01823.x

O'Malley, C. P. B., White, N. J., Stephenson, S. N., & Roberts, G. G. (2021). Large-Scale Tectonic Forcing of the African Landscape. *Journal of Geophysical Research: Earth Surface*, *126*, 1–37. doi: 10.1029/2021jf006345

Panasyuk, S. V., Hager, B. H., & Forte, A. M. (1996). Understanding the effects of mantle compressibility on geoid kernels. *Geophysical Journal International*, *124*(1), 121–133. doi: 10.1111/j.1365-246X.1996.tb06357.x

Panton, J., Davies, J. H., & Myhill, R. (2023). The Stability of Dense Oceanic Crust Near the Core-Mantle Boundary. *Journal of Geophysical Research: Solid Earth*, *128*, 1–21. doi: 10.1029/2022JB025610

Parsons, B., & Daly, S. (1983). The relationship between surface topography, gravity anomalies and temperature structure of convection. *Journal of Geophysical Research*, *88*(B2), 1129–1144. doi: 10.1029/JB088iB02p01129

Pekeris, C. L. (1935). Thermal Convection in the Interior of the Earth. *Geophysical Supplements to the Monthly Notices of the Royal Astronomical Society*, *3*(8), 343–367.

Priestley, K., & McKenzie, D. (2013). The relationship between shear wave velocity, temperature, attenuation and viscosity in the shallow part of the mantle. *Earth and Planetary Science Letters*, *381*, 78–91. doi: 10.1016/j.epsl.2013.08.022

Ribe, N. M. (2007). Analytical Approaches to Mantle Dynamics. *Treatise on Geophysics*, *7*, 167–226. doi: 10.1016/B978-044452748-6.00117-6

Ricard, Y. (2007). Physics of Mantle Convection. *Treatise on Geophysics*, *7*, 31–88.

Ricard, Y. (2015). Physics of Mantle Convection. In G. Schubert (Ed.), *Treatise on geophysics* (pp. 23–71). doi: 10.1016/B978-044452748-6.00115-2

Richards, F. D., Hoggard, M. J., Ghelichkhan, S., Koelemeijer, P., & Lau, H. C. P. (2021). Geodynamic, geodetic, and seismic constraints favour deflated and dense-cored LLVPs. *EarthArXiv*, 1–20. doi: 10.31223/X55601

Richards, F. D., Hoggard, M. J., Ghelichkhan, S., Koelemeijer, P., & Lau, H. C. P. (2023). Geodynamic, geodetic, and seismic constraints favour deflated and dense-cored LLVPs. *Earth and Planetary Science Letters*, *602*(117964), 1–13. doi: 10.1016/j.epsl.2022.117964

Richards, F. D., Hoggard, M. J., White, N., & Ghelichkhan, S. (2020). Quantifying the relationship between short-wavelength dynamic topography and thermomechanical structure of the upper mantle using calibrated parameterization of anelasticity. *Journal of Geophysical Research: Solid Earth*, *125*, 1–36. doi: 10.1029/2019JB019062

Richards, M. A., & Hager, B. H. (1984). Geoid Anomalies in a Dynamic Earth. *Journal of Geophysical Research*, *89*(B7), 5987–6002. doi: 10.1029/JB089iB07p05987

Salles, T., Flament, N., & Müller, D. (2017, jan). Influence of mantle flow on the drainage of eastern Australia since the Jurassic Period. *Geochemistry, Geophysics, Geosystems*, *18*(1), 280–305. doi: 10.1002/2016GC006617

Spasojevic, S., & Gurnis, M. (2012). Sea level and vertical motion of continents from dynamic earth models since the Late Cretaceous. *AAPG Bulletin*, *96*(11), 2037–2064. doi: 10.1306/03261211121

Stanley, J. R., Braun, J., Baby, G., Guillocheau, F., Robin, C., Flowers, R. M., ... Beucher, R. (2021). Constraining Plateau Uplift in Southern Africa by Combining Thermochronology, Sediment Flux, Topography, and Landscape Evolution Modeling. *Journal of Geophysical Research: Solid Earth*, *126*, 1–34. doi: 10.1029/2020JB021243

Steinberger, B. (2007). Effects of latent heat release at phase boundaries on flow in

the Earth's mantle, phase boundary topography and dynamic topography at the Earth's surface. *Physics of the Earth and Planetary Interiors*, *164*(1-2), 2–20. doi: 10.1016/j.pepi.2007.04.021

Steinberger, B. (2016). Topography caused by mantle density variations: Observation-based estimates and models derived from tomography and lithosphere thickness. *Geophysical Journal International*, *205*(1), 604–621. doi: 10.1093/gji/ggw040

Steinberger, B., & Antretter, M. (2006). Conduit diameter and buoyant rising speed of mantle plumes: Implications for the motion of hot spots and shape of plume conduits. *Geochemistry, Geophysics, Geosystems*, *7*(11), 1–25. doi: 10.1029/2006GC001409

Steinberger, B., & Calderwood, A. R. (2006). Models of large-scale viscous flow in the Earth's mantle with constraints from mineral physics and surface observations. *Geophysical Journal International*, *167*(3), 1461–1481. doi: 10.1111/j.1365-246X.2006.03131.x

Steinberger, B., Nelson, P. L., Grand, S. P., & Wang, W. (2019). Yellowstone plume conduit tilt caused by large-scale mantle flow. *Geochemistry, Geophysics, Geosystems*, *20*, 5896–5912. doi: 10.1029/2019gc008490

Stephenson, S. N., White, N. J., Carter, A., Seward, D., Ball, P. W., & Klöcking, M. (2021). Cenozoic Dynamic Topography of Madagascar. *Geochemistry, Geophysics, Geosystems*, *22*, 1–38. doi: 10.1029/2020gc009624

Tackley, P. J., Stevenson, D. J., Glatzmaier, G. A., & Schubert, G. (1993). Effects of an endothermic phase transition at 670 km depth on spherical mantle convection. *Nature*, *361*, 699–704. doi: 10.1038/361699a0

Thoraval, C., Machete, P., & Cazenave, A. (1994). Influence of mantle compressibility and ocean warping on dynamical models of the geoid. *Geophysical Journal International*, *117*, 566–573. doi: 10.1111/j.1365-246X.1994.tb03954.x

Thoraval, C., & Richards, M. A. (1997). The geoid constraint in global geodynamics: Viscosity structure, mantle heterogeneity models and boundary conditions. *Geophysical Journal International*, *131*, 1–8. doi: 10.1111/j.1365-246X.1997.tb00591.x

Topographic asymmetry of the south atlantic from global models of mantle flow and lithospheric stretching. (2014). *Earth and Planetary Science Letters*, *387*, 107-119. doi: 10.1016/j.epsl.2013.11.017

Turcotte, D. L., & Schubert, G. (2002). *Geodynamics* (Second Edi ed.). Cambridge University Press.

Wang, Y., Liu, L., & Zhou, Q. (2022). Topography and gravity reveal denser cratonic lithospheric mantle than previously thought. *Geophysical Research Letters*, *49*(1). doi: https://doi.org/10.1029/2021GL096844

Wieczorek, M. A., & Meschede, M. (2018). SHTools: Tools for Working with Spherical Harmonics. *Geochemistry, Geophysics, Geosystems*, *19*, 1–19. doi: 10.1029/2018GC007529

Zhong, S., Gurnis, M., & Hulbert, G. (1993). Accurate determination of surface normal stress in viscous flow from a consistent boundary flux method. *Physics of the Earth and Planetary Interiors*, *78*, 1–8. doi: 10.1016/0031-9201(93)90078-N

Zhong, S., McNamara, A., Tan, E., Moresi, L., & Gurnis, M. (2008). A benchmark study on mantle convection in a 3-D spherical shell using CitcomS. *Geochemistry, Geophysics, Geosystems*, *9*(10), 1–32. doi: 10.1029/2008GC002048

Zhong, S., Zuber, M. T., Moresi, L., & Gurnis, M. (2000). Role of temperature-dependent viscosity and surface plates in spherical shell models of mantle convection. *Journal of Geophysical Research*, *105*(B5), 11063–11082.

Zhou, Q., & Liu, L. (2019). Topographic evolution of the western United States since the early Miocene. *Earth and Planetary Science Letters*, *514*, 1–12. doi: 10.1016/j.epsl.2019.02.029

1157 Zhou, Q., Liu, L., & Hu, J. (2018). Western US volcanism due to intruding oceanic
1158 mantle driven by ancient Farallon slabs. *Nature Geoscience*, *11*, 70–76. doi: 10
1159 .1038/s41561-017-0035-y

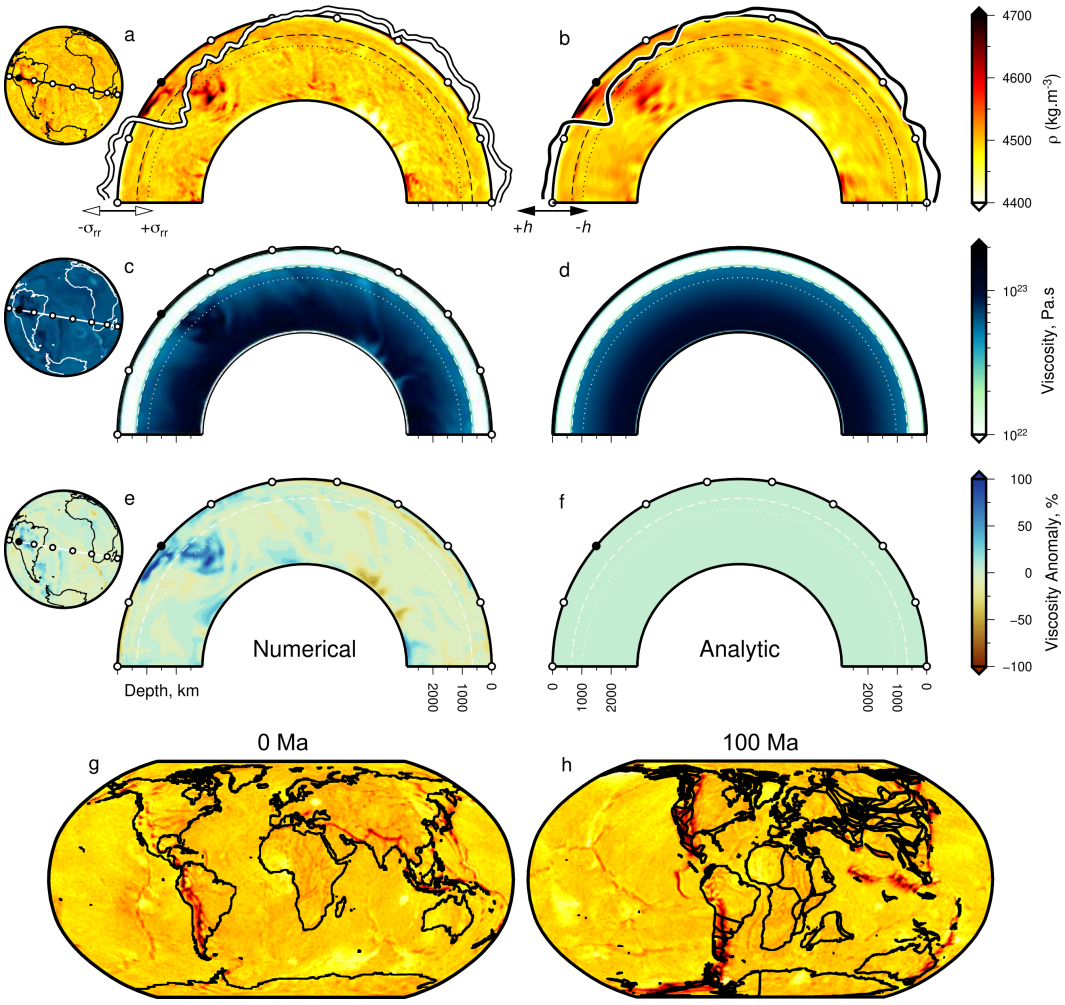

Figure 1. Examples of mantle densities and viscosity used to calculate stresses and surface deflections numerically and analytically. (a) Great-circle slice (180°) through full-resolution, present-day, density ρ, predicted by numeric model TERRA with temperature dependent viscosity (Model 11a; see Table 1 and body text); see globe to left for location. White circles = 20° intervals; filled black circle indicates orientation of cross section; dashed line = 660 km depth contour; dotted line = 1038 km depth contour, at which depth ρ is plotted on globe; white-black curve = numeric prediction of surface normal stress σ_{rr} from Model 11a. (b) As (a) but slice is through spherical harmonic expansion of density structure, to maximum degree $l = 50$ ($\lambda \approx 792$ km; Model 11b); black-white curve = surface deflection h, calculated using (analytic) propagator matrix approach (Model 12). (c) As (a) but for slice through full-resolution viscosity structure of numeric model. (d) As (c) but for mean (radial) viscosity structure, used along with the density structure shown in (b) to generate analytic solution for surface deflection shown by black-white curve atop (b). (e–f) As (c–d) but viscosity is expressed as a percentage anomaly with respect to the layer (radial) mean. (g–h) Predicted densities at 270 km depth at 0 and 100 Ma from numeric model with viscosity independent of temperature (Model 1a). Extended results are shown in Figure S1. Plate motions and paleo-coastlines are from Merdith et al. (2021).

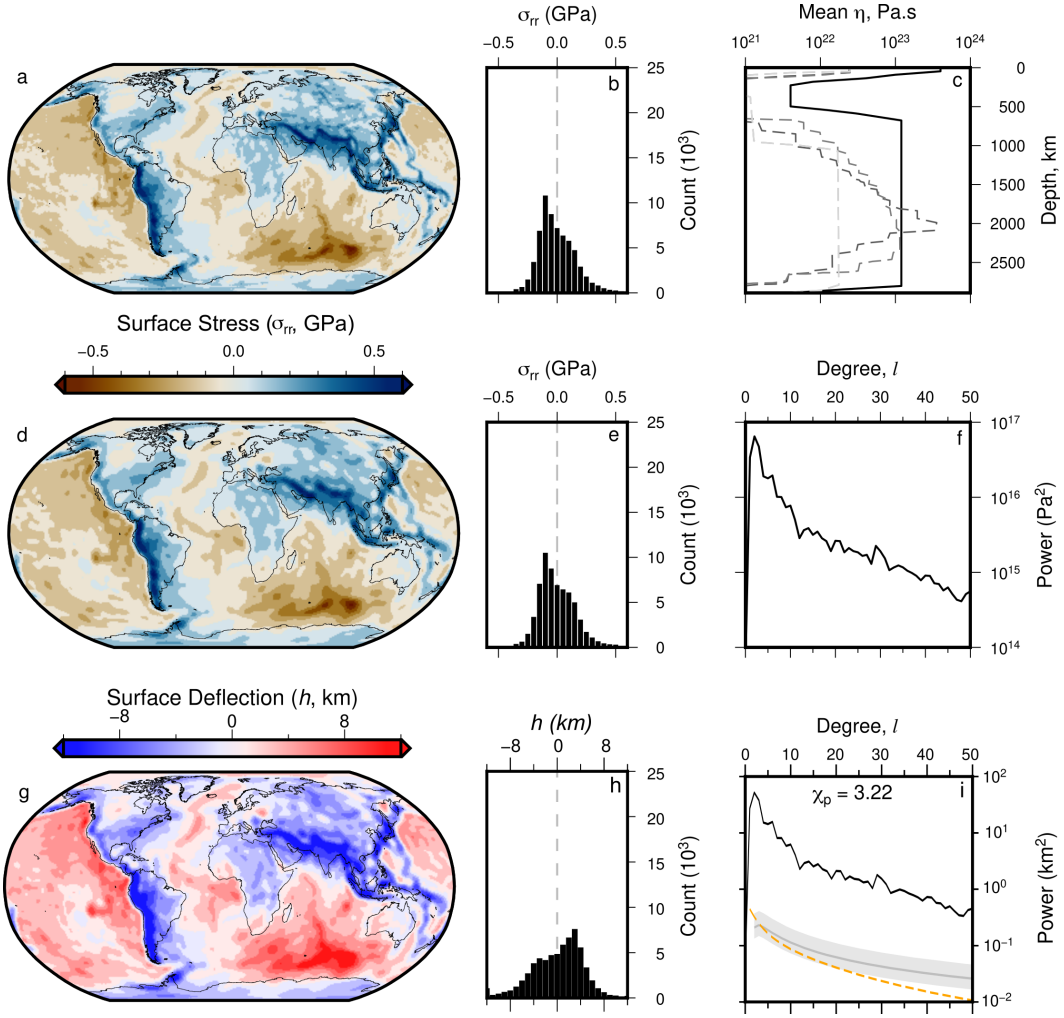

Figure 2. Surface stresses and deflections from numeric simulation of mantle convection with spherical harmonic expansion up to degree 50. (a) Predicted present-day surface radial stress, σ_{rr} (Model 1a). (b) Histogram of values shown in (a). (c) Black line = radial viscosity structure used to drive Model 1a and thus produce grid shown in panel (a). Gray dashed lines = alternative viscosity profiles of (from darkest to lightest) Mitrovica and Forte (2004), Steinberger and Calderwood (2006), and μ_1, μ_2 from Ghelichkhan et al. (2021). (d) Model 1b: Spherical harmonic fit to Model 1a (panel a) up to maximum degree $l = 50$ (minimum wavelength $\lambda \approx 792$ km). (e) Histogram of values shown in panel (d). (f) Power spectrum—total power per degree—of stress field shown in panel (d). (g) Spherical harmonic fit to surface deflections (Model 1b; up to degree $l = 50$). (h) Histogram of values shown in panel (g). (i) Black curve = power spectrum of calculated water-loaded surface deflections (panel g); gray line and band = expected dynamic topography from Kaula's rule using admittance $Z = 12 \pm 3$ mGal km^{-1} (Kaula, 1963). Orange dashed line = expected power spectrum for water-loaded residual topography (from Holdt et al., 2022) via analytic solution of special case of Equation 15. χ_p = root-mean-squared difference between calculated (black) and independent (orange & grey) surface deflection power (see Equation 20). All histograms are weighted by latitude to correct to equal-area. Figure S2 shows extended results including air-loaded deflections.

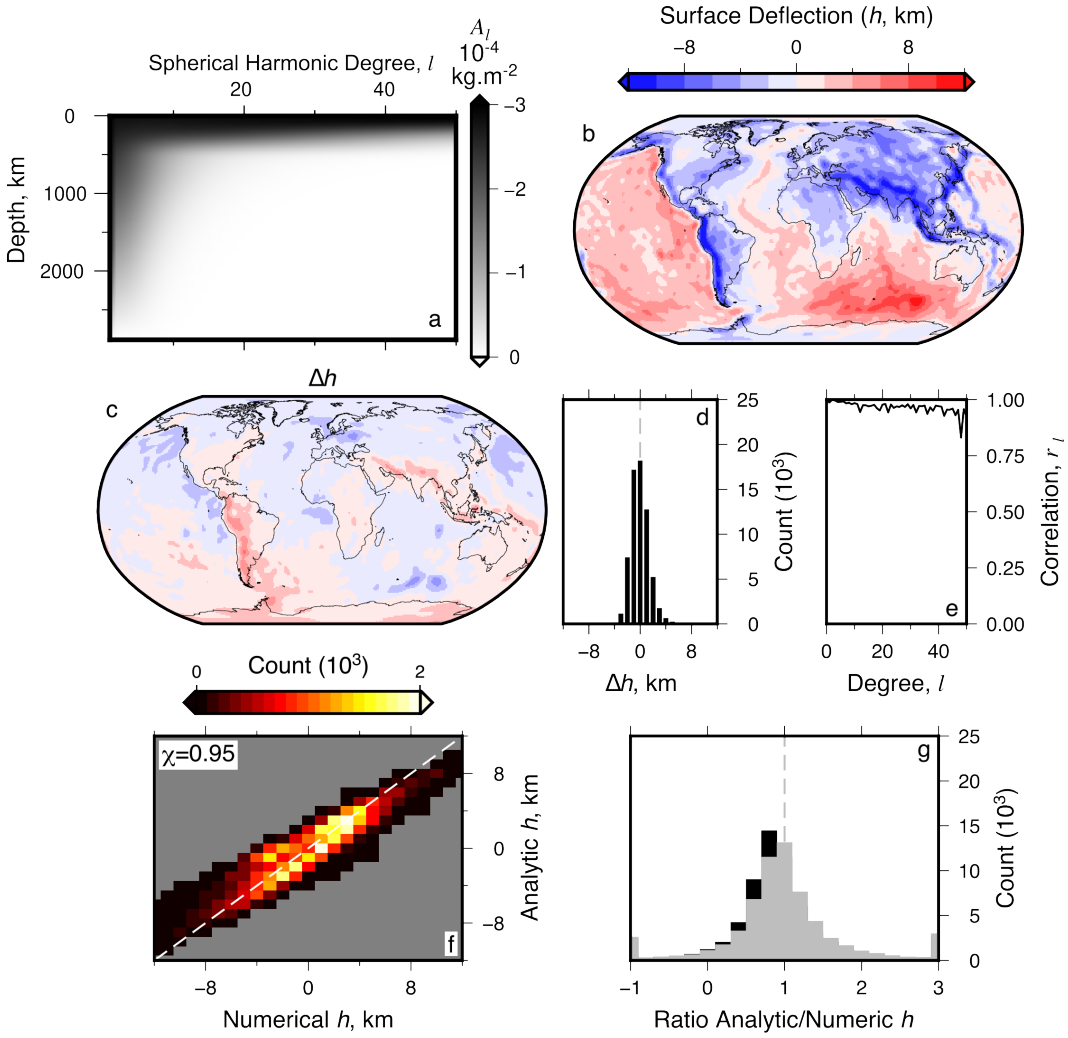

Figure 3. Comparisons of numeric (Model 1b) and analytic (Model 2) estimation of surface deflections from models with identical parameterization. (a) Surface deflection sensitivity kernel A_l as a function of spherical harmonic degree, l, and depth (Model 2). (b) Propagator matrix (analytic) solution for water-loaded surface deflection calculated using sensitivity kernel shown in panel (a). Figure S3 shows extended results including power spectra and air-loaded deflections. (c) Difference, Δh, of surface deflections in Models 1b and 2. (d) Histogram of difference values shown in (c). (e) Spectral correlation coefficient, r_l, between Models 1b and 2; Equation 8. (f) Comparison of predicted surface deflections; χ = root-mean-squared difference between predictions (Equation 7); gray dashed line = 1:1 ratio. (g) Black bars = histogram of ratios between analytic:numeric solutions for surface deflection as in (f). Gray dashed line = 1 (i.e., identical values). Gray bars = as black bars, but for propagator matrix solution amplitudes scaled up by optimal factor to fit numeric solution (=10%). All histograms are weighted by latitude to correct to equal-area.

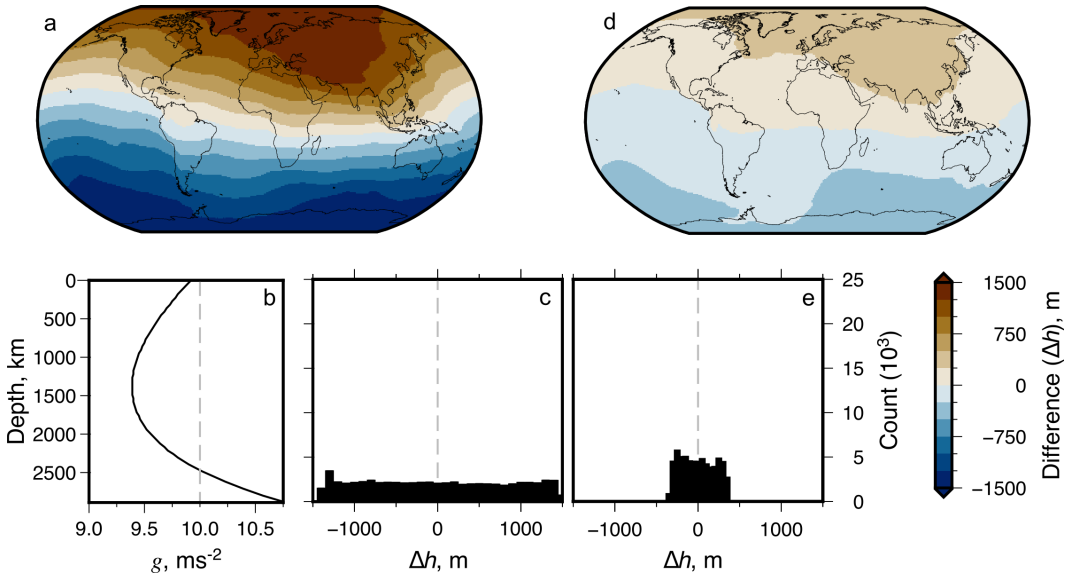

Figure 4. Impact of self-gravitation (a–c) and gravitational potential of deflected surfaces (d–e) on surface deflections calculated analytically. In these tests surface deflections from models with different gravity parameterizations are compared to predictions from Model 2. (a) Difference between water-loaded surface deflections calculated using the propagator matrix technique incorporating self-gravitation (Model 3; black curve in panel b) and g = 10 m s^{-2} (dashed line in panel b; Model 2). (c) Histogram of values in panel (a). (d–e) Differences in surface deflection from models with (Model 4) and without (Model 2) stress perturbations induced by gravitational potential of the deflected surface. All histograms are weighted by latitude to correct to equal-area, they show the full extent of the results. Figures S4–S5 show extended results including maps of calculated surface deflections.

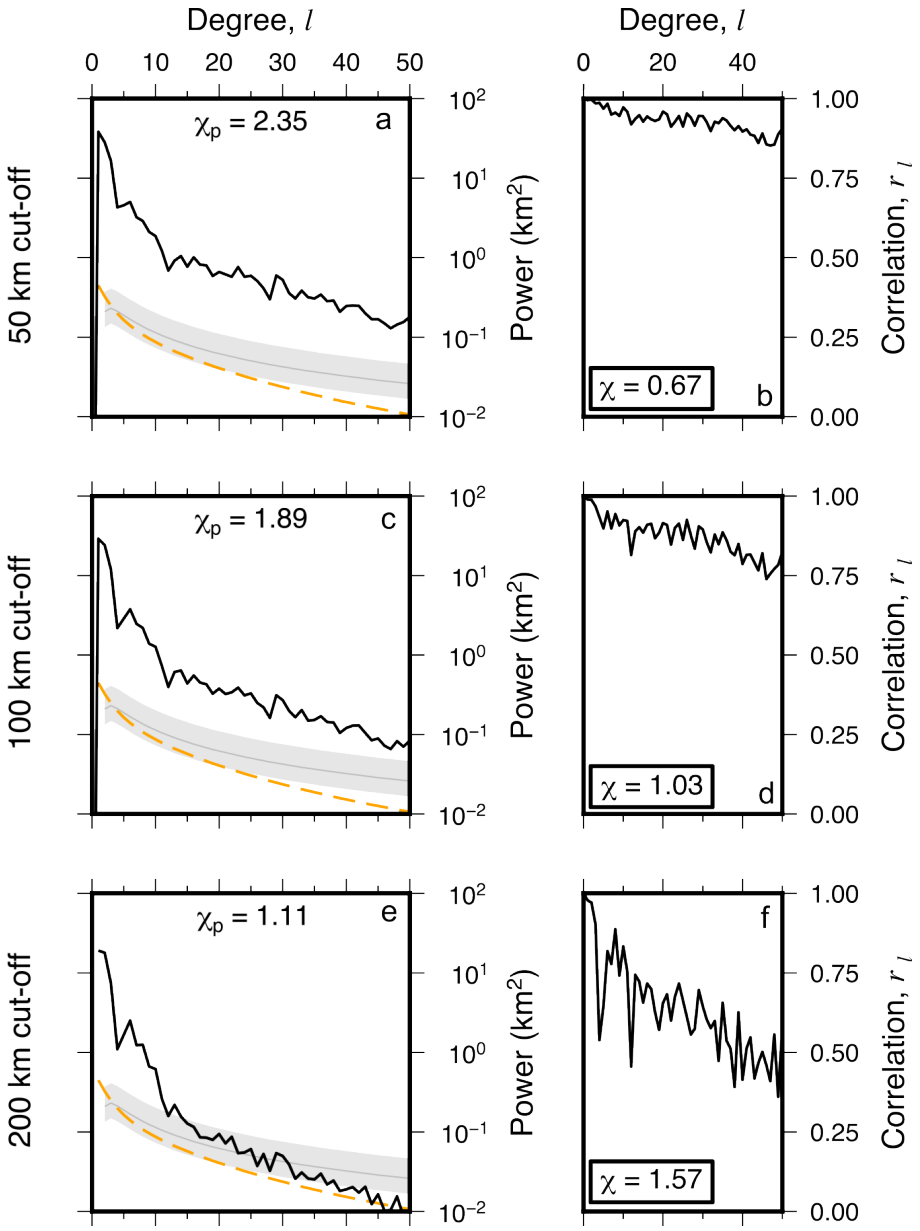

Figure 5. Effect of removing shallow structure on surface deflections calculated analytically. Surface deflections in models with shallow structure removed are compared to those predicted by Model 2. (a) Black line = Power spectra of predicted water-loaded surface deflection from propagator matrix solution for Model 2 (Figure 3b), but with effect of upper 50 km of density anomaly structure ignored in calculation (Model 5). Gray line and band = expected dynamic topography from Kaula's rule using admittance $Z = 12 \pm 3$ mGal km^{-1} (Kaula, 1963). Orange dashed line = expected power spectrum for water-loaded residual topography from Holdt et al. (2022), via analytic solution of special case of Equation 15. χ_p = root-mean-squared difference between calculated (black) and independent (orange & grey) surface deflection power (see Equation 20). (b) Spectral correlation coefficient, r_l, of surface deflections in Models 5 and 2 (see Equation 19). Inset χ = root-mean-squared difference in surface deflections of Models 5 and 2 (see Equation 18). (c–d) and (e–f) as (a–b) but for depth cut-offs of 100 (Model 6) and 200 km (Model 7), respectively. Figure S7 show extended results including maps of calculated surface deflections and differences with Model 2.

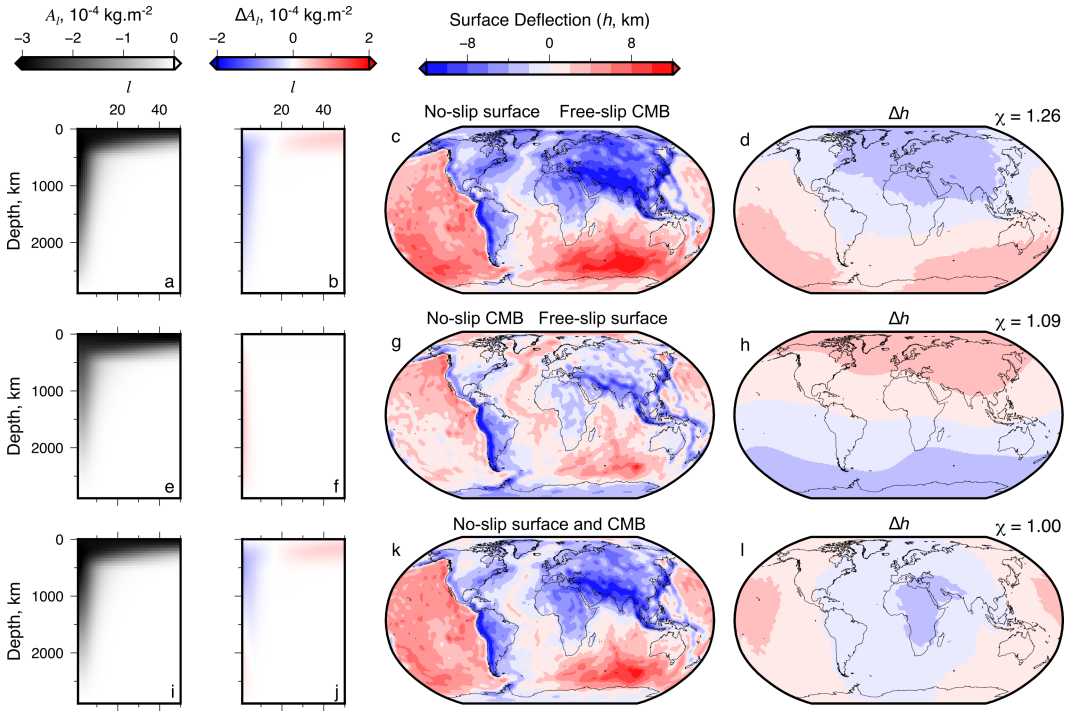

Figure 6. Impact of free- and no-slip surface and core-mantle boundary boundary conditions on surface deflections. This figure shows comparisons of surface deflections from models with different assumed boundary conditions and Model 2. (a) Water-loaded surface deflection sensitivity kernel A_l, for Model 8, which has a no-slip surface boundary condition, but otherwise is parameterised the same as Model 2. (b) Sensitivity kernel of Model 8 minus sensitivity kernel of Model 2. Note, positive difference implies reduced sensitivity compared to Model 2, and vice versa, since A_l is negative. (c) Predicted water-loaded surface deflection for Model 8. (d) Difference between surface deflection predictions for Model 8 and Model 2. (e–h) as (a–d) but for Model 9: free-slip surface boundary, no-slip CMB. (i–l) as (a–d) but for Model 10: no-slip surface and CMB boundaries.

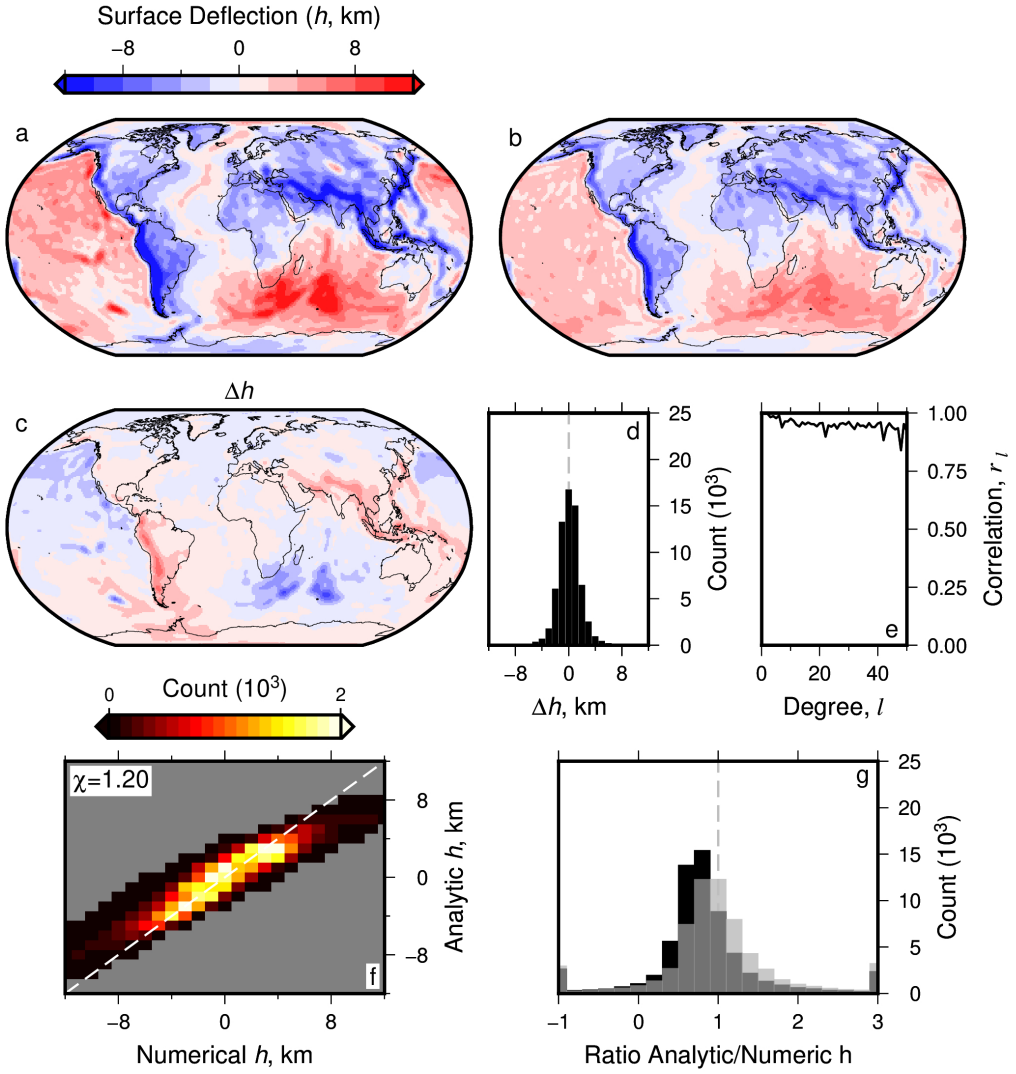

Figure 7. Comparison of surface deflections calculated numerically (Model 11b) and analytically (Model 12) using results from simulation with temperature dependent viscosity. (a) Model 11b: Spherical harmonic expansion of predicted present-day water-loaded surface deflection converted from stress output from numeric model TERRA (Model 11a), to maximum degree $l = 50$. (b) Model 12: As (a) but for prediction made using propagator matrix method. (c) Difference, Δh, between Models 11b and 12 (panels a and b). (d) Histogram of difference values shown in (c), weighted by latitude to correct to equal-area. (e) Spectral correlation coefficient, r_l, between predictions shown in panels (a) and (b); Equation 8. (f) Numeric (Model 11b) versus analytic (Model 12) predictions of surface deflection; χ = root-mean-squared difference between predictions, Equation 7; gray dashed line = 1:1 ratio. (g) Histogram of ratios between analytic:numeric solutions for surface deflection as in (f), weighted by latitude. Gray dashed line = 1 (i.e., identical values). Gray bars = as black bars, but for propagator matrix solution amplitudes scaled up by optimal factor to fit numeric solution (24%).

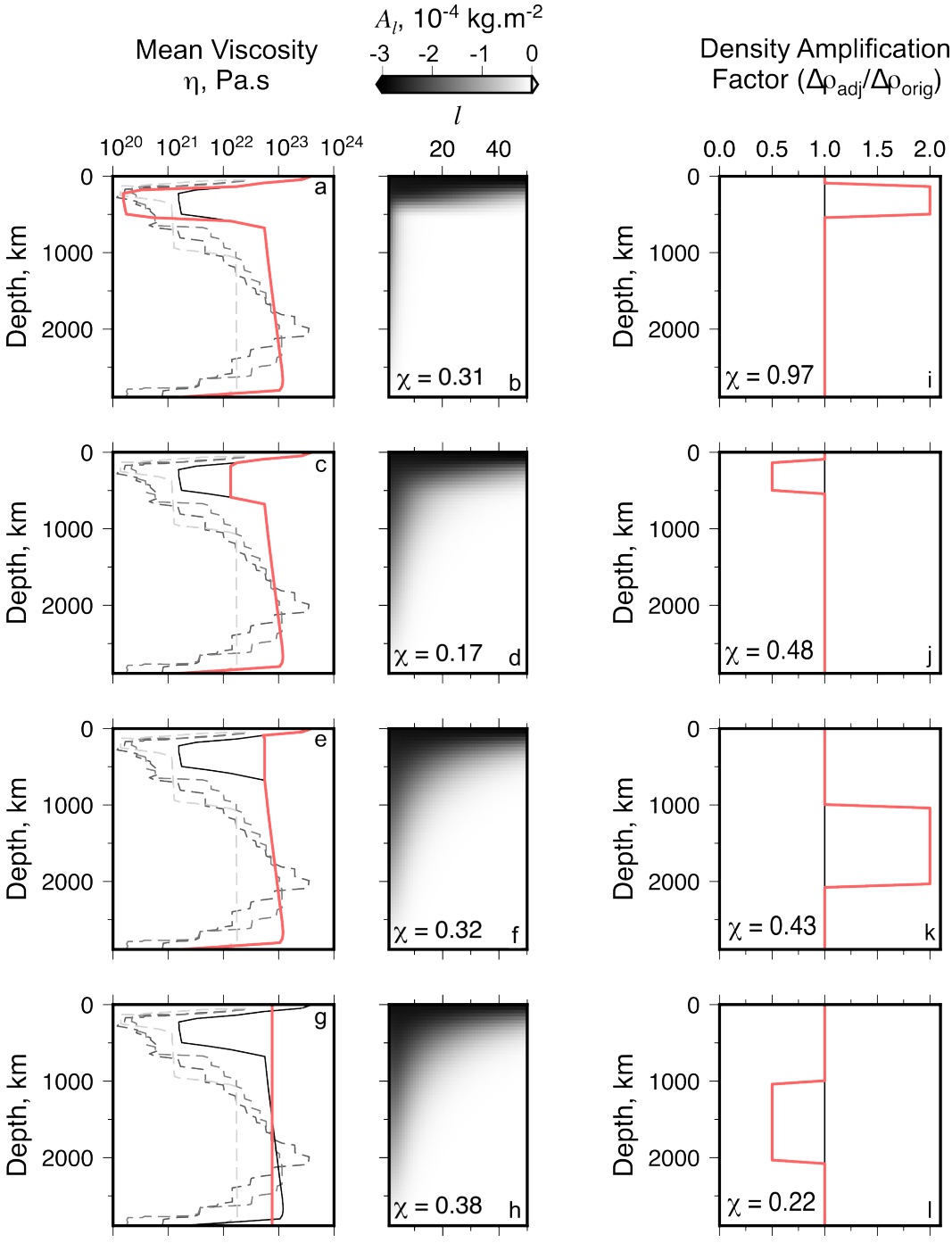
Mean Viscosity
η, Pa.s
A_l, 10^{-4} kg.m^{-2}
-3 -2 -1 0
l
Density Amplification
Factor ($\Delta\rho_{adj}/\Delta\rho_{orig}$)
10^{20} 10^{21} 10^{22} 10^{23} 10^{24}
20 40
0.0 0.5 1.0 1.5 2.0
Depth, km
0
1000
2000
a
b
χ = 0.31
c
d
χ = 0.17
e
f
χ = 0.32
g
h
χ = 0.38
i
χ = 0.97
j
χ = 0.48
k
χ = 0.43
l
χ = 0.22

Figure 8. Sensitivity of calculated analytic surface deflection to adjusted radial viscosity (a–h) and density anomalies (i–l). This figure shows comparisons of surface deflections calculated in models with modified viscosity and density to the results from Model 12 (see Table 1). (a) Black curve = unadjusted prediction of present-day radial mean viscosity from Model 11; red line = adjusted radial profile with viscosity decreased by a factor of 10 between depths of $\sim$ 300–500 km (Model 13); gray dashed lines = viscosity profiles used in other studies (see Figure 2). (b) Sensitivity kernel for the viscosity profile indicated by the red curve in panel a. Value of root-mean-squared difference, χ, between calculated surface deflections for unadjusted and adjusted viscosity is stated (see Equation 7). (c–h) Results from testing alternative radial viscosity (Models 14–16). Figure S13 shows extended results including maps of surface deflections and their differences. (i-l) Density anomalies (red line) adjusted by directly scaling spherical harmonic coefficients ($l > 0$) up or down by a factor of 2 (Models 17 & 19: panels e & g) or $\frac{1}{2}$ (Models 18 & 20: f & h). Viscosity structure applied in each case is same as that used to generate Figure 7b. Sensitivity kernels for surface deflections are not shown since they are invariant with respect to density anomalies, $\Delta\rho$, depending only on viscosity structure. Figure S14 shows extended results including maps of surface deflections and their differences.

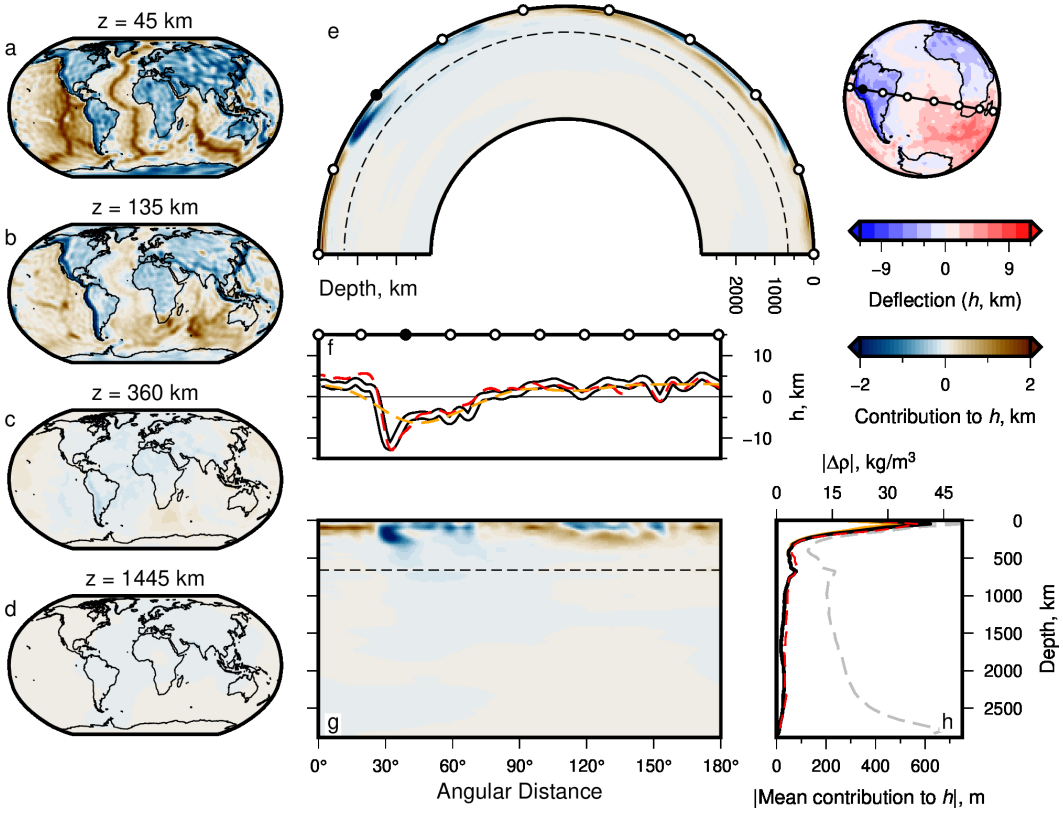

Figure 9. Effective density; contributions from density anomalies to surface deflection. (a–d) Maps of net contribution to present-day water-loaded surface deflection calculated using propagator matrix approach (Model 12; see body text for details). Depth slices at 45, 135, 360 and 1445 km depth incorporating all spherical harmonic degrees l and orders m, up to l = 50. (e) Great-circle slice (180°) showing contributions to surface deflection; globe to right shows transect location and calculated surface deflection (Model 12). White circles = 20° intervals; note filled black circle for orientation; dashed line = 660 km depth contour. (f) White-black curve = total surface deflection along transect shown atop globe in panel (e); abscissa aligned with panel g; orange dashed line = same but for maximum l = 10 (see Supporting Information Figure S18); red dashed curve = surface deflection from Model 2. (g) Cartesian version of panel (e); ordinate aligned with panel (h). (h) Grey dashed curve = mean absolute value of density anomalies in Model 12—see top axis for values. Black curve = global mean amplitude (modulus) of contribution from density structure in Model 12 to total surface deflection h, across all l and m; orange line = same but for maximum l = 10; red dashed line = results for Model 2 (see Section 6.3). See Figures S15–S19 for extended results, demonstrating sensitivity of surface deflections to maximum spherical harmonic degree.

Supporting Information for "Reconciling Surface Deflections From Simulations of Global Mantle Convection"

Conor P. B. O'Malley[1,2], Gareth G. Roberts[1], James Panton[3], Fred D. Richards[1], J. Huw Davies[3], Victoria M. Fernandes[1,4], Siavash Ghelichkhan[5]

[1]Department of Earth Science & Engineering, Imperial College London, London SW7 2BP, UK

[2]now at Cathie Group, 2-4 Hanover Square, Newcastle upon Tyne NE1 3NP, UK

[3]School of Earth & Environmental Sciences, University of Cardiff, Park Place, Cardiff CF10 3AT, UK

[4]now at Section 4.6 Geomorphology, GFZ Potsdam, Telegrafenberg, 14473 Potsdam, Germany

[5]Research School of Earth Sciences, Australian National University, 142 Mills Road, Acton, ACT 0200, Australia

Contents of this file

1. Equations of motion and description of numerical approach to solving them.
2. Table summarising model parameters.
3. Summary of spherical harmonic expansion used to estimate surface deflections.
4. Figures S1 to S19.

Corresponding authors: C. P. O'Malley or G. G. Roberts, Department of Earth Science & Engineering, Imperial College London, London SW7 2BP, UK. (c_omalley1@msn.com or gareth.roberts@imperial.ac.uk)

1. Introduction

This Supporting Information document includes an extended description of the equations of motion solved to predict mantle convection. It summarises the numeric approach adopted to solve them using the TERRA code, the spherical harmonic expansion and model parameters. The approaches used to calculate surface deflections are included with the main manuscript.

This document also includes nineteen figures in three groups. First, Figures S1–S2 summarise the setup of the numerical simulations, and show examples of results and resultant surface deflections. They expand upon the results shown in Figures 1–2 in the main manuscript. Secondly, Figures S3–S7 show surface deflections and sensitivity kernels calculated by solving the equations of motion analytically using the propagator matrix approach and associated statistics. They show results for models that include self-consistent radial gravitation and removal of shallow structure, expanding upon the results shown in Figures 3–5 in the main manuscript. Figures S8–S14 show calculated vertical surface deflections from models in which viscosity and density are modified. These figures includes comparisons of surface deflections calculated using the different approaches (numeric and analytic) and model parametrizations. They extend the results shown in Figures 7–8 in the main manuscript. Figures S15–S19 show effective contributions from density anomalies in the mantle to instantaneous surface deflections. In the main text, we show spherical harmonic solutions up to a maximum spherical harmonic degree $l = 50$ (see Figure 9). Here, results are presented for maximum degrees 40, 30, 20, 10 and 5. The

results demonstrate the importance of contributions from short wavelength (high degree) density structure to surface deflections, especially at shallow depths.

2. Equations Governing Predicted Mantle Convection

In the main manuscript we explore how calculated surface deflections are impacted by the choice of methodology and assumptions used in solving equations of motion for mantle convection. This section expands on the numeric approach used to solve the equations. The analytic approach is discussed in the main manuscript.

Theoretical predictions of surface displacements from mantle convection arise from the application of physical laws that take the form of conservation equations for mass, momentum and energy (see, e.g., Hager & O'Connell, 1981; Parsons & Daly, 1983). Here, we solve those equations across a 3D spherical domain using the finite element code TERRA (Baumgardner, 1985; Bunge & Baumgardner, 1995, etc.). Under this formulation, theoretical convection in an incompressible fluid can be expressed by the following three dimensionless equations (e.g., Baumgardner, 1985; Davies et al., 2013; McKenzie et al., 1974; Parsons & Daly, 1983). First, the continuity condition for conservation of mass,

$$\nabla \cdot \mathbf{u} = 0, \tag{1}$$

where $\mathbf{u}$ is the fluid velocity vector. Since the Prandtl number is likely to always be extremely large in this system—mantle viscosity is expected to be many orders of mag-

nitude larger than the product of density and thermal diffusivity—inertial terms can be neglected (e.g., Parsons & Daly, 1983). Second, the equation of motion,

$$\nabla\sigma = -\rho'\mathbf{g}, \tag{2}$$

where

$$\rho' = -\alpha\rho_0(T - T_{\text{ref}}). \tag{3}$$

σ is the 3×3 stress tensor where the (radial) hydrostatic component balancing the reference density structure has been subtracted, ρ' is the density difference due to temperature, α is the coefficient of thermal expansion, T is temperature, T_{ref} is a radially varying reference temperature structure, which has a constant value in the mid-mantle and joins to a cold thermal boundary layer near the surface and a hot one at the CMB, reaching the surface, T_s, and core mantle boundary, T_{CMB} temperatures at the respective boundaries, and $\mathbf{g}$ is gravitational acceleration acting radially (see Table S1). This stress tensor σ_{ij} is decomposed into deviatoric and lithostatic components:

$$\sigma_{ij} = \tau_{ij} - p\delta_{ij}, \tag{4}$$

where τ_{ij} is the deviatoric stress tensor, p is dynamic pressure and δ_{ij} is the Kronecker delta function. The deviatoric stress tensor and the strain-rate tensor, $\dot{\epsilon}_{ij}$, are related by:

$$\tau_{ij} = 2\eta\dot{\epsilon}_{ij} = \eta\left(\frac{\partial\mathbf{u}_i}{\partial x_j} + \frac{\partial\mathbf{u}_j}{\partial x_i}\right), \tag{5}$$

where η is viscosity, and $\partial/\partial x_i$ is the spatial partial derivative. By combining equations 2, 4 and 5 we solve the equation of motion:

$$\frac{\partial(\eta\epsilon_{ij})}{\partial x_j} - \frac{\partial p}{\partial x_i} = -\rho' g \delta_{ir}, \tag{6}$$

where g is the scalar value of $\mathbf{g}$ and δ_{ir} is the Kronecker delta selecting the radial direction r.

We first examine predictions from models in which viscosity varies only with depth, i.e., $\eta = \eta_0 \times \eta_r$, where η_0 is reference viscosity (see Table S1), and η_r is a scaling factor dependent only on radius, plotted with model results as appropriate throughout this manuscript. We then include temperature dependence of viscosity, i.e., $\eta = \eta_0 \times \eta_r \times \eta_T$, where

$$\eta_T = \exp(z' - 2T'). \tag{7}$$

Dimensionless depth, $z' = z/d$, where $d = z_{\text{surface}} - z_{\text{CMB}} = 2890$ km, and dimensionless temperature $T' = (T - T_s)/(T_{\text{CMB}} - T_s)$, where $T_{\text{CMB}} - T_s = 2700$ K.

Finally, the heat transport equation is solved to ensure conservation of energy:

$$\frac{\partial T}{\partial t} + \mathbf{u} \cdot \nabla T = \kappa \nabla^2 T + \frac{H}{C_p}, \tag{8}$$

where κ is thermal diffusivity, H is internal heat generation and C_p is specific heat capacity. See Table S1 for parameter values and units. Heat generation within the mantle depends on the distribution of radiogenic isotopes (e.g., Ricard, 2015). Concentrations of such

elements can be tracked in TERRA, using particles, varying as a consequence of flow and melting (see, e.g., Panton et al., 2023; van Heck et al., 2016, for full explanation). The bulk composition field, C, which varies between 0 and 1, is also tracked on particles and calculated for each of the finite elements in the model. The end-members represent completely depleted/harzburgitic material ($C = 0$), and fully enriched/basaltic material ($C = 1$). As a result, radiogenic heat production across the whole mantle volume varies, being ≈ 24 TW (5.8×10^{-12} W kg^{-1}) at 1.2 Ga, and ~ 18 TW (4.5×10^{-12} W kg^{-1}) by 0 Ma. Simulations are initialised such that the average mantle composition is $C = 0.20$ (Panton et al., 2023), and composition obeys the conservation equation:

$$\frac{\partial C}{\partial t} = -\nabla \cdot (C\mathbf{u}). \tag{9}$$

2.1. Numerical Modelling Strategy

The Stokes equations described above are solved by the finite element method on a series of stacked spherical shells composed of nodes based on a subdivision of a regular icosahedron, with an identical geometry for each shell when projected onto the CMB (see, e.g., Figure 1 of Baumgardner, 1985). The radial spacing of consecutive shells is 45 km, which is the same as the mean horizontal spacing of the elements across the entire model domain. The stacking of identically partitioned shells leads to a finer mean horizontal resolution of ≈ 33 km at the CMB, and a coarser resolution of ≈ 60 km at the surface. The surfaces of the uppermost elements in the shallowest shell lie at zero depth. To enable estimates of stress from these models to be directly compared with analytical solutions obtained from Green's functions across layer boundaries, the predicted

values of deviatoric stress were calculated using the calculated velocities from the nearest shells using the interpolating linear shape functions of the underlying finite elements, while the dynamic pressure is calculated directly at the surface (see the main manuscript).

Each numerical model presented in this paper has two computational stages: 'spin-up', which is used to initialize the model, and the geologically more realistic 'main' stage, from which we generate predictions of surface deflections. The spin-up stage includes 2.2 billion years of model run-time. It has the following conditions imposed to avoid sharp velocity and temperature gradients, and sudden reorganization of mantle flow when the main model starts. First, a free-slip condition is imposed at the surface. Second, an initial, random white noise temperature field generated with power across spherical harmonic degrees 1-19, is inserted. Mean mantle temperature is initially 2000 K. Mantle convection arises naturally over the first two billion years of model run-time. A fixed-slip surface velocity condition is then applied to the surface for 200 Ma. These velocities are set to be equal to those at 1 Ga extracted from the reconstructions of Merdith et al. (2021); the vertical component of slip is zero. The resultant mantle structure is used as the initial condition for the main model.

The main model routine predicts flow from 1 Ga to the present-day (0 Ma). It includes an isothermal condition imposed at the surface, $T_s = 300$ K. A fixed-slip condition is imposed such that the vertical component of $\mathbf{u}$ is zero. Horizontal slip is prescribed using the plate reconstructions of Merdith et al. (2021); these are applied in 1 Ma long stages. As such, stirring by plate drift and slab sinking play a role in driving mantle flow in these

models. An isothermal condition is also imposed at the core-mantle boundary such that $T_{\mathrm{CMB}} = 3000$ K. A free-slip velocity boundary condition is imposed there, so the radial component of the mantle flow velocity $(\mathbf{u_r}) = 0$. While this radial velocity boundary condition is of the Dirichlet type, in a free-slip boundary condition no tangential restriction is imposed on the flow velocity but rather on the tangential deviatoric stresses acting on the boundary ($\tau_{r\theta}$, $\tau_{r\phi}$ where r, θ and ϕ are the radial and two tangential directions respectively), which are zero. Horizontal components of slip are allowed to naturally emerge and evolve subject to lowermost mantle flow. Plume behaviour is not artificially suppressed or instigated.

To ensure numerical stability and computational accuracy in these simulations, the reference viscosity, η_0, is set to 4×10^{21} Pa s. This value is probably an order of magnitude greater than the viscosity of the actual upper mantle (e.g., Forte, 2007; Ghelichkhan et al., 2021; Mitrovica & Forte, 2004, and references therein). Consequently, flow velocities in the simulations are likely to be significantly slower than in actuality. An obvious cause for concern is that using actual (comparatively fast) plate velocities as surface boundary conditions atop a relatively slowly convecting 'mantle' is likely to induce unrealistic flow. To address this issue, imposed plate velocities are scaled such that the root-mean squared (RMS) values of the actual applied velocities (≈ 5 cm yr^{-1} unscaled) match RMS values of surface velocities (≈ 2.5 cm yr^{-1}) calculated during the spin-up phase (before plate velocities are imposed on the model) when the model mantle is convecting naturally and not being driven by surface velocities. The applied surface plate velocities are therefore scaled by a factor of 0.5 (i.e., 2.5/5) in the simulations examined in this study. To ensure

that volumetric fluxes through ridges and subduction zones are realistic, simulation run times are increased by a factor of 2; i.e., the 1 Myr long plate stages are run for twice their elapsed time (2 Myr), but at half the speed. All times stated throughout the rest of this manuscript refer to times re-scaled for real-world comparison; i.e., the actual age of the respective plate stage.

For the reference case (Model 1), these conditions lead to the density distributions shown in Figure S1. Surface layer density anomalies occur only as a result of predicted compositional variation, since the surface temperature, T_s, is constant globally. This model represents the first of two reference numerical models examined in this contribution. It has the radial viscosity structure shown in Figure 2c of the main manuscript. Later, in the main manuscript, we investigate a second numerical model incorporating temperature-dependent viscosity (Equation 7). In the main manuscript we describe numeric and analytic approaches that use output from these models to calculate instantaneous surface deflections. Both approaches make use of spherical harmonics.

3. Spherical Harmonics

Any real, square-integrable function over the surface of the Earth can be described as a function of longitude θ and latitude ϕ by a linear combination of spherical harmonics of degree l and order m,

$$f(\theta,\phi) = \sum_{l=1}^{L} \sum_{m=-l}^{l} f_{lm} Y_{lm}(\theta,\phi). \tag{10}$$

The spherical harmonic functions Y_{lm} are the natural orthogonal set of basis functions on the sphere, and f_{lm} are the spherical harmonic coefficients. As an example, Figure 2d

in the main manuscript shows spherical harmonic expansion of the surface stress field predicted by Model 1 at 0 Ma (cf. Figure 2a in the main manuscript). We call this result Model 1b, and the original, full-resolution numerical result is referred to as Model 1a. The fidelity of the spherical harmonic expansion is demonstrated by the similarity of the maps and histograms shown in panels a–b and d–e of Figure 2 in the main manuscript.

$$P_l = \sum_{m=-l}^{l} f_{lm}^2 \tag{11}$$

gives the total power across all spherical harmonics of a given degree l. Average power for each mode m within degree l, $\hat{P}_l = P_l/(2l+1)$, since there are $2l+1$ modes (orders) per degree—we do not explore this definition of power in this contribution, and present only total power per degree (see, e.g., Hoggard et al., 2016; Holdt et al., 2022).

References

Baumgardner, J. R. (1985). Three-dimensional treatment of convective flow in the earth's mantle. *Journal of Statistical Physics*, *39*(5-6), 501–511. doi: 10.1007/BF01008348

Bunge, H.-P., & Baumgardner, J. R. (1995). Mantle convection modeling on parallel virtual machines. *Computers in Physics*, *9*(2), 207–215. doi: 10.1063/1.168525

Davies, D. R., Davies, J. H., Bollada, P. C., Hassan, O., Morgan, K., & Nithiarasu, P. (2013). A hierarchical mesh refinement technique for global 3-D spherical mantle convection modelling. *Geoscientific Model Development*, *6*(4), 1095–1107. doi: 10.5194/gmd-6-1095-2013

Forte, A. M. (2007). Constraints on Seismic Models from Other Disciplines - Implications for Mantle Dynamics and Composition. In B. Romanowicz & A. Dziewonski (Eds.), *Seismology and the structure of the earth* (pp. 805–858). Elsevier B.V. doi: 10.1016/B978-044452748-6.00027-4

Ghelichkhan, S., Bunge, H.-P., & Oeser, J. (2021). Global mantle flow retrodictions for the early Cenozoic using an adjoint method: Evolving dynamic topographies, deep mantle structures, flow trajectories and sublithospheric stresses. *Geophysical Journal International*, *226*(2), 1432–1460. doi: 10.1093/gji/ggab108

Hager, B. H., & O'Connell, R. J. (1981). A Simple Global Model of Plate Dynamics and Mantle Convection. *Journal of Geophysical Research*, *86*(B6), 4843–4867. doi: 10.1029/JB086iB06p04843

Hoggard, M. J., White, N., & Al-Attar, D. (2016). Global dynamic topography observations reveal limited influence of large-scale mantle flow. *Nature Geoscience*, *9*(May), 1–8. doi: 10.1038/ngeo2709

Holdt, M. C., White, N. J., Stephenson, S. N., & Conway-Jones, B. W. (2022). Densely Sampled Global Dynamic Topographic Observations and Their Significance. *Journal of Geophysical Research: Solid Earth*, *127*, 1–32.

McKenzie, D. P., Roberts, J. M., & Weiss, N. O. (1974). Convection in the earth's mantle: Towards a numerical simulation. *Journal of Fluid Mechanics*, *62*(3), 465–538. doi: 10.1017/S0022112074000784

Merdith, A. S., Williams, S. E., Collins, A. S., Tetley, M. G., Mulder, J. A., Blades, M. L., ... Müller, R. D. (2021). Extending full-plate tectonic models into deep time: Linking the Neoproterozoic and the Phanerozoic. *Earth-Science Reviews*, *214*(103477), 1–44. doi: 10.1016/j.earscirev.2020.103477

Mitrovica, J. X., & Forte, A. M. (2004). A new inference of mantle viscosity based upon joint inversion of convection and glacial isostatic adjustment data. *Earth and Planetary Science Letters*, *225*(1-2), 177–189. doi: 10.1016/j.epsl.2004.06.005

Panton, J., Davies, J. H., & Myhill, R. (2023). The Stability of Dense Oceanic Crust Near the Core-Mantle Boundary. *Journal of Geophysical Research: Solid Earth*, *128*, 1–21. doi: 10.1029/2022JB025610

Parsons, B., & Daly, S. (1983). The relationship between surface topography, gravity anomalies and temperature structure of convection. *Journal of Geophysical Research*, *88*(B2), 1129–1144. doi: 10.1029/JB088iB02p01129

Ricard, Y. (2015). Physics of Mantle Convection. In G. Schubert (Ed.), *Treatise on geophysics* (pp. 23–71). doi: 10.1016/B978-044452748-6.00115-2

van Heck, H. J., Davies, J. H., Elliott, T., & Porcelli, D. (2016). Global-scale modelling of melting and isotopic evolution of Earth's mantle: Melting modules for TERRA.

218 *Geoscientific Model Development*, *9*, 1399–1411. doi: 10.5194/gmd-9-1399-2016

Table S1. Summary of Model Parameters.

Parameter	Symbol	Value	Units
Surface temperature	T_s	300	K
Core-mantle boundary temperature	T_{CMB}	3000	K
Internal heating rate	H	See text.	W kg^{-1}
Thermal expansivity	α	2.5×10^{-5}	K^{-1}
Thermal conductivity	K	4	W m^{-1}K^{-1}
Thermal diffusivity	κ	8.08×10^{-7}	m^{2}s^{-1}
Specific heat capacity	C_p	1100	J kg^{-1}K^{-1}
Reference viscosity	η_0	4×10^{21}	Pa s
Reference density	ρ_0	4500	kg m^{-3}
Overlying fluid density	ρ_w	1 or 1030	kg m^{-3}

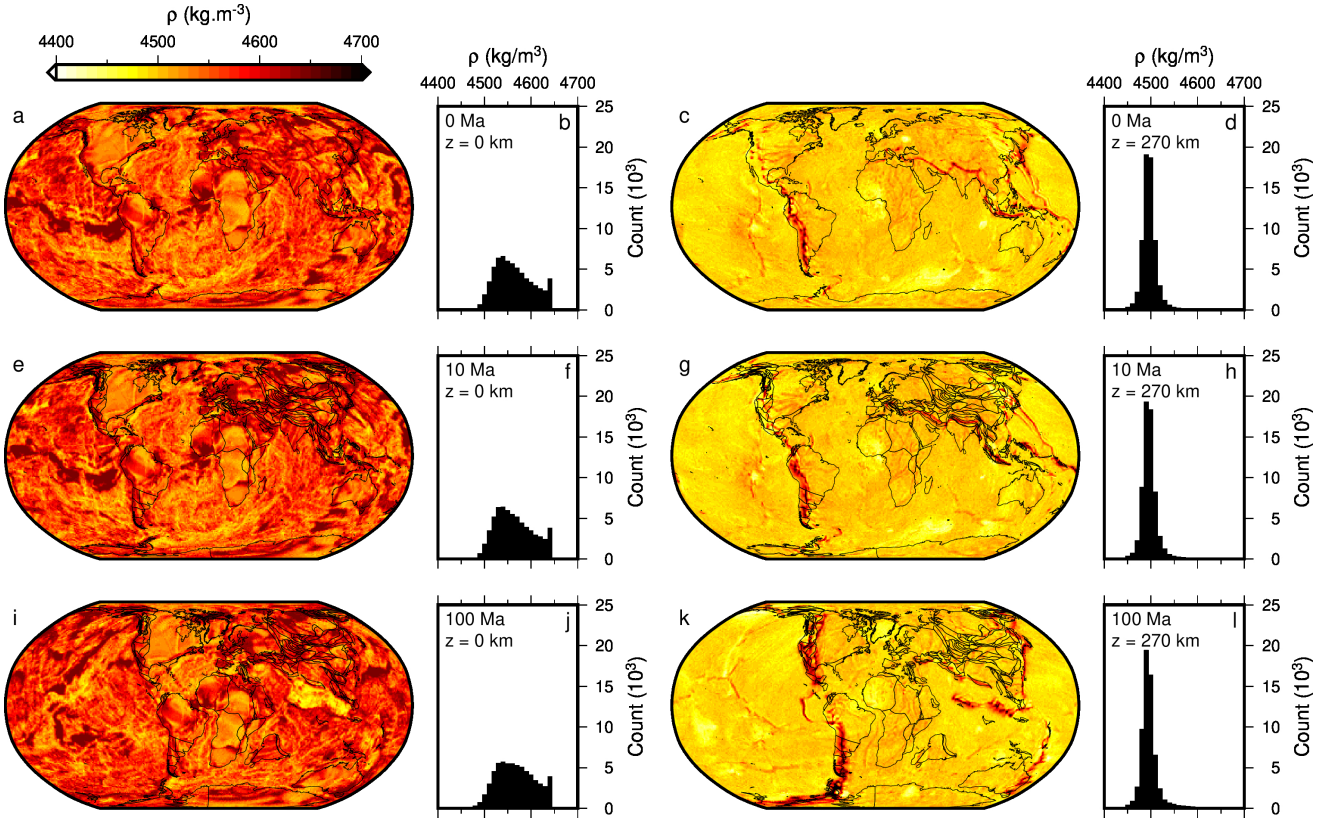

Figure S1. Model 1: Densities predicted from numerical simulation of mantle convection. (a) Predicted present-day density ρ, at surface (z=0), from TERRA model with viscosity independent of temperature (Model 1a), plotted at grid resolution of 1 degree. (b) Histogram of values shown in (a), weighted by latitude to correct to equal-area. (c–d) As (a–b) but for densities at a depth of 270 km. (e–h) As (a–d) but for time slice at 10 Ma; paleo-coastlines generated from Phanerozoic plate rotation history of Merdith et al. (2021). (i–l) As (a–d) but for time slice at 100 Ma.

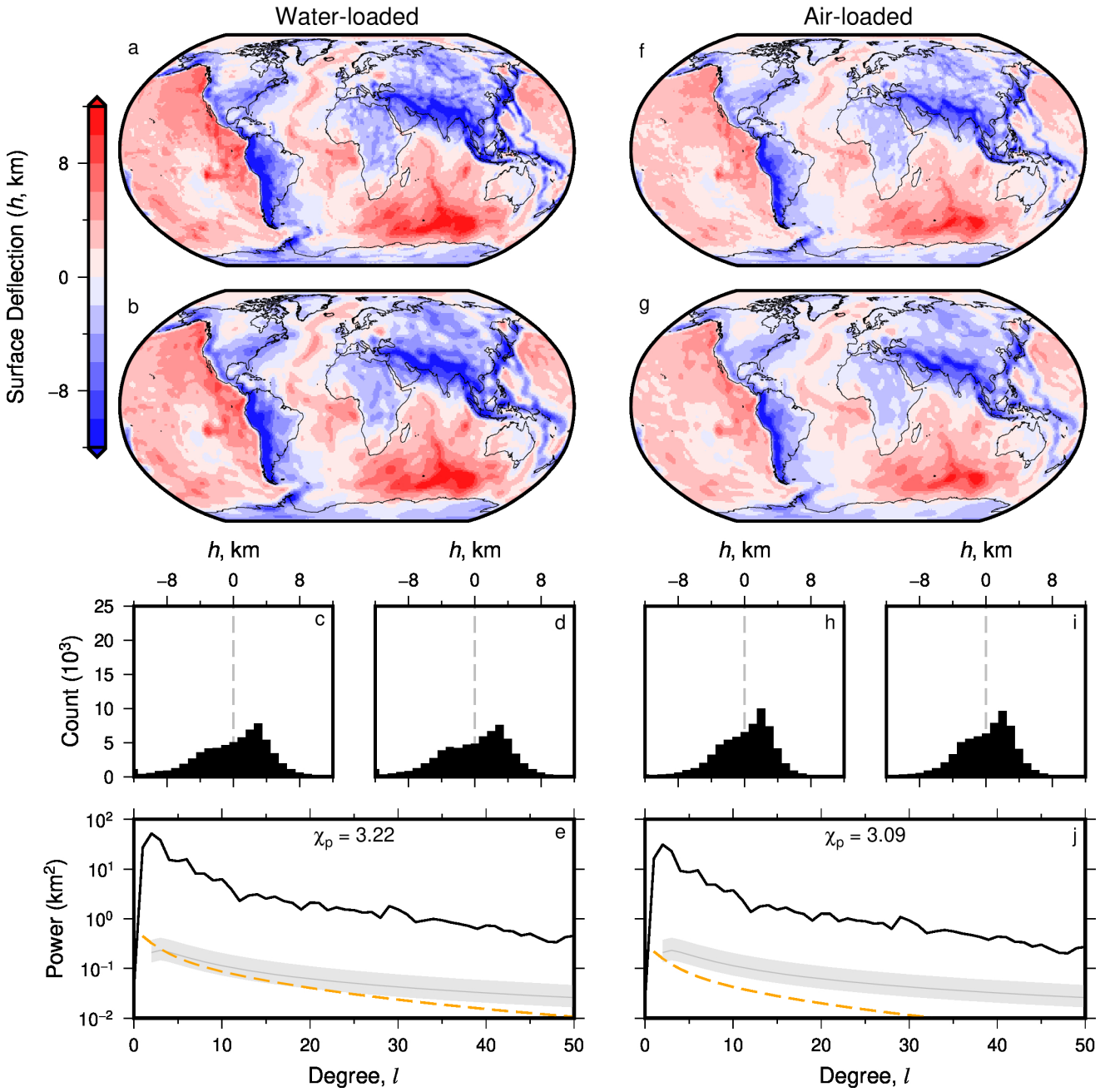
Water-loaded
Air-loaded
a
b
c
d
e
f
g
h
i
j
Surface Deflection (h, km)
8
0
−8
h, km
−8
0
8
Count (10³)
25
20
15
10
5
0
Power (km²)
10²
10¹
10⁰
10⁻¹
10⁻²
χp = 3.22
χp = 3.09
0
10
20
30
40
50
Degree, l

Figure S2. Model 1: Predicted water- and air-loaded surface deflections. (a) Water-loaded, present day, surface deflection predicted by Model 1a. Figure S2a shows normal stress, σ, used with Equation 2 in the main manuscript to calculate surface deflections, h; $\rho_w = 1030$ kg m^{-3}. (b) Spherical harmonic fit (Model 1b) up to degree $l = 50$ of grid shown in (a), calculated using the approach of Hoggard et al. (2016). (c–d) Histogram of values shown in (a) and (b) respectively, weighted by latitude to correct to equal-area. (e) Black line = power spectrum in terms of total power per degree, from spherical harmonic expansion shown in (b); gray line and band = expected dynamic topography from Kaula's rule using admittance $Z = 12 \pm 3$ mGal km^{-1} (Kaula, 1963). Orange dashed line = expected power spectrum for water-loaded residual topography from Holdt et al. (2022) via analytical solution of special case of Equation 4 of the main manuscript. χ_p = total root-mean-squared difference between distribution of modeled and theoretical surface deflection power (see Equation 9 in the main manuscript). (f–j) As (a–e) but for air-loaded surface deflection; $\rho_w = 1$ kg m^{-3}.

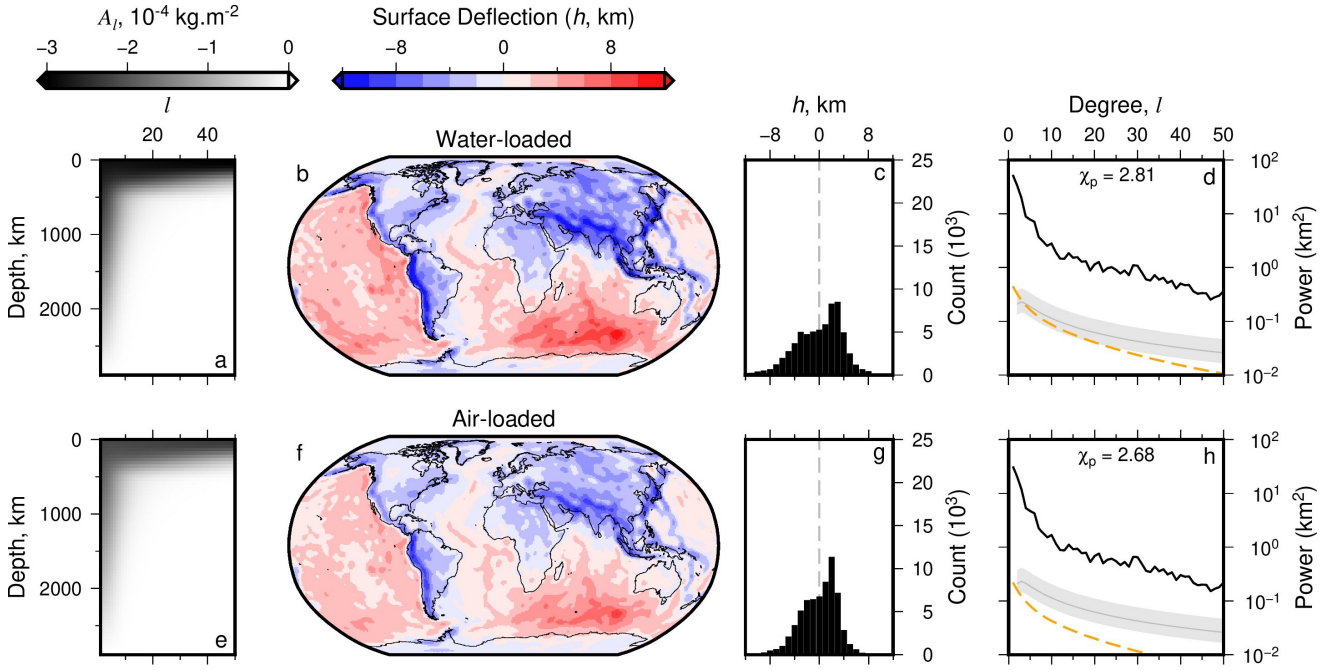
A_l, 10^{-4} kg.m^{-2}
−3 −2 −1 0
Surface Deflection (h, km)
−8 0 8
l
20 40
Depth, km
0 1000 2000
a
Water-loaded
b
h, km
−8 0 8
c
Count (10^3)
0 5 10 15 20 25
Degree, l
0 10 20 30 40 50
χ_p = 2.81
d
Power (km^2)
10^2 10^1 10^0 10^{-1} 10^{-2}
e
Air-loaded
f
g
χ_p = 2.68
h

Figure S3. Model 2: Propagator matrix solution for surface deflection with associated sensitivity kernels. (a) Surface deflection sensitivity kernel A_l, as a function of spherical harmonic degree, l, and depth, calculated for the radial viscosity structure (and other parameters) which were used to generate Model 1; see Equation 5 in the main manuscript. (b) Present-day predicted water-loaded surface deflection, calculated using propagator matrix method, from spherical harmonic expansion (to maximum degree $l = 50$) of density structure (e.g., Figure S1) and radial viscosity structure (e.g., Figure 2c; Corrieu et al., 1995; Hager et al., 1985; Parsons & Daly, 1983). Note that for comparison with numeric calculations shown in Figure 3, no terms related to flow-related perturbation of gravitational potential terms are included (see Equations 5 and 6 in the main manuscript), and gravitational acceleration $g = 10$ m s^{-2} everywhere. (c) Histogram of values shown in (b), weighted by latitude to correct to equal-area. (d) Black line = power spectrum in terms of total power per degree, from surface deflection prediction shown in (a); gray line and band = expected dynamic topography from Kaula's rule using admittance $Z = 12 \pm 3$ mGal km^{-1} (Kaula, 1963). Orange dashed line = power spectrum of water-loaded residual topography from Holdt et al. (2022), via analytical solution of special case of Equation 4 in the main manuscript. χ_p = total root-mean-squared difference between distribution of modeled and theoretical surface deflection power (see Equation 9 in the main manuscript). (e–h) As (a–d) but for air-loaded surface deflection; $\rho_w = 1$ kg m^{-3}.

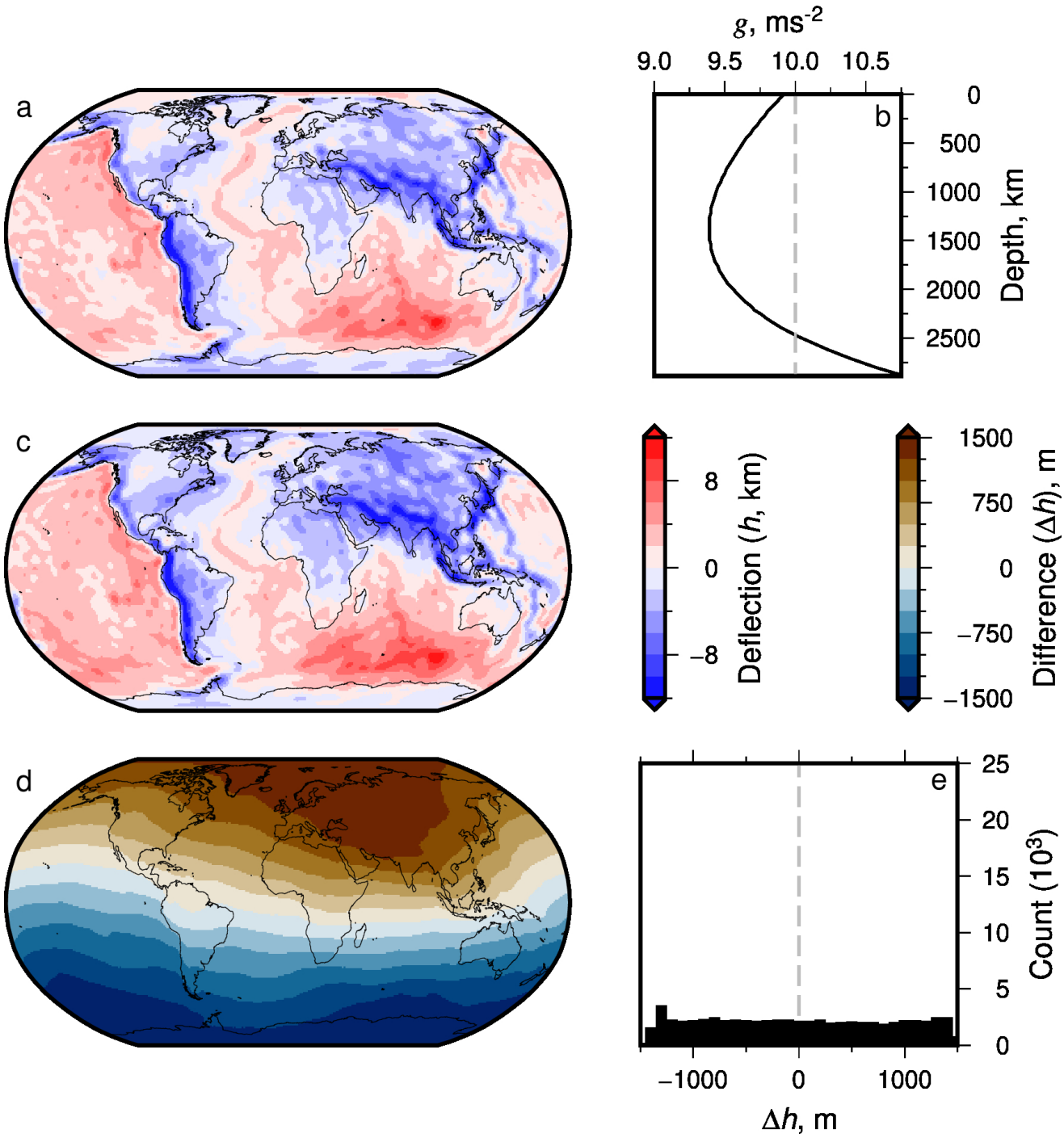
a
b
c
d
e
g, ms^{-2}
9.0
9.5
10.0
10.5
0
500
1000
1500
2000
2500
Depth, km
8
0
−8
Deflection (h, km)
1500
750
0
−750
−1500
Difference (Δh), m
25
20
15
10
5
0
Count (10^3)
−1000
0
1000
Δh, m

Figure S4. Model 3: Predicted surface deflection from mantle convection in presence of radial gravitation. (a) Predicted present-day water-loaded surface deflection calculated using propagator matrix method, incorporating radial gravitation i.e., $g(r)$, black curve in (b).(b) Black curve = profile of gravitational acceleration as a function of radius, given density distribution predicted by Model 1a; gray dashed line = constant value of $g = 10$ m s^{-2} used within TERRA model runs and in previous figures. (c) As (a) but calculated using $g = 10$ m s^{-2} everywhere, i.e., same as Figure S3a–d (see dashed line in panel b). Associated sensitivity kernels are shown in Figure S6. (d) Difference between surface deflections predicted by Models 3 and 2 (panels a and c). (e) Histogram of values in (d), weighted by latitude to correct to equal-area.

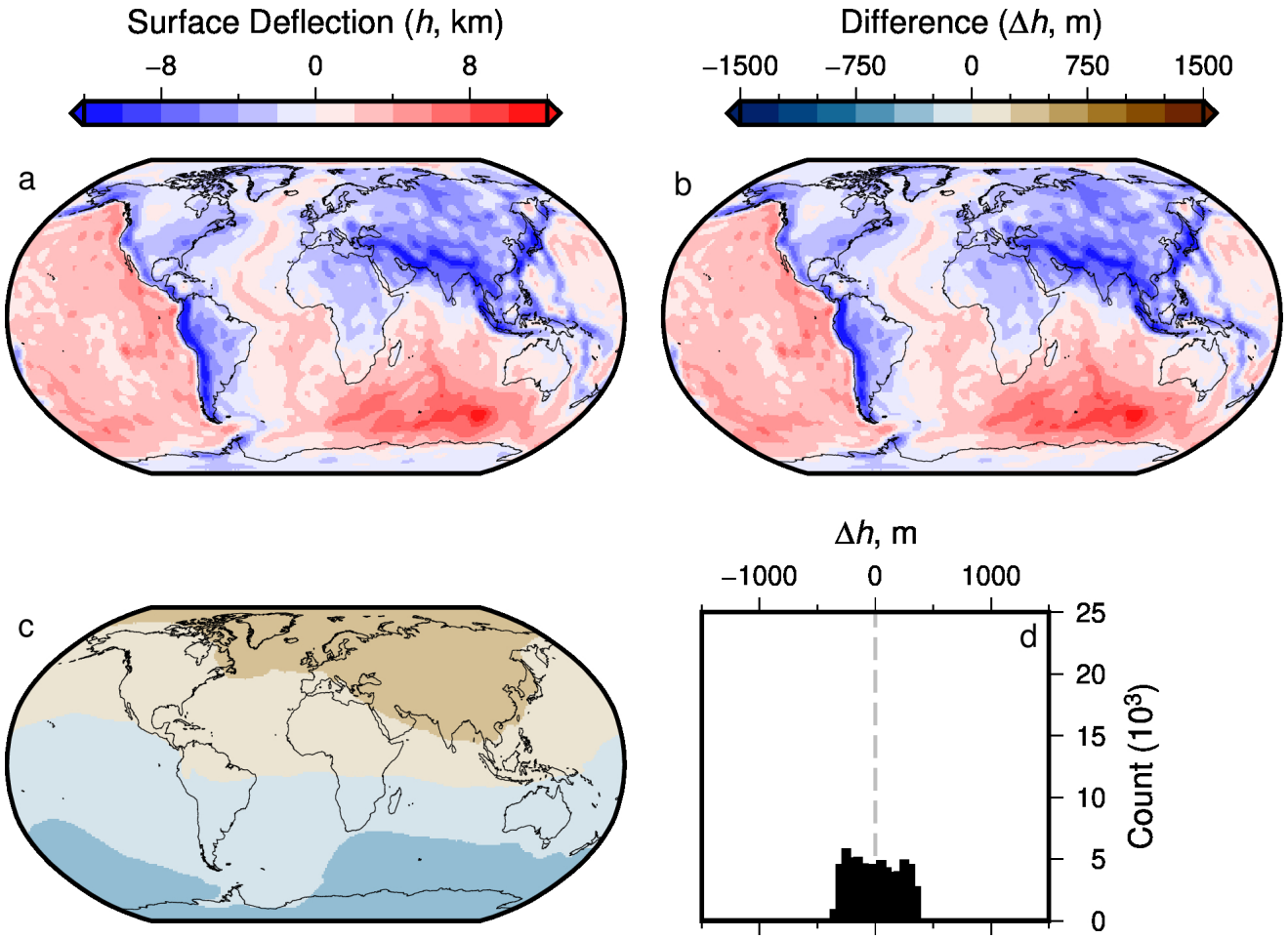

Figure S5. Model 4: Comparing predicted surface deflections with and without stress perturbations induced by gravitational potential of deflected surface. (a) Predicted present-day water-loaded surface deflection calculated using propagator matrix method, with $g = 10$ m s^{-2} everywhere, including terms describing stress perturbation due to change in gravitational potential (i.e., u_3 term in Equation 5 in the main manuscript). (b) As (a) but calculated excluding u_3 term, i.e., same as Figure S3a. See Figure S6 for associated sensitivity kernels. (c) Difference between Models 4 and 2 (panels a and b). Note same colour scales are used as in Figure S4. (d) Histogram of values in (d), weighted by latitude to correct to equal-area.

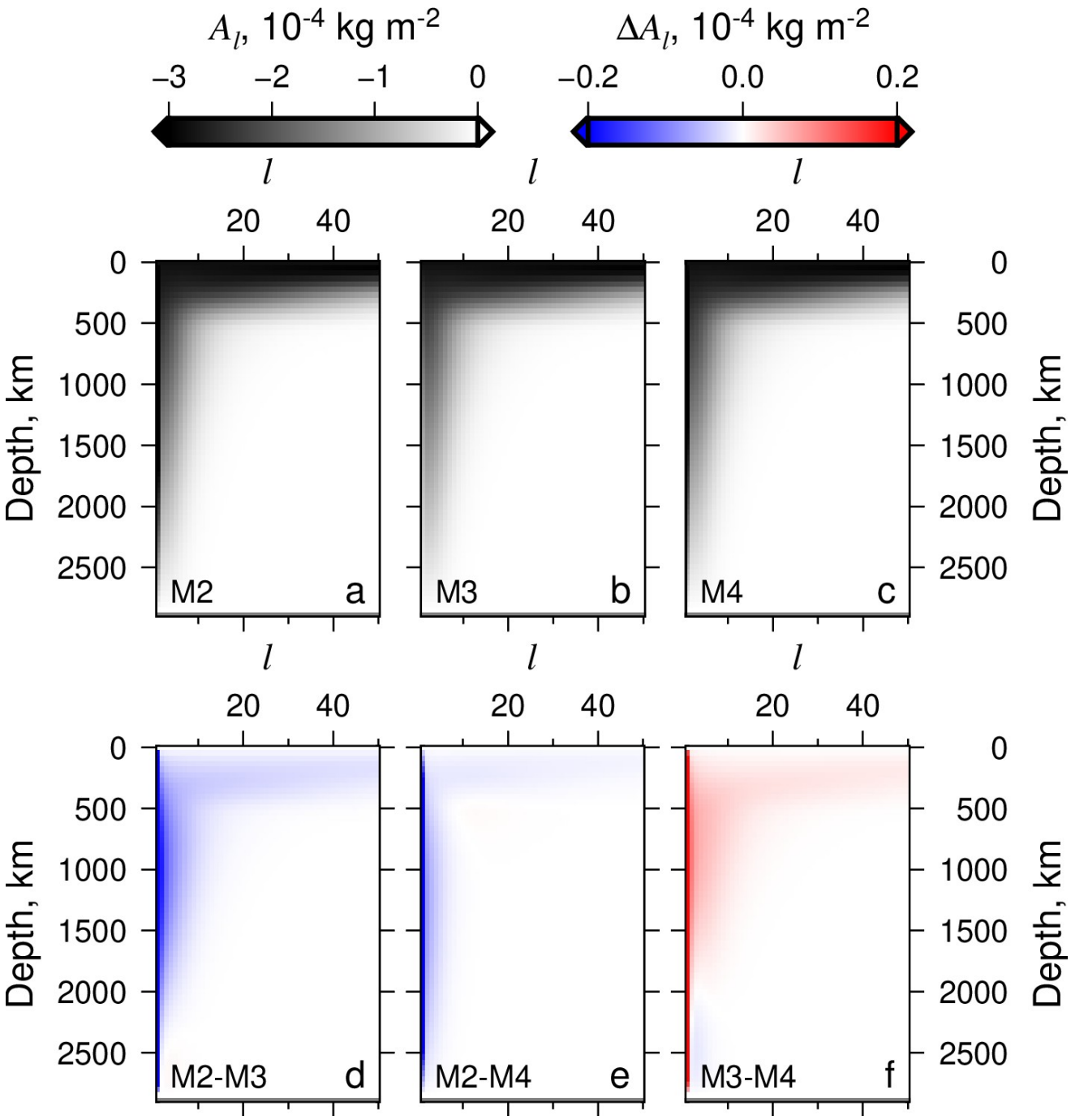

Figure S6. Comparison of sensitivity kernels generated with different treatment of gravitation. (a–c) Sensitivity kernels of Models 2 (M2; $g = 10$ m s^{-2}), 3 (M3; $g = g(r)$) and 4 (M4; gravitational potential of perturbed surface is included and $g = 10$ m s^{-2}); see Figures 3–4 & S3–S5. (d) Comparison of sensitivity kernels from Models 2 and 3; Model 3 kernel is subtracted from Model 2 kernel. (e–f) Comparisons of kernels from Models 2 & 4, and 3 & 4.

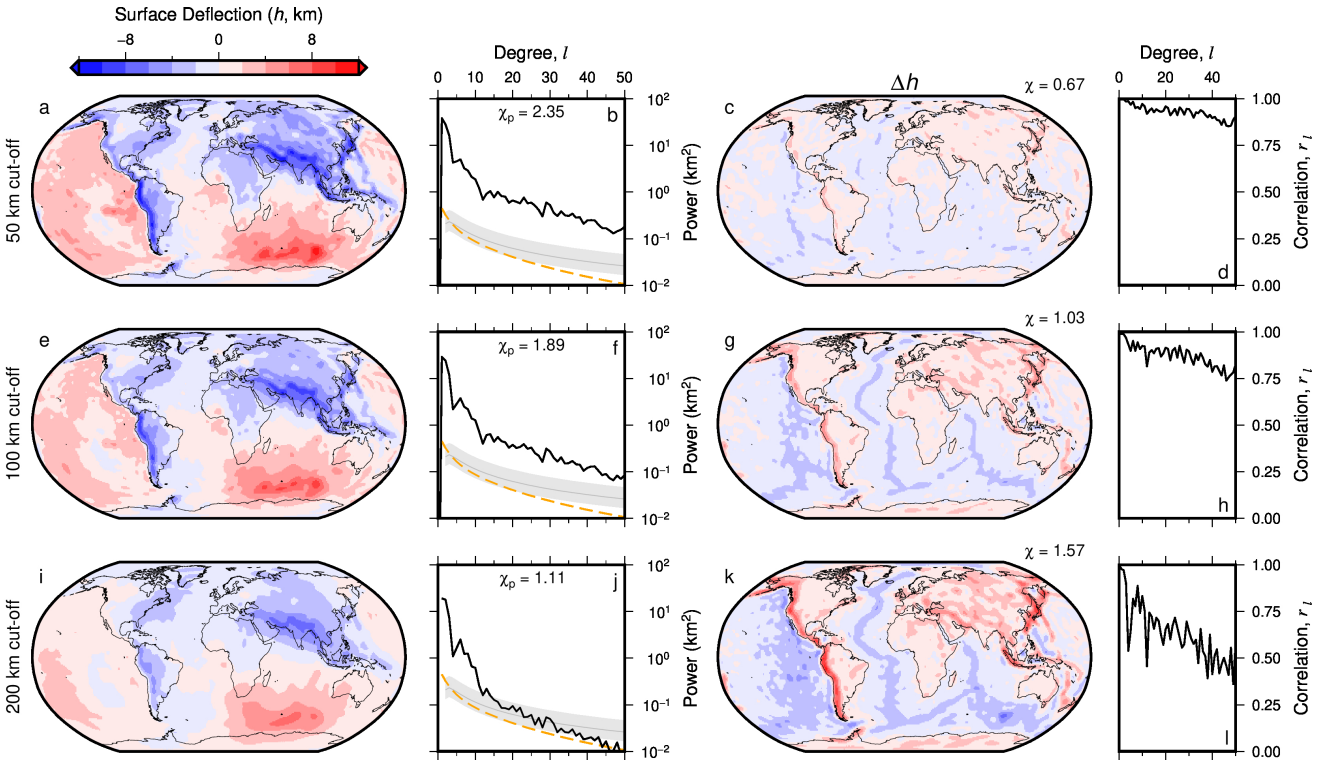

Figure S7. Models 5–7: Effect of removing shallow structure from analytic surface deflection calculations. (a) Model 5: Predicted water-loaded surface deflection from propagator matrix solution for Model 2, i.e., as Figure S3b, but with effect of upper 50 km of density anomaly structure ignored in calculation. (b) Black line = power spectrum of surface deflection shown in (a); gray line and band = expected dynamic topography from Kaula's rule using admittance $Z = 12 \pm 3$ mGal km^{-1} (Kaula, 1963). Orange dashed line = expected power spectrum for water-loaded residual topography from Holdt et al. (2022), via analytical solution of special case of Equation 4 in the main manuscript. χ_p = total root-mean-squared difference between distribution of modeled and theoretical surface deflection power (see Equation 9 in the main manuscript). (c) Difference between Models 5 and 2, i.e., between panel (a) and original propagator matrix solution, Model 2, shown in Figure S3b. (d) Spectral correlation coefficient, r_l, between Model 5 and 2; Equation 8 in the main manuscript. (e–h) and (i–l) as (a–d) but for depth cut-offs of 100 (Model 6) and 200 km (Model 7), respectively.

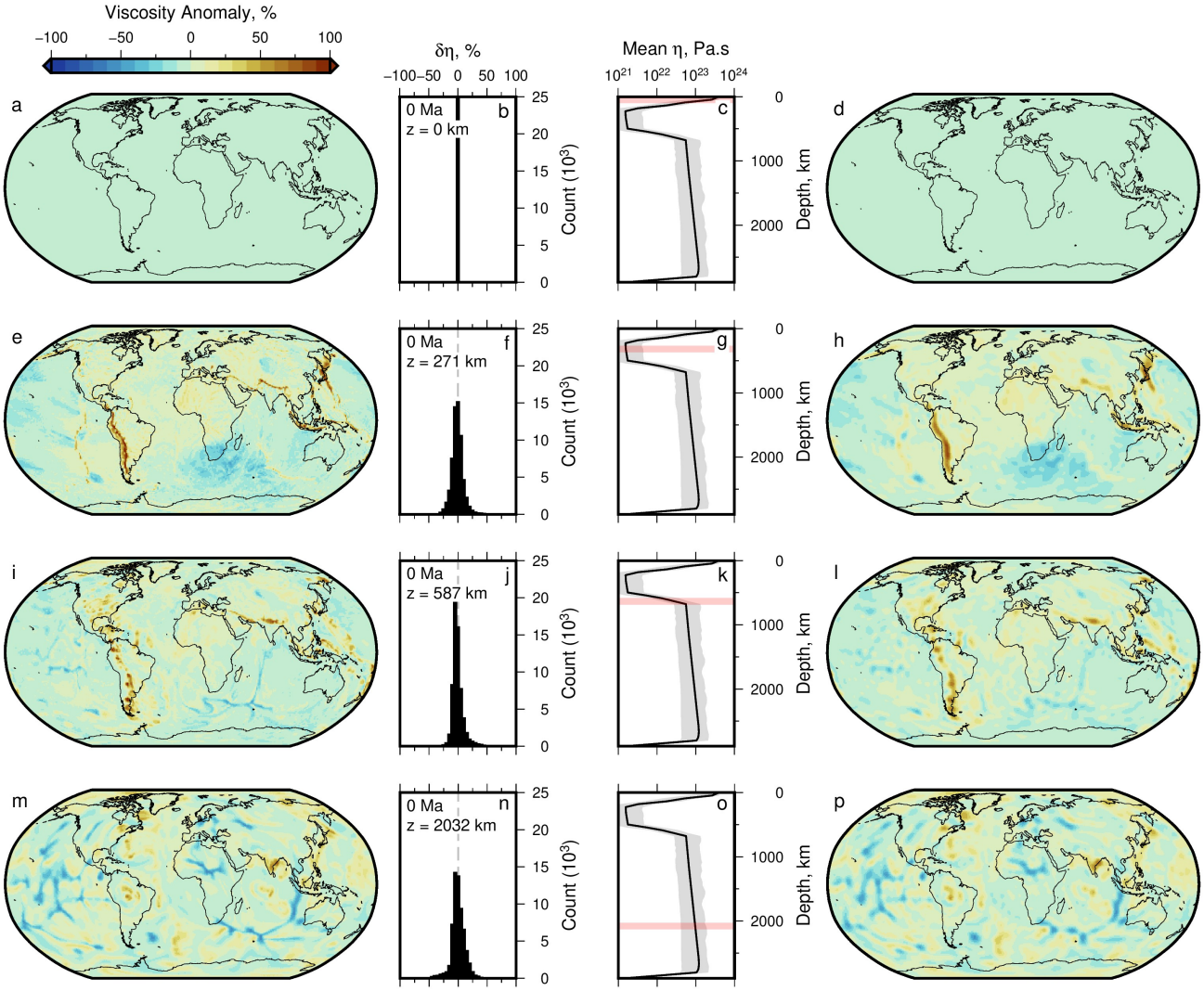

Figure S8. Model 11: Numerical simulation of mantle convection with temperature dependent viscosity, η, and spherical harmonic representation. (a) Present-day viscosity at surface from Model 11a, expressed as percentage deviation from layer mean, $\delta\eta$, plotted at grid resolution of 1 degree. (b) Histogram of values shown in (a), weighted by latitude to correct to equal-area. (c) Black line and gray band = global mean and extreme viscosity values as a function of depth; pink band = depth slice shown in (a). (d) Model 11b: Spherical harmonic fit up to degree $l = 50$ of grid shown in (a), using inverse approach of Hoggard et al. (2016). (e–h) As (a–d) but for depth slice at 271 km below surface. (i–l) and (m–p) 587 km and 2032 km depth slices.

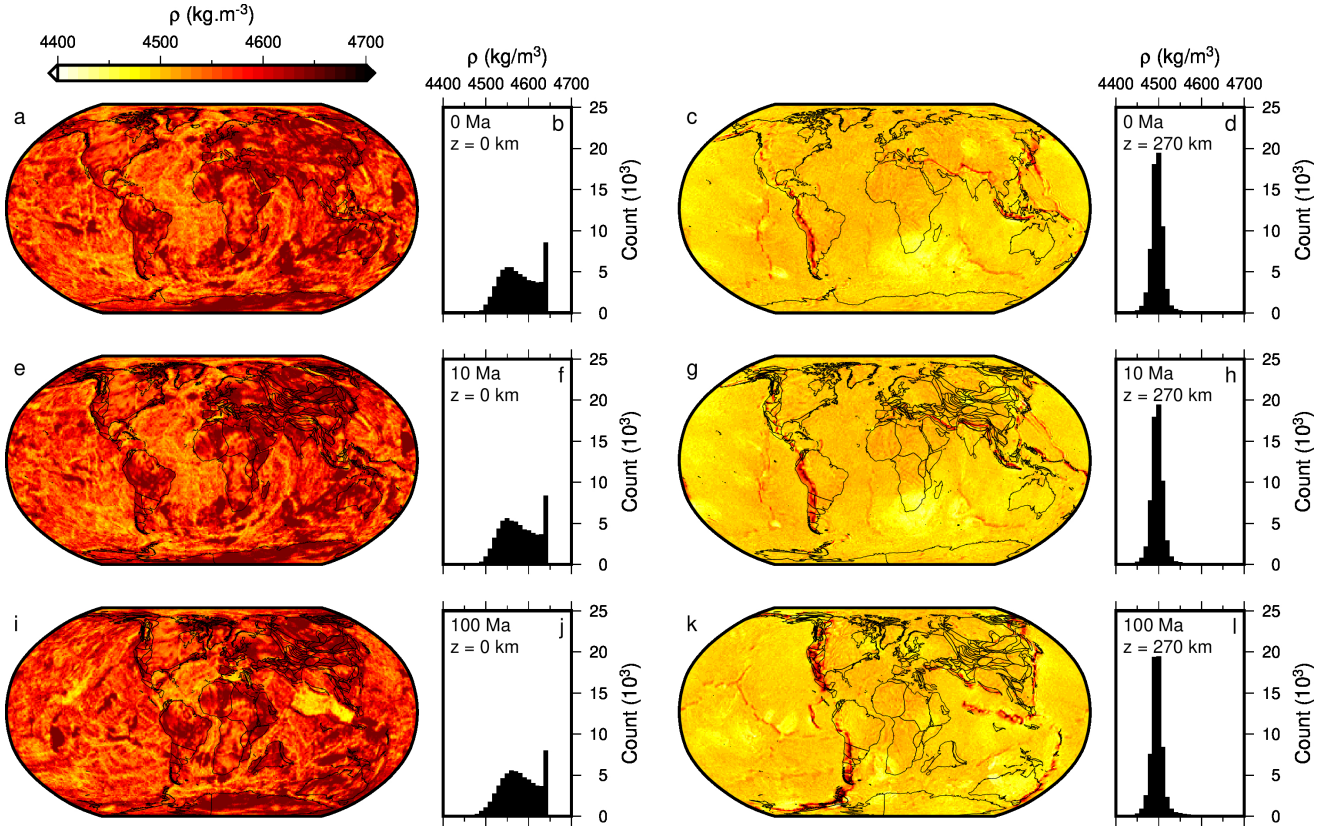

Figure S9. Model 11: Densities predicted by numerical simulation with temperature-dependent viscosity. (a) Predicted present-day density ρ, at surface (z=0), from TERRA model. (b) Histogram of values shown in (a), weighted by latitude. (c–d) As panels (a–b) but for densities at 270 km depth. (e–h) and (i–l) As panels (a–d) for time slices at 10 and 100 Ma (see caption of Figure S1 for expanded description; Figure S8 for viscosity structure; Equation 7 of this document).

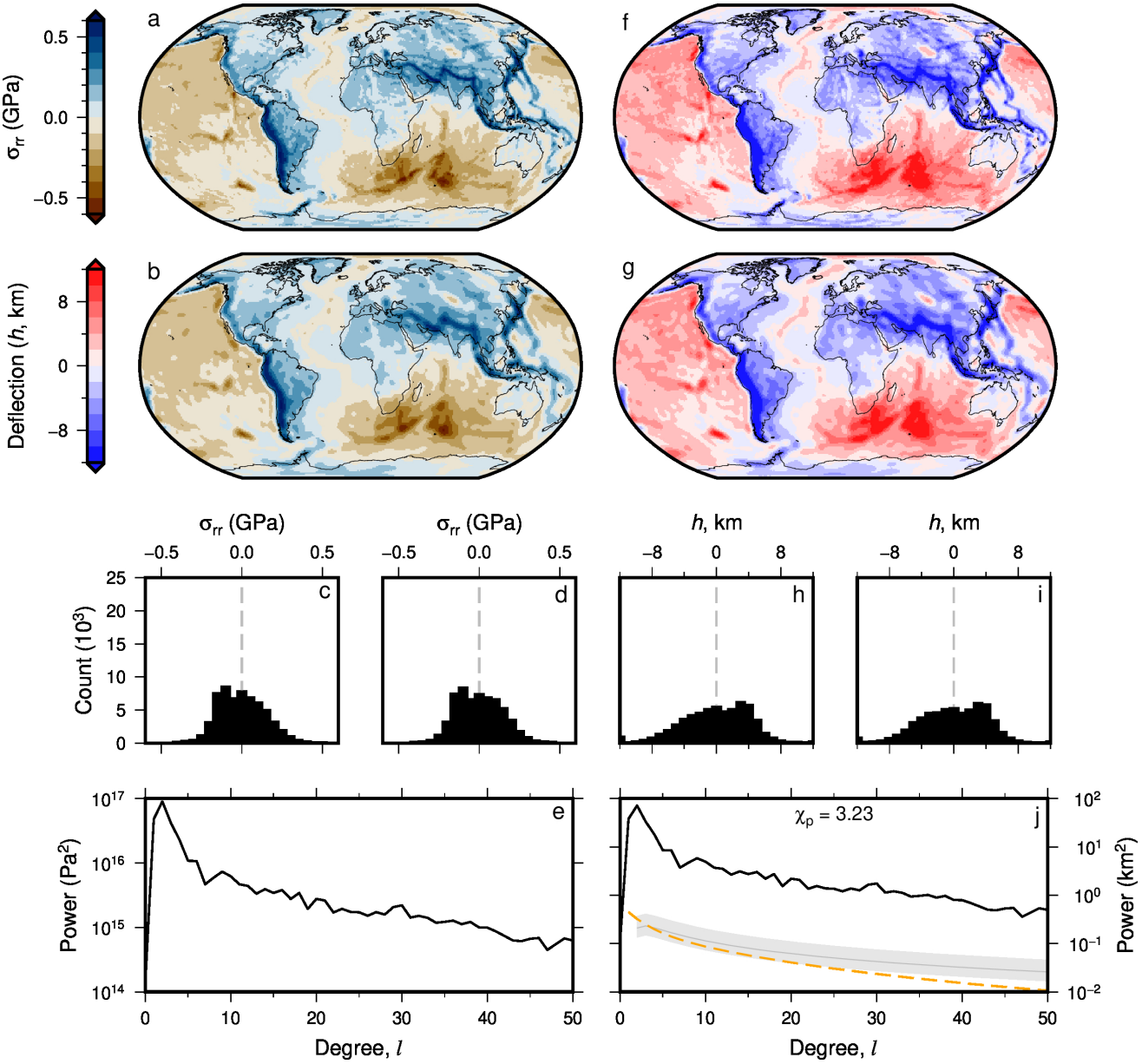
a
b
c
d
e
f
g
h
i
j
σrr (GPa)
Deflection (h, km)
Count (10³)
Power (Pa²)
Power (km²)
Degree, l
h, km
χp = 3.23

Figure S10. Model 11: Predictions of surface stresses and deflections from simulations with temperature dependent viscosity. (a) Predicted present-day surface radial stress, σ_{rr} from numerical TERRA model (Model 11a), plotted at grid resolution of 1 degree. (b) Model 11b: Spherical harmonic representation of Model 11a up to degree $l = 50$. (c) Histogram of values shown in (a), weighted by latitude to correct to equal-area. (d) Histogram of values shown in panel (b). (e) Power spectrum of surface stresses. (f–i) Calculated water-loaded surface deflections and associated histograms for full resolution numerical solutions (f, h) and spherical harmonic representation (g, i). (j) Power spectrum (black) of water-loaded surface deflection (panel g), Kaula's rule (grey curve and band), and water-loaded residual topography (orange); see Figure S2 for expanded description.

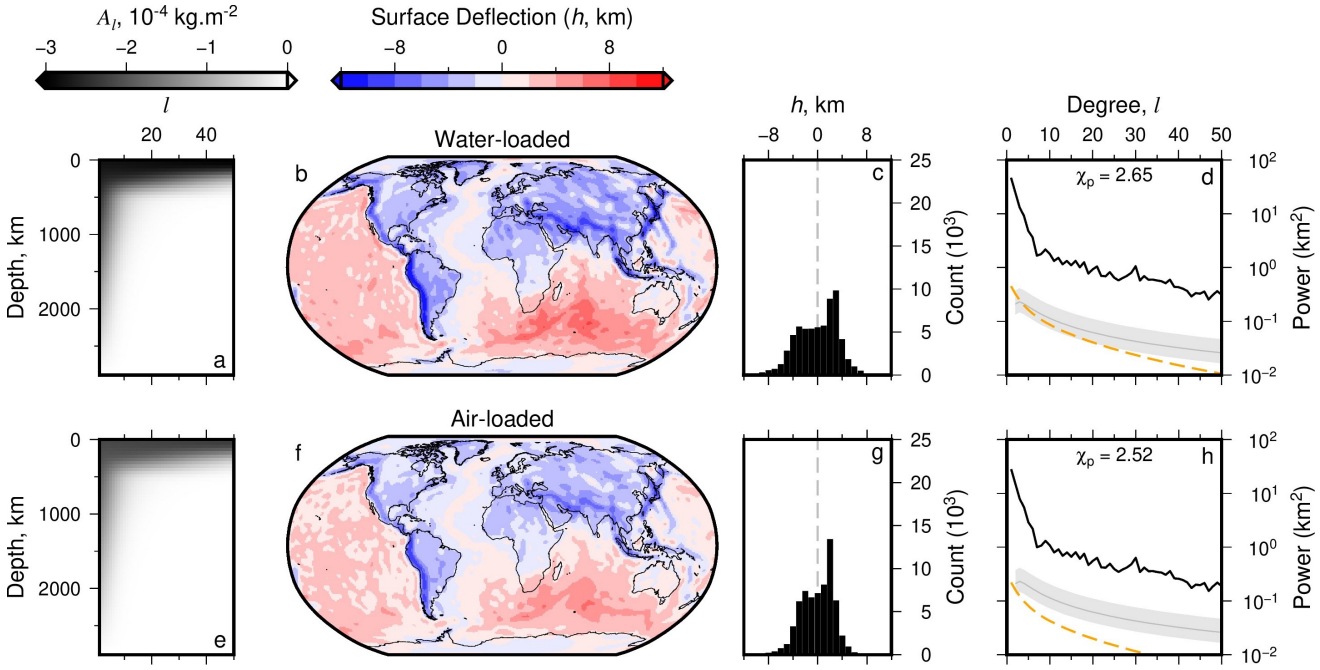

Figure S11. Model 12: Analytical (propagator matrix) predictions of surface deflections from simulations with temperature dependent viscosity. Radial viscosity is calculated using mean (radial) values from numerical model with temperature-dependent viscosity (i.e., Model 11a; Figure S10). (a–d) Present-day, water-loaded, surface deflection calculated analytically using propagator matrix solution; see Figure S3 for expanded description of panels. (e–h) Air-loaded deflection and associated metrics.

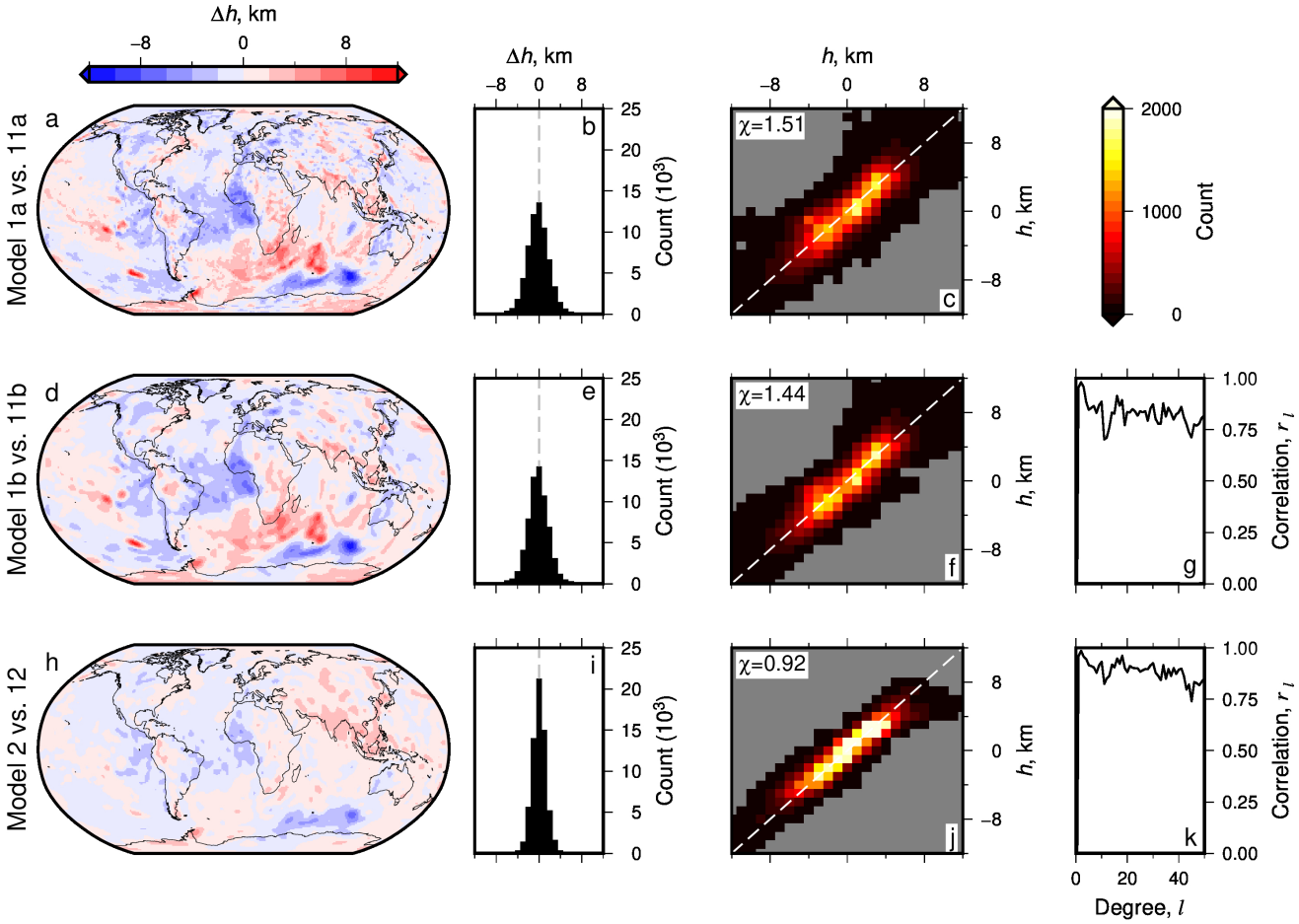
Δh, km
−8
0
8
Model 1a vs. 11a
a
b
c
χ=1.51
Count (10³)
h, km
Count
2000
1000
0
Model 1b vs. 11b
d
e
f
g
χ=1.44
Correlation, r_l
1.00
0.75
0.50
0.25
0.00
Model 2 vs. 12
h
i
j
k
χ=0.92
0
20
40
Degree, l

Figure S12. Comparing surface deflections calculated using normal stresses from numeric simulations (Models 1 and 11) and analytic estimates (Models 2 and 12) with and without temperature dependent viscosity. (a) Difference in predicted surface deflection, Δh, between numerical simulations with (Model 11a) and without (Model 1a) temperature-dependent viscosity. Full-resolution surface radial stresses are converted into surface deflections, h, using Equation 2 of the main manuscript. (b) Histogram of values shown in (a). (c) Pixel-wise comparison of predicted surface deflection between the two models; χ = root-mean-squared difference between predictions, see Equation 7 of the main manuscript; gray dashed line = 1:1 ratio. (d–f) as (a–c) but for surface deflection calculated using spherical harmonic expansion of surface radial stresses (Model 1b vs. 11b). (g) Spectral correlation coefficient, r_l, between model predictions (with and without temperature dependent viscosity; see Equation 8 of the main manuscript). (h–k) as (d–g) but for surface deflections calculated for each model using the propagator matrix approach (Model 2 vs. 12).

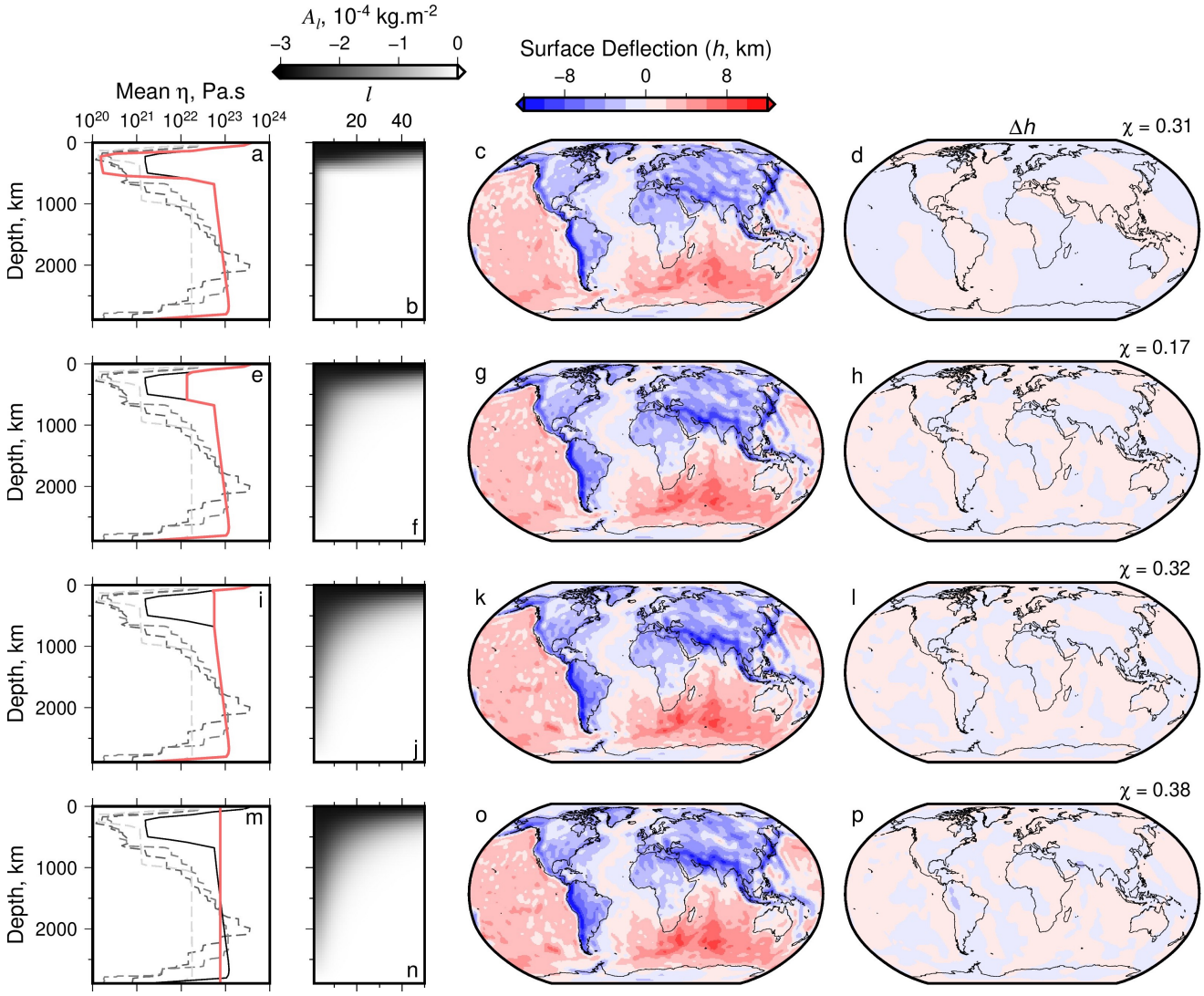
A_l, 10^{-4} kg.m^{-2}
−3 −2 −1 0
l
20 40
Surface Deflection (h, km)
−8 0 8
Mean η, Pa.s
10^{20} 10^{21} 10^{22} 10^{23} 10^{24}
Depth, km
0
1000
2000
a
b
c
d
Δh
χ = 0.31
e
f
g
h
χ = 0.17
i
j
k
l
χ = 0.32
m
n
o
p
χ = 0.38

Figure S13. Models 13–16: Sensitivity of calculated analytic surface deflection to adjusted radial viscosity. (a) Model 13: Black curve = prediction of present-day radial mean viscosity from Model 11; red line = adjusted radial profile with viscosity decreased by a factor of 10 between depths of $\sim$ 300–500 km; gray dashed lines = viscosity profiles used in other studies (see Figure 2c). (b) Sensitivity kernel generated using adjusted viscosity shown in (a). (c) Surface deflection calculated using propagator matrix approach parameterised using adjusted viscosity profile (red curve in panel a), and resulting sensitivity kernel shown in panel (b). (d) Difference between propagator matrix solutions generated using adjusted and un-adjusted viscosity profiles, i.e., panel (c) minus Figure 7b (Model 13 vs. 12). Value of root-mean-squared difference, χ, (between calculated surface deflections for un-adjusted and adjusted viscosity) is stated (see Equation 7 of the main manuscript). (e–h) Model 14: As (a–d) but applying an increase in viscosity of a factor of 10 between $\sim$ 300–500 km. (i–l) Model 15: As (a–d) but applying an increase in viscosity of a factor of 100 between $\sim$ 300–500 km. (m–p) Model 16: As (a–d) but applying an constant viscosity of $\approx 7.5 \times 10^{22}$ Pa s (i.e., the mean value of the reference profile) across all depths.

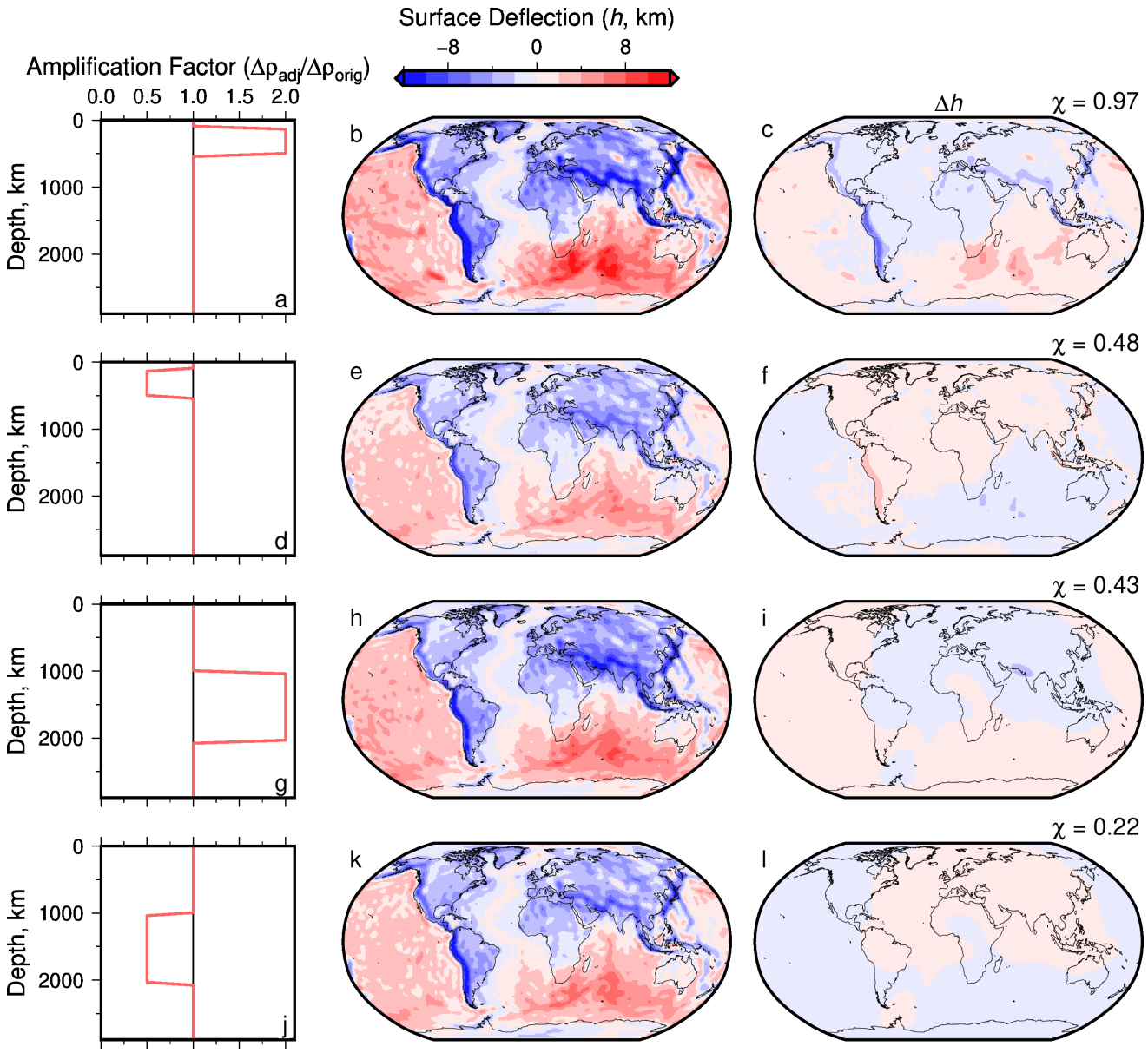

Figure S14. Models 17–20: Sensitivity of calculated analytic surface deflection to adjusted density anomalies. Annotation is as for Figure S13 but for adjusted density anomalies (red lines in left panels), by directly scaling spherical harmonic coefficients ($l > 0$) up or down by a factor of 2 (Models 17 & 19, panels a–c & g–i, respectively) or $\frac{1}{2}$ (Models 18 & 20: d–f & j–l). Viscosity structure applied in each case is same as that used to generate Figure 7b. Sensitivity kernels for surface deflection are not shown since they are invariant with respect to density anomalies, $\Delta\rho$, depending only on viscosity structure.

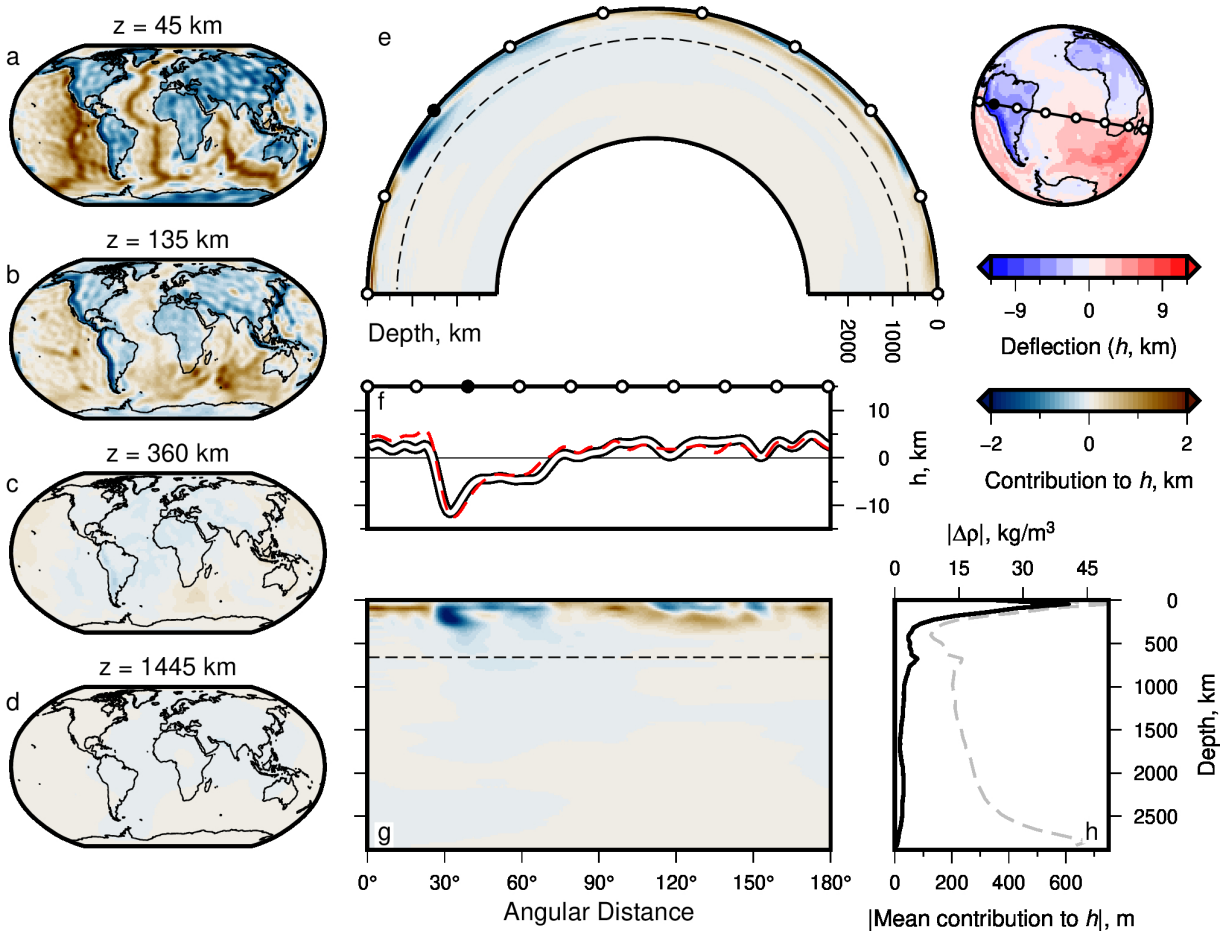

Figure S15. Surface deflections and effective densities up to maximum degree 40. (a–d) Net contribution to present-day water-loaded surface deflection calculated using analytical approach with maximum $l = 40$. Depth slices at 45, 135, 360 and 1445 km depth. (e) Great-circle slice (180°) showing contributions to surface deflection; globe to right shows transect location and calculated surface deflection, up to maximum $l = 40$. White circles = 20° intervals; filled black circle is for orientation; dashed line = 660 km depth contour. (f) White-black curve = surface deflection along transect shown atop globe in panel (e); red dashed curve = surface deflection from Model 2. (g) Cartesian version of panel (e). (h) Grey dashed curve = mean absolute value of density anomalies in Model 12—see top axis for values. Black curve = global mean amplitude (modulus) of contribution from density structure up to maximum $l = 40$ to total surface deflection h.

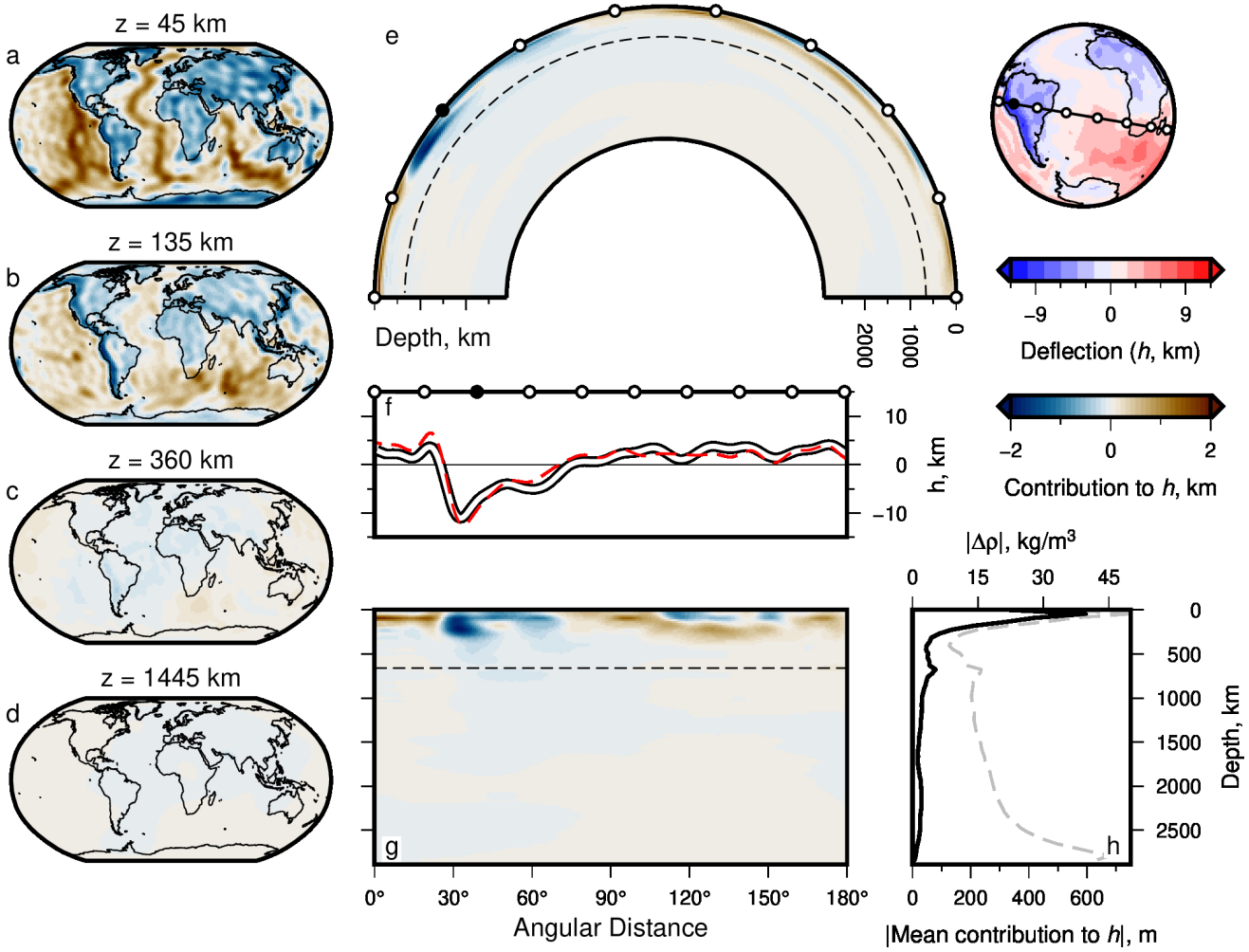

Figure S16. Surface deflections and effective densities up to maximum degree 30.

As Figure S15, but for maximum spherical harmonic degree $l = 30$.

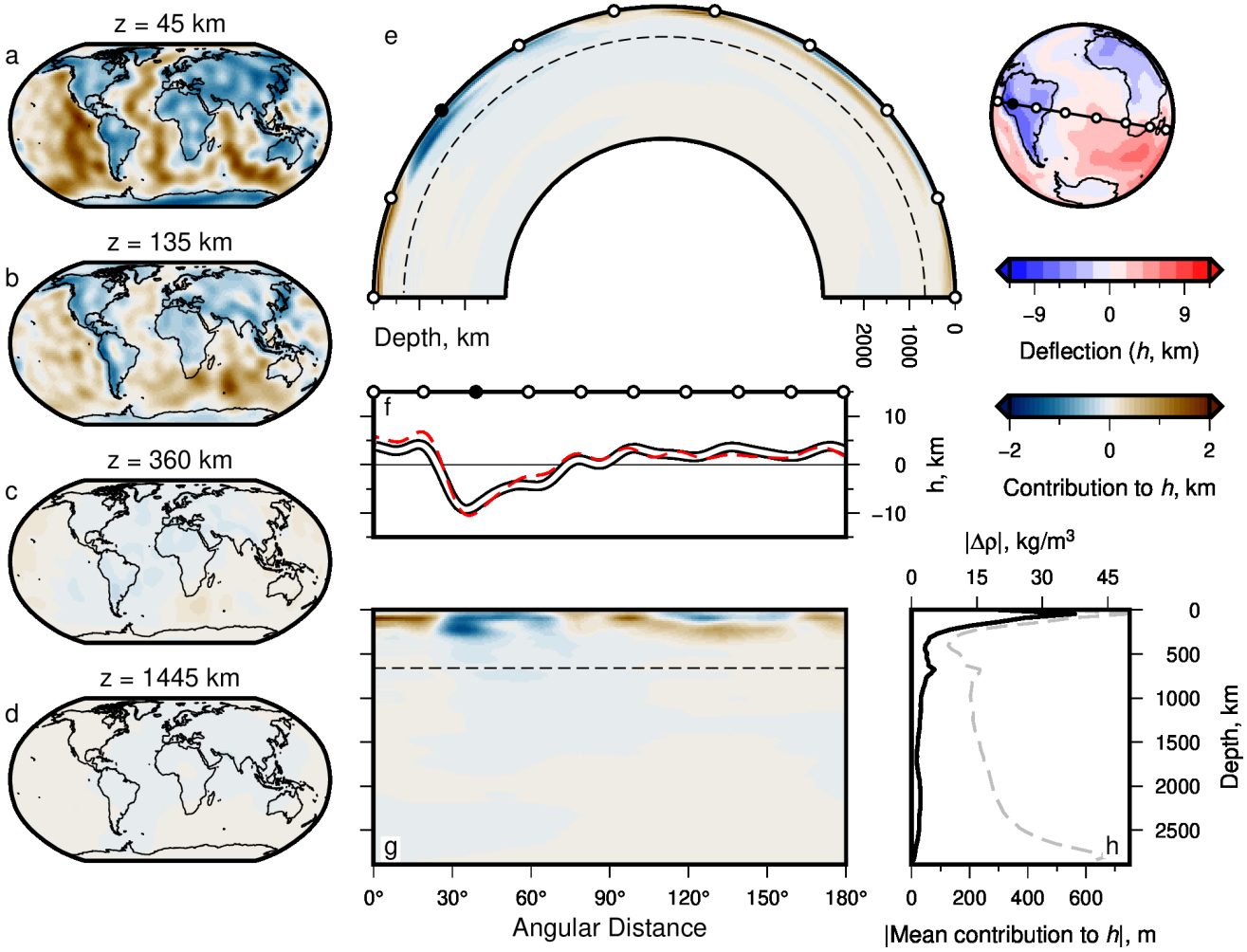

Figure S17. Surface deflections and effective densities up to maximum degree 20.

As Figure S15, but for maximum spherical harmonic degree $l = 20$.

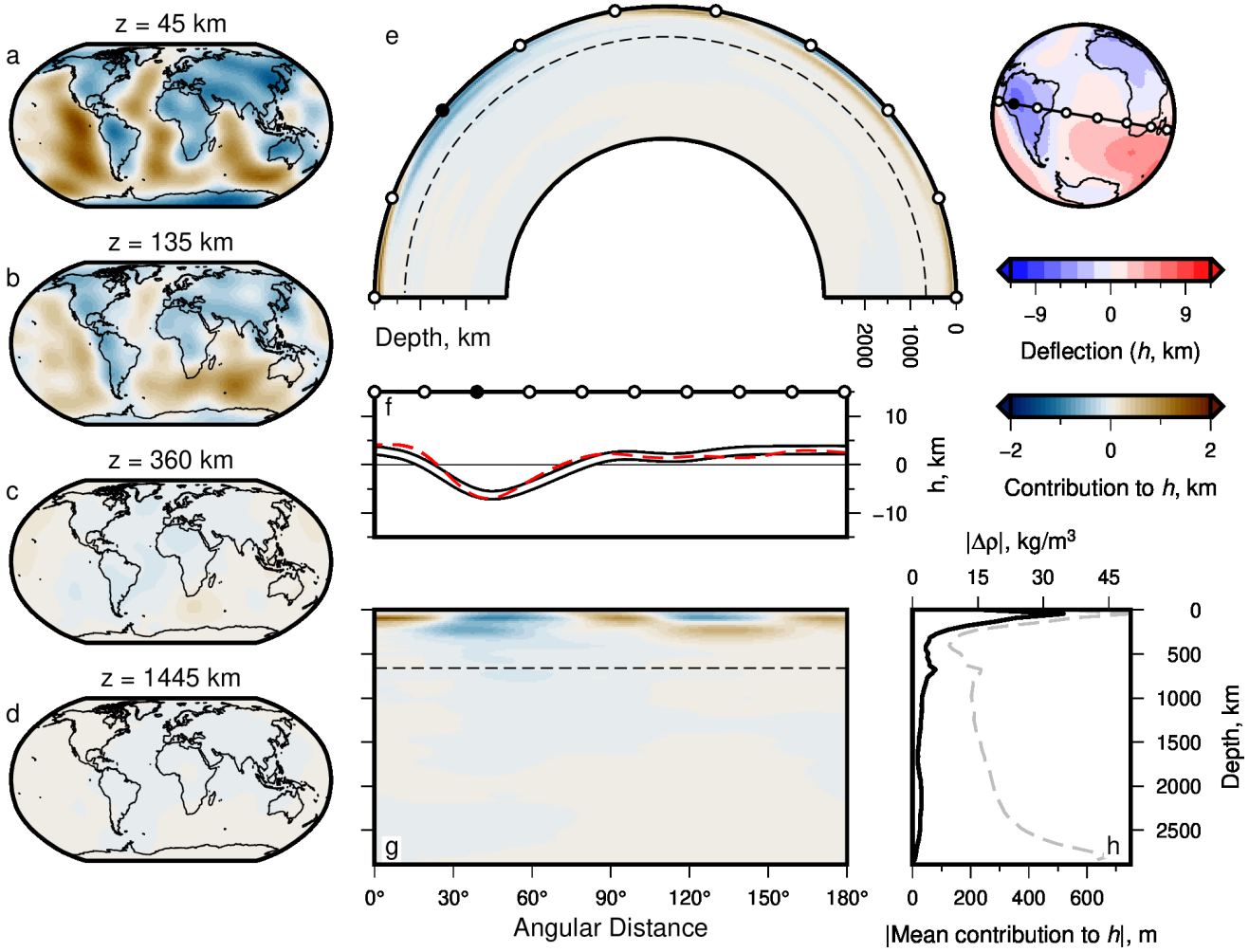

Figure S18. Surface deflections and effective densities up to maximum degree 10.

As Figure S15, but for maximum spherical harmonic degree $l = 10$.

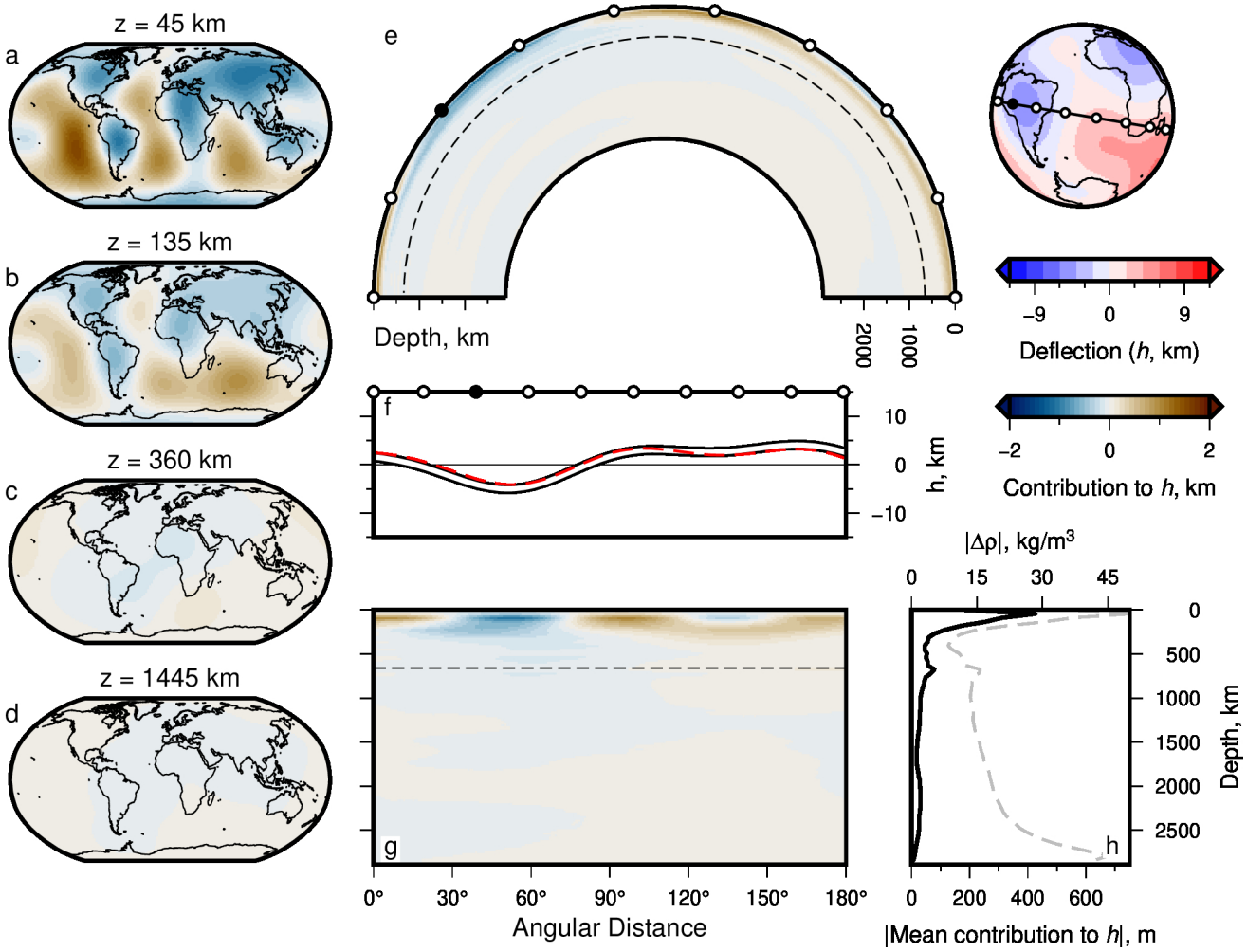

Figure S19. Surface deflections and effective densities up to maximum degree 5.

As Figure S15, but for maximum spherical harmonic degree $l = 5$.